TWO-DIMENSIONAL TELLURIUM: MATERIAL CHARACTERIZATIONS,

ELECTRONIC APPLICATIONS AND QUANTUM TRANSPORT

A Dissertation

Submitted to the Faculty

of

Purdue University

by

Gang Qiu

In Partial Fulfillment of the

Requirements for the Degree

of

Doctor of Philosophy

December 2019

Purdue University

West Lafayette, Indiana

THE PURDUE UNIVERSITY GRADUATE SCHOOL
STATEMENT OF DISSERTATION APPROVAL

Dr. Peide D. Ye, Chair

    School of Electrical and Computer Engineering

Dr. Muhammad A. Alam

    School of Electrical and Computer Engineering

Dr. Saeed Mohammadi

    School of Electrical and Computer Engineering

Dr. Wenzhuo Wu

    School of Industrial Engineering

Approved by:

    Dr. Dimitrios Peroulis

        Head of the School Graduate Program

Dedicated to my beloved better half

Jingyi Fang

ACKNOWLEDGMENTS

Pursuing this Ph. D. degree has been a bittersweet journey and made me a stronger and better person. I would not make this far without the support and guidance from so many people who stand by my side all the time.

First and the most, I would like to give my richest gratitude to my advisor, Prof. Peide D. Ye. for being supportive and inspiring during all these years. Your devotion to work, enthusiasm to knowledge, and attention to details set a perfect role model for me as how to be a good researcher. I remember when I first came to Purdue I did not have a clear vision for my career, and it is your passion to research that has had a life-changing impact on me and motivated me to achieve higher goals in the future.

I am also very grateful for my Ph. D. committee members, Prof. Muhammad A. Alam, Prof. Saeed Mohammadi, and Prof. Wenzhuo Wu for experimental support and valuable instructions. My particular appreciation goes to Prof. Wenzhuo Wu, for introducing this great topic to me on and we had a very fruitful collaboration. I also want to acknowledge Prof. Xianfan Xu, Prof. Gary Cheng, Prof. Qiong Nian (Arizona State University), Prof. Kyeongjae Cho (University of Texas at Dallas), Prof. James Hwang (Lehigh Univeristy) and Dr. Samuel Berweger (National Institute of Standards and Technology) for offering the opportunity for collaboration.

I greatly appreciate the support from my group members, Dr. M. Si, Dr. H. Bae, Dr. H. Wu, Dr. J Zhang, Dr. Y. Deng, Dr Y. Du, Dr. H. Zhou, Dr. L. Yang, Dr. S. Alghamdi, N. Conrad, J. Li, Y. Qu, W. Chung, A. Charnas, J. Noh, X. Lyu, P. Liao, C. Niu, D. Zheng, Z. Zhang and Z. Lin. A big thank you also goes to those of you who shared so many memorable hard-working days and nights with me in the cleanroom. Many thanks also to Y. Wang, R. Wang, S. Gao, M. Wu, Dr. S. Jin K. Xiong (Lehigh Univeristy), and Dr. Y. Nie (Lawrence Berkeley National Laboratory) who have had a close and productive collaboration with me.

I also gratefully thank the very knowledgeable and helpful staff members from National High Magnetic Field Lab (NHMFL), Tim Murphy, Ju-Hyun Park, G. Jones, and Hongwoo Baek, Jan Jaroszynski, Alexey Suslov, William Coniglio, and Prof. Peng Xiong and Tianhan Liu from Florida State University. I have visited Tallahassee 12 times to work on site at NHMFL which makes up a big part of my Ph. D. career, and I developed my experimental skills under the coaching of these wonderful people.

I am deeply indebted to my parents and family back in China who have firmly supported me for every step I have taken in my life. I want to give my eternal appreciation to my parents for their uttermost love and unconditional sacrifice, which gave me the courage to embark the challenging journey of pursuing Ph. D. degree in the first place.

And finally to Jingyi Fang, who has survived this five-year distance relationship together and always been there for me every moment. I will remember those frustrating nights I had in the lab, and it was your comforting and encouraging voice over the phone that motivated me to get out of the bed and start off again the very second day. And now it is your turn to go after the Ph. D. degree and I wish I can instill you the power and courage as much as you gave me. Marrying you is the most blessed thing during my Ph. D. and I cannot wait to start the new journey in the life with you.

TABLE OF CONTENTS

LIST OF FIGURES

SYMBOLS

μ Mobility

t Thickness

R_c Contact Resistance

V_{ds} Source-to-Drain Voltage

V_g Gate Voltage

V_{th} Threshold Voltage

L_{ch} Channek Length

T_c Critical Temperature

k_B Boltzmann Constant

H_c Critical Field

Φ_c Flux Quanta

ξ Copper Pair Coherence Length

g_m Transconductance

R_{xx} Longitudinal Resistance

R_{xy} Transverse Resistance

S Seebeck Coefficient

ϵ_s Semiconductor Permittivity

n_{2D} Two-Dimensional Density

n_{HALL} Hall Density

ω_c Cyclotron Frequency

τ Carrier Lifetime

m^* Effective Mass

h Planck's Constant

$\hbar$ Reduced Planck's Constant

e	Elementary Charge
g_s	Spin Degeneracy
g_v	Valley Degeneracy
ν	Filling Factor
B_F	SdH Oscillation Frequency
S_F	Fermi Surface Area
Γ	Landau Level Broadening
R_D	Dingle Factor
g^*	Effective g-Factor
μ_B	Bohr Magneton
ΔG	Magneto Conductance Fluctuations
L_ϕ^{UCF}	Coherence Length Measured from Universal Conductance Fluctuation
ΔE_{SAS}	Energy Gap between Symmetric and Antisymmetric States
V_{tg}	Top Gate Voltage
V_{bg}	Back Gate Voltage

ABBREVIATIONS

2D	Two-Dimensional
TEM	Transmission Electron Microscopy
FET	Field-Effect Transistor
SdH	Sdhubnikov-de Haas
QHE	Quantum Hall Effect
IC	Integrated Circuit
TSMC	Taiwan Semiconductor Manufacturing Company, Limited
3D	Three-Dimensional
vdW	van der Waals
DOS	Density of States
1D	One-Dimensional
CNT	Carbon Nanotubes
CMOS	Complementary Metal-Oxide-Semiconductor
CVD	Chemical Vapor Deposition
BP	Black Phosphorus
CVT	Chemical Vapor Transport
ALD	Atomic Layer Deposition
TMD	Transition Metal Dichalcogenides
MOS	Metal-Oxide-Semiconductor
SOC	Spin-Orbit Coupling
AFM	Atomic Force Microscopy
XRD	X-Ray Powder Diffraction
PVD	Physical Vapor Deposition
PMOS	P-Type Metal-Oxide-Semiconductor

NMOS	N-Type Metal-Oxide-Semiconductor
MBE	molecular beam epitaxy
LB	Langmuir-Blodgett
CBM	Conduction Band Minima
VBM	Valence Band Maxima
TLM	transmission line method
HAADF	High-Angle Annular Dark-Field Imaging
STEM	Scanning Transmission Electron Microscopy
HRTEM	High Resolution Transmission Electron Microscopy
EDS	Energy-Dispersive X-Ray Spectroscopy
TO	Transverse Optic Phonon
LO	Longitudinal Optic Phonon
AC	Alternating Current
BCS	Bardeen-Cooper-Schrieffer
GL	Ginzburg-Landau
WHH	Werthamer-Helfand-Hohenberg
EBL	Electron Beam Lithography
WL	Weak Localization
WAL	Weak Antilocalization
UCF	Universal Conductance Fluctuation
HLN	Hikami-Larkin-Nagaoka
MOSFET	Metal-Oxide-Semiconductor Field-Effect Transistor
2DEG	Two-Dimensional Electron Gas
DFT	Density Functional Theory
EOT	Effective Oxide Thickness

NOMENCLATURE

Te	Tellurium
Si	Silicon
H-SiC	Hexagonal Silicon Carbide
Ni	Nickel
Cu	Copper
h-BN	Hexagonal Boron Nitride
Al_2O_3	Aluminum Oxide
Se	Selenium
MoS_2	Molybdenum Disulfide
WSe_2	Tungsten Diselenide
$NbSi_2$	Niobium Disilicide
Na_2TeO_3	Sodium Tellurite
N_2H_4	Hydrazine
PVP	Polyvinylpyrrolidone
NaOH	Sodium Hydroxide
DMF	N, N-dimethylformamide
$CHCl_3$	Chloroform
SiO_2	Silicon Dioxide
Pd	Palladium
Au	Gold
$PdTe_2$	Palladium Telluride
$PdCl_2$	Palladium Chloride
Ti	Titanium
HfO_2	Hafnium Dioxide

ZrO_2	Zirconium Dioxide
GaAs	Gallium Arsenide
Cr	Chromium

ABSTRACT

Qiu, Gang Ph.D., Purdue University, December 2019. Two-dimensional Tellurium: Material Characterizations, Electronic Applications and Quantum Transport. Major Professor: Peide D. Ye.

Since the debut of graphene, many 2D materials have emerged as promising candidates for silicon alternatives to extend Moores Law, such as MoS_2 and phosphorene. However, some common shortcomings such as low mobility, instability and lack of massive production methods limit the exploration and applications of these materials. Here, we introduce a novel member to the 2D category high-mobility air-stable 2D tellurium film (tellurene).

Tellurium (Te) is a narrow bandgap semiconductor with unique one-dimensional chiral structure. Recently, a hydrothermal synthesizing method was developed to produce large-area tellurene nanofilms with thickness ranging from tens of nanometers down to few layers. In this thesis, a thorough investigation of Te properties in 2D quantum region was first carried out by various material characterization techniques including TEM and Raman spectroscopy. Potential applications of Te-based electronics, optoelectronic and thermoelectric devices were explored, and high-performance Te FETs were achieved with record-high drive current over 1 A/mm via device scaling and contact engineering. Magneto-transport, including weak anti-localization and Shubnikov-de-Haas oscillations was studied at cryogenic temperature. Quantum Hall effect was observed for the first time in both 2D electron and hole gases with mobility of 6,000 and 3,000 cm^2/Vs, and non-trivial Berry phase in Te 2D electron system was detected as the first experimental evidence of massive Weyl fermions. This work not only demonstrates the great potential of tellurene films for electronics and quantum

device applications, but also expands the spectrum of topological matters into a new material species - Weyl semiconductors.

1. INTRODUCTION

1.1 The Post-silicon Era beyond Moores Law

Since Moore's Law was first put forward in 1965, this prophecy has governed cadence of miniaturizing the transistor geometry and increasing the transistor density on integrated circuits (ICs) for over half a century. Nowadays, the leading semiconductor corporations such as TSMC, Samsung and Intel are devoting themselves to developing 7-nm and 5-nm technology node, and we may expect the advent of 3-nm technology node in the foreseeable future. Beyond that, the long-living Moore's Law may be extended by using 3D vertical integration to keep increasing the density of the transistors. However, there is no doubt that this downsizing trend cannot be sustained forever as the device size is approaching the atomic scale and quantum effect starts to rule the transistor behavior. Yet even before the device feature size enters the quantum realm, we have encountered serious technical problems. For one thing, as we keep shrinking the device size, we start to lose electrostatic control and the transistors cannot be shut off. The large standby power consumption will make our laptops and cellphones burning hot. Moreover, downsizing traditional 3D semiconductors such as silicon comes with the cost of degrading mobility. More specifically, for ultra-thin body silicon devices, the mobility decrease with the thickness of the channel following an empirical sixth power rule [1]: $\mu \propto t^6$. As a rule of thumb, to maintain electrostatic control, the channel thickness should be one third of the gate length. That is to say, for a transistor with 3 nm gate length, the channel need to be as thin as 1 nm, or in other words, a couple of layers of atoms. The surface scattering and the dangling bonds will deteriorate the device performance. A different approach, whether structural-wise or material-wise, is desperately demanded semiconductor industry in the post-silicon era. A semiconductor material that can be operated at least

as fast as silicon, yet more immune to the mobility degradation when approaching 2D limit, will be an ideal candidate. This is where 2D vdW materials comes to the rescue. 2D materials features vdW bonding between atomic layers, which allows easy cleavage into a perfect dangling-bond-free interface and sustain a reasonably high mobility even in mono-layer regime. Besides, 2D material is a big family covers a wide spectrum from metals, semiconductors to insulators, which allows us to potentially build all-2D-material circuits by stacking different 2D materials together like Lego. Here in the next section, we will introduce synthesis, material properties, and recent research progress of some of the most well-known 2D materials.

1.2   An Overlook of 2D Materials and Recent Progress

1.2.1   Graphene

The Nobel-prize-winning material graphene was the very first 2D material that was isolated into single layer. The carbon atoms are arranged into hexagonal crystal structure connected with sp^2-hybridzed valence bonds. The fourth p-orbit electron forms an out-of-plane π bond, which gives a unique Dirac cone band structure at the corners of Brillouin zone K and K′ point [2]. Therefore graphene is classified as a semimetal, meaning that although it does not possess a finite band gap in the electronic structure, the density of states (DOS) is zero at Dirac point where the conduction band and valence band touch with each other. The linear dispersion in the vicinity of Dirac point gives rise to massless Dirac fermions with high mobility over 25,000 cm^2/Vs at room temperature.

This special band structure sparked tremendous interest to study the quantum properties of relativistic particles in low energy spectrum. Many fascinating physical properties has been observed in graphene system such as non-trivial topological phase [3,4] and quantum Hall effect even at room temperature [5]. By stacking monolayers of graphene with different angles, an additional sub-band forms due to the long

range moire superlattice which introduces more exotic phenomena such as Hofstadter butterfly [6], superconductivity [7] and Mott insulator [8].

Despite all the fantastic progress in condensed matter physics research, the development of graphene based electronics falls far behind. The major obstacle is that graphene FETs cannot be turned off and the on/off ratio is within one order due to its semimetallic nature, which is unsuitable for low-power circuits. For transistors, a moderate band gap over 0.3 eV is generally needed as a guideline in order to shut off the device. Therefore recently efforts have been pivoted into studying another carbon-based 1D counterpart - CNTs for FETs and CMOS circuits.

The easiest way to obtain graphene exfoliation, either mechanically or chemically, from bulk graphite. This method yields the highest quality of graphene crystal, however these nano-sheets are in several μm of lateral size and thus cannot be used for massive production. Alternative chemical methods have been developed to grow wafer-size few layer or even monolayer graphene using epitaxial growth on H-SiC crystal [9] or chemical vapor deposition (CVD) on metal sheets like Ni and Cu [10,11].

1.2.2 Black Phosphorus

Black phosphorus (BP) is the most stable allotrope of phosphorus and was first synthesized in 1914 in with high pressure and high temperature technique [12]. Later other routes were proposed to prepare bulk BP such as using mercury as catalyst and recrystallization from bismuth flux [13–15]. In 2008, Nilges et al. [16] proposed a fast low-pressure chemical vapor transport (CVT) method using AuSn as transport agent to produce bulk BP single crystals, which later was further simplified by Kopf et al. [17]. Efforts has also been made to grow large area BP thin films [18,19].

Just like graphene, black phosphorus also has a layered crystal structure with a puckered honeycomb lattice. Phosphorene, the monolayer form of BP was first isolated in 2014 [20,21]. BP FETs were subsequently demonstrated with extraordinary electrical performance with on/off ratio over 10^6 and field-effect mobility ranging

from a couple of hundreds to near 1000 cm^2/Vs. The band gap of BP evolves from 0.3 eV (bulk) to over 2 eV in monolayer form with enhanced quantum confinement. BP shows p-type semiconductor behavior due to the intrinsic p-type defects. Furthermore, by proper device engineering, such as adopting low work-function metal contact [22], ALD doping [23], and gate electrostatic doping [24], n-type transistors with high electron mobility are also realized. Thereby, it has great potential to be used as ultrathin transistor channel material and further pushes CMOS scaling trend. In addition to extraordinary electrical properties, the ultrathin 2D BP also has superior mechanical flexibility and durability [25], thus showing promise as a possible flexible electronics component.

The major roadblock towards applications of BP is its instability in air. Few-layer BP films will absorb oxygen and water in the air and degrade within several hours and this issue becomes more severe with reduced thickness. To preserve BP films, a capping layer such as h-BN [26] or ALD deposited Al_2O_3 [27] has been proved to slow down the oxidation process to some extent. However these methods lacks of massive manufacturing capability and the instability issue poses a critical challenge towards the application of BP. An alternative material with air-stability is desperately needed.

1.2.3   MoS$_2$ and other TMDs

Transition metal dichalcogenides are a group of material that share a same element composition MX$_2$ where M stands of transition metal and X are group VI chalcogen atoms (ie. S, Se and Te). There are over 40 different TMDs which covers a vast spectrum of material category from superconductors to insulators. Several TMDs such as MoS$_2$ and WSe$_2$ have received extensive attention since they have a favorable band gap around 1 eV and are very stable in air. MoS$_2$ is one of the earliest and the most intensively investigated TMD materials in terms of FETs. The demonstration of MoS$_2$ transistors can be traced back to 2007 [28], and later the transistor performance kept improving and even monolayer MoS$_2$ also exhibits extraordinary electri-

cal performance [29]. MoS_2 also shows great scaling potential [30, 31] even down to sub-nanometer gate length [32] that is compatible with state-of-the-art semiconductor manufacturing technology node. Large-area atomically thin MoS_2 films [33] and TMD hetero-structures [34] have also been achieved with CVD method.

However there are some issues that hinders the advance of TMD-based electronics. The major roadblock is the intrinsically low carrier mobility due the large effective mass of electrons in TMDs. The mobility in TMDs is in general two orders lower than silicon, and the mobility describes how fast electrons/holes move in the semiconductor which has huge impact on the device operation speed and the clock frequency of the microprocessor. Besides, due to the relatively large bandgap and the difficulty in band alignment, contact resistance is quite high in TMD Schottky transistors. Finally, high-performance p-type TMD transistors have not yet been demonstrated to match the n-type MoS_2 transistors in order to construct CMOS logic circuits.

1.3   Fundamentals of Tellurium and Tellurene

Despite the variety of 2D materials that have been discovered and intensively studied, we have not yet met the perfect material that is capable of replacing silicon and Si-based semiconductor technology. From the discussion above, we can come to the conclusion that a suitable candidate should: (1) have a reasonable bandgap (at least 0.3 eV) for the device to be properly shut off and reduce standby power; (2) be air-stable for real device application (instead prototype testing devices in the lab); (3) develop sophisticated doping technique for easy access of both electrons and holes in order to build complimentary MOS circuit; (4) high and near-symmetric carrier mobility for both electrons and holes for building high-speed CMOS devices.

In this section we will introduce some basic physical and chemical properties of tellurium and its 2D counterpart tellurene and show that this material indeed fulfills all the requirements we proposed above and has great potential for applications in electronics, optoelectronics and quantum devices.
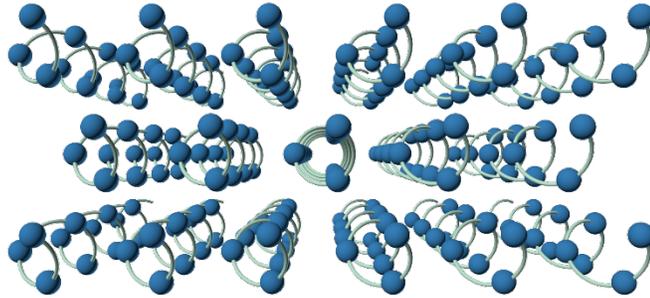
Fig. 1.1. Crystal structure of Te. Helical chains with three-fold rotational symmetry are bonded together by vdW-like forces and arranged into hexagonal 1D structure.

Tellurium (Te) is a group VI element with 2 s-orbital electrons and 4 p-orbital electrons. It is also the heaviest stable (non-radioactive) non-metal element known so far in the periodic table. Hexagonal Te is the most stable and most common allotrope in nature, and from hereon we will be focusing on this phase of Te only. Te is a narrow bandgap semiconductor with a unique one-dimensional helical atomic structure. The crystal is formed by parallel assembled helical chains with three-fold screw symmetry that stretches in z direction, with either left or right handedness (see Figure 1.1a). These chains are interconnected by van der Waals forces in the x-y plane into a trigonal crystal, as shown in side view and top view in Figure 1.2a and 1.2b. The rotational symmetry, while relatively common among organic macromolecues [35] (DNA is the most well-known example), is very rare at atomic scale in very few types inorganic crystals such as certain zeolites [36] and $NbSi_2$ [37]. The inherent rotational symmetry in helical crystal structure gives rise to some unique properties of tellurium such as current-induced spin polarization [38] and circular photon drag effect [39].
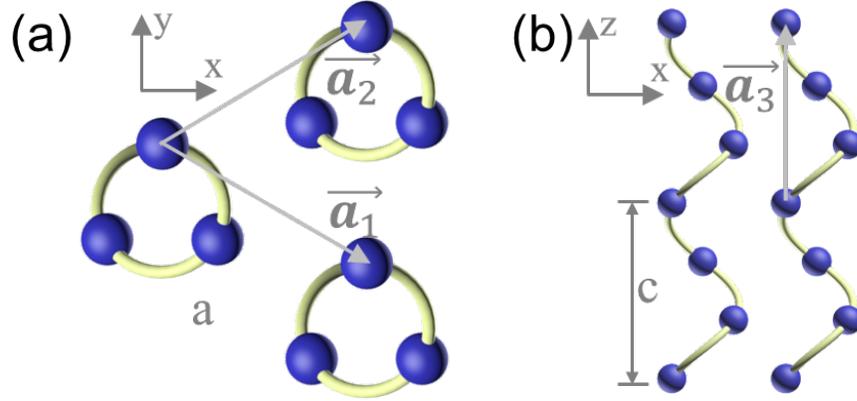
Fig. 1.2. Orthographic View of Te crystal.(a) Side view and (b) top view of 1D helical chains.

The unit cell of Te consists of three neighboring atoms along the chain, each has a 120° rotational shift in xy plane and an offset of 1.97 Å in z direction. The space group of Te crystal is either $P3_121$ (D_3^4) or $P3_221$ (D_3^4), depending on the clockwise or counterclockwise rotational directions [40–42]. By identifying the unit cell, we can define the unit vectors in the real space to be $\vec{a_1} = a\hat{x}, \vec{a_2} = \frac{1}{2}a\hat{x} + \frac{\sqrt{3}}{2}a\hat{y}, \vec{a_3} = c\hat{z}$ (here a and c are atom spacing as denoted in Figure 1.2a and 1.2b), and the corresponding reciprocal lattice vectors can be expressed easily by taking reciprocal triad of unit vectors. The first Brillouin zone is defined by taking the Wigner-Seitz cell in reciprocal space and is illustrated in Figure 1.3a.

As a direct consequence of lacking inversion symmetry and heavy atoms, Te exhibits strong spin-orbit coupling (SOC), which gives rise to a spin-split conduction band with a Weyl crossing point in the conduction band edge [42], and a famous camel-back-shaped valence band edge [40, 43, 44]. These prominent features near the band edge will have an influence on the transport behavior and will be manifested in the magneto-transport and quantum Hall effect as we shall discuss later.
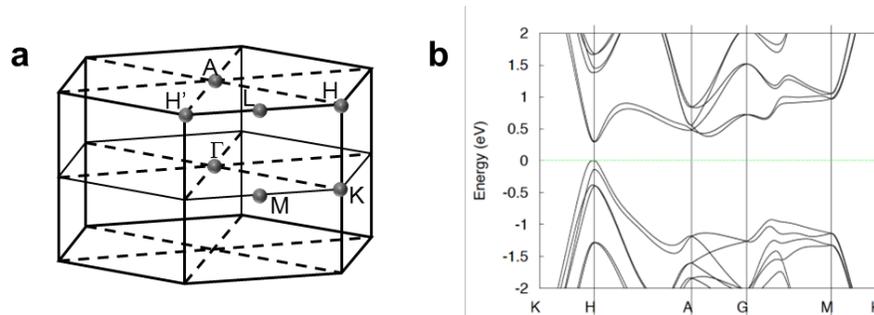
Fig. 1.3. Orthographic View of Te crystal.(a) First Brillouin zone of Te. (b) Band structure of Te from DFT calculations. The direct band gap of 0.35 eV is located at the corner point H and H' of BZ.

Because of the unique 1D crystal structure, Te not only tends to grow into 1D nanowires in general, but also can be arranged into 2D films with proper growth technique. We shall see in this dissertation that 2D Te films down to 0.3 nm which is a monolayer of Te atoms (half of the unit cell thickness) can be grown with liquid-based growth method that we developed. The monolayer or few-layer tellurium film is coined as tellurene, as an analogy to graphene, phosphorene, and stanane. In this work, more generally, we use the word tellurene to refer to all the 2D Te films we grow with hydrothermal method regardless of the thickness. The films show great air-stability over several months time span. The mobility of both electrons and holes are high and near symmetric, which ensures its potential to be used as a FET channel material for CMOS circuits.

1.4   Summary

This report will be focusing on three major topics regarding tellurene: the material growth and characterization; electrical properties and FET device application, and magneto-transport. The dissertation is organized as following:

In **Chapter 2** we will introduce our initial effort with collaborators to develop and improve a hydrothermal growth method to obtain large-area high-quality 2D tellurene. This is the first time 2D Te films (from tens of nanometers down to few

layers) are acquired from a bottom-up synthesis process. Comprehensive techniques were employed to characterize the quality of the films including TEM, AFM, XRD and Raman spectroscopy. The thickness-dependent and strain-response Raman spectrum captures the physical transition as the material approaches lower dimension.

In **Chapter 3** we thoroughly investigated the electrical properties of tellurene and explored high performance p-type FETs based on Te films. The p-type Te transistors exhibits highest on-state drive current over 1A/mm among all 2D material based transistors with high hole mobility near 700 cm^2/Vs and decent on/off ratio over 10^6. The device scaling were also demonstrated with channel length down to 100 nm and EOT down to 2.5 nm. Record-low contact resistance were achieved using high work function metal or using chemically converted lateral contacts. The top gate device were also demonstrated using PVD grown gate stacks or self-aligned aluminum top gate. Finally, Te nanowire transistors were also realized.

In **Chapter 4** we report Te NMOS and CMOS devices along with other device applications. ALD dielectric doping was successfully implemented to achieve n-type doping effect. NMOS device with high electron mobility near 600 cm^2/Vs and proto-typical CMOS inverter were demonstrated. We also broadened our horizon to explore the thermoelectric properties of 2D Te films. The thermoelectrical figure-of-merit ZT value was boosted to 0.63 and this is so far the highest thermoelectric efficiency in single element materials. Photo/thermoelectric current mapping were carried out to visualize the thermoelectric and photoelectric current distribution. Accumulation-type contacts were achieved in p-type 2D semiconductor for the first time.

Chapter 5 covers magneto-transport behavior in both p-type and n-type Te samples. Shubnikov-de Haas oscillations and quantum Hall effect were first reported in high quality p-type tellurene with Hall mobility near 3,000 cm^2/Vs at cryogenic temperature. Anomaly in both SdH oscillations and transport behaviors was observed which can be explained by the interplay between SOC and Zeeman splitting effect. The Magneto-resistance along z-directions shows some evidence of structure induced 1D transport behavior. Higher electron mobility of 6,000 cm^2/Vs were achieved in

ALD doped n-type device, allowing more exotic physics phenomena to be unveiled. Because of the unique doping profile, correlated wide quantum well with approximate SU(8) symmetric pseudospin space were realized in well-developed quantum Hall states. Non-trivial π Berry phase were detected in SdH oscillations, suggesting the first experimental observation of massive Weyl fermions in unprecedented Weyl semiconductor system.

2. SYNTHESIS AND CHARACTERIZATION OF TELLURENE FILMS

2D materials are defined as a group of materials featuring atomic-thin layered crystal structure with interlayer vdW force. Through high-throughput vdW density functional calculations (DFT), over five thousand materials were identified with vdW structure, yet only about 30% of them can be easily exfoliated [45]. Tellurium is a special 2D material in a sense that it forms 1D atomic chain with vdW forces between neighboring chains. Still atomically thin 2D Te films can theoretically be achieved with perfect vdW interface. Unfortunately, Te falls into the majority of 2D materials which cannot be easily exfoliated with typical mechanical method USING scotch tape. Hence all the previous works on Te were focused on its bulk form or evaporated poly-films [46]. The quest for high quality single crystalline 2D Te films is urgent to explore the electrical and physical properties of Te approaching 2D limit. In this chapter we will first report a hydrothermal growth method to synthesize 2D Te films. This is the first time large-area single crystalline 2D Te films were obtained. The method provides controllability of film thickness and later size, and allows the film to be assembled onto arbitrary substrates. TEM and AFM techniques were employed to determine the crystal quality nd thickness of the film. Finally, we will discuss the anisotropic optical properties along with strain response to shed light on crystal structure-property correlations of Te with its unique atomic structure.

2.1 Material Synthesis and Assembly

In general, the most widely used methods to acquire 2D thin films from van der Waals materials are mechanical exfoliation and chemical vapor deposition (CVD). Significant efforts have also been made to grow tellurium nanostructures, however

these methods yield either quasi-one-dimensional morphology [47–52] or small 2D flakes [53] that are unsuitable for studying magneto-transport. It is also very difficult to study transport properties of monolayer tellurene grown on conducting graphene surface by (MBE) molecular beam epitaxy [54,55] since it requires monolayer transfer and process [56–58]. In this section, we report a substrate-free solution process for synthesizing large-area, high-quality 2D Te crystals (termed tellurene) with a thickness of a monolayer to tens of nanometers and a unique chiral-chain vdW structure which is fundamentally different from the layered vdW materials. We use the term X-ene to describe 2D forms of elemental materials without considering the specific bonding [58, 59]. The samples are grown through the reduction of sodium tellurite (Na_2TeO_3) by hydrazine hydrate (N_2H_4) in an alkaline solution at temperatures from 160-200 °C, with the presence of crystal-face-blocking ligand polyvinylpyrrolidone (PVP).
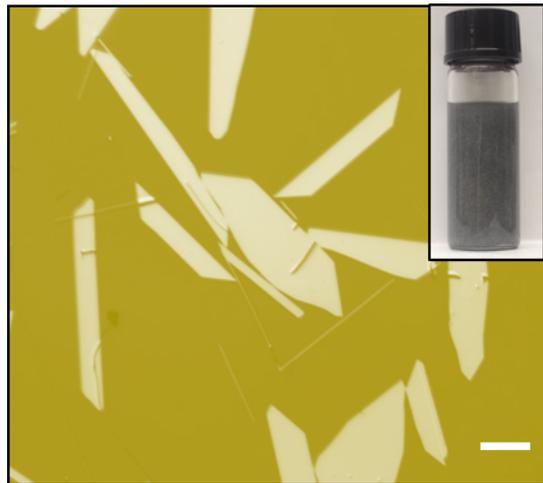

Fig. 2.1. Optical image of solution-grown tellurene flakes. Inset: Optical image of the tellurene solution dispersion. The scale bar is 20 μm.

In a typical procedure, analytical grade Na_2TeO_3 (0.00045 mol) and a certain amount of poly(-vinyl pyrrolidone) was put into double distilled water (33 ml) at room temperature under magnetic stirring to form a homogeneous solution. The

resulting solution was poured into a Teflon-lined stainless-steel autoclave, which was then filled with an aqueous ammonia solution (25%, w/w%) and hydrazine hydrate (80 %, w/w%). The autoclave was sealed and maintained at the reaction temperature for a designed time. Then the autoclave was cooled to room temperature naturally. The resulting silver-gray, solid products were precipitated by centrifuge at 5000 rpm for 5 minutes and washed 3 times with distilled water (to remove any ions remaining in the final product).

Figure 2.1 shows the as-grown Te nanofilms and the inset is an optical image of a typical tellurene solution dispersion after reactions at 180 °C for 20 hours when the Na_2TeO_3:PVP mole ratio is 52.4:1. Individual 2D flakes have edge lengths ranging from 50 to 100 μm, and thicknesses from 10 to 100 nm.

Tellurene crystals with a thickness smaller than 10 nm to ultimately monolayer structure can be further derived through a solvent-assisted post-growth thinning process. The as-synthesized 2D tellurene solution (1 mL) was mixed with acetone (3 mL) at the room temperature. After a specific time (e.g., 6 hours), the thin 2D tellurene can be obtained by centrifuge at 5000 rpm for 5 minutes. With L-B process, the 2D tellurene can be transferred onto the substrate.

For thinning process using tellurene solution with controlled pH values, the suspension of as-synthesized 2D Te (1 mL) was centrifuged with the addition of 3 mL DI water. Then, the 2D Te was dispersed into a solution of 1 mL of NaOH and 3 mL of acetone. The concentration of NaOH was varied to control the pH value of the above 4 mL solution. After that, the above solution was kept at room temperature for 2-10 hours. Finally, the thinned tellurene samples were precipitated by centrifuge. The thickness of tellurene decreases with time after acetone is introduced into the growth solution. After 6 hours, the average thickness of tellurene is reduced to $\sim$ 10 nm, with the thinnest flake down to 4 nm thick ($\sim$ 10 layers) (Figure 2.2). Due to the poor solubility in acetone, PVP molecules tend to desorb from the tellurene and undergo aggregation, giving rise to the sediment of tellurene over the time in acetone. Lacking the protection of PVP, the tellurene surfaces get exposed and react with the alkaline
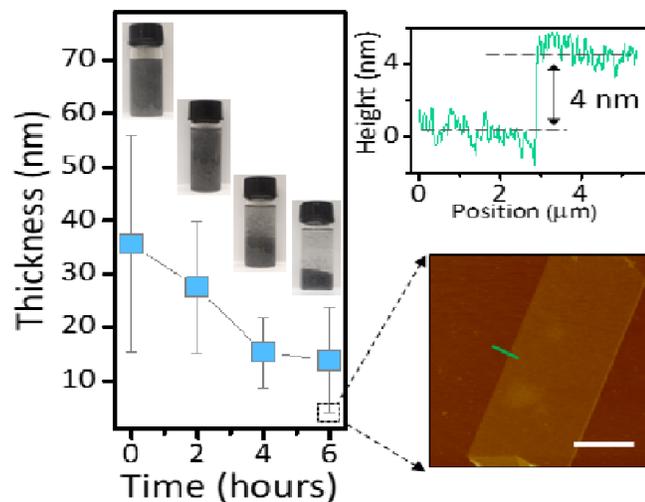
Fig. 2.2. Post-growth thinning process in the alkaline growth solution (pH $\sim$ 11.5) for obtaining ultrathin few-layer tellurene. The scale bar is 5 μm. Mean values from 8 technical replicates are indicated. Error bars represent s.d.

growth solution (pH $\sim$ 11.5), leading to the reduced thickness. Large-area (up to 100 μm in lateral dimensions) tellurene crystals with monolayer, bi- layer, tri-layer and few-layer thicknesses can be further obtained (Figure 2.3), by controlling the pH values of the tellurene dispersion solution in the above post-growth thinning process.
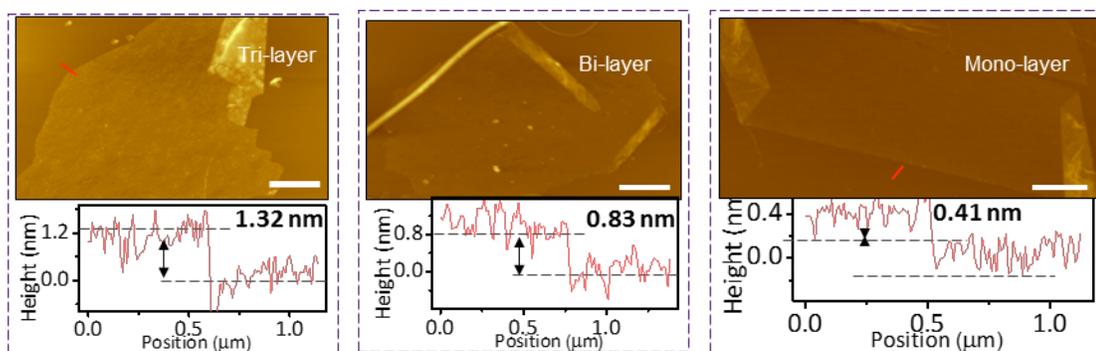
Fig. 2.3. Tri-layer, bi-layer and mono-layer tellurene samples obtained after the post-growth thinning process (pH = 10.5) The scale bar is 5 μm.

The 2D Te flakes can be transferred and assembled at large scale into a single layer of continuous thin film through a Langmuir-Blodgett (LB) process [60] onto various substrates for subsequent characterization and device integration. The washed nanoflakes were suspended in a mixture solvent made of N, N-dimethylformamide (DMF) and $CHCl_3$ (e.g., in the ratio of 1.3:1). Then, the mixture solvent was dropped into the deionized water. Too much DMF will result in the falling of 2D Te in the water. It is difficult to mix the DMF, $CHCl_3$ and 2D Te when $CHCl_3$ is too much. After the evaporation of the solvent, a monolayer assembly of 2D Te flakes was observed at the air/water interface. Then we can transfer the monolayer assembly of 2D Te onto the substrates.

2.2 Crystal Growth Mechanism and Geometric Control

The controlled PVP concentration is the key for obtaining 2D tellurene. Figure 2.4 shows the productivity of tellurene grown at 180 °C with time for a broad range of Na_2TeO_3/PVP mole ratios. When a smaller amount of PVP is used, the first 2D structures occur after a shorter reaction time (Figure 2.4a). A closer examination of reactions with different PVP concentrations reveals an intriguing morphology evolution in growth products with time. For each PVP concentration, the initial growth products are dominantly 1D nanostructures (Figure 2.4b), similar to previous reports [51, 61, 62]. After a certain period of reaction, structures possessing both 1D and 2D characteristics start to emerge (Figure 2.4a). TEM characterizations indicate that the long axes (showing 1D characteristics) of these flakes are $\langle 0001 \rangle$ oriented, and the lateral protruding regions (showing 2D characteristics) grow along the $\langle 1\bar{2}10 \rangle$ directions, with the $\{10\bar{1}0\}$ facets as the top/bottom surfaces. The 2D regions are enclosed by edges with atomic level step roughness. These high energy edges are not specific to certain planes during the intermediate states. These structures also have more uneven surfaces compared to 2D tellurene, further manifesting their intermediate nature. Finally, the ratio of 2D tellurene flakes which have a straight $\{1\bar{2}10\}$ edge

increases with a reduction in 1D and intermediate structures and reaches a plateau after an extended growth, e.g. 30 hours. The growth with a lower level of PVP has a smaller final productivity. The observed morphology evolution suggests that the balance between the kinetic and thermodynamic growth dictates the transformation from 1D structures to 2D forms (Figure 2.4b). In the initial growth, PVP is preferentially adsorbed on the $\{10\bar{1}0\}$ surfaces of the nucleated seeds, which promotes the kinetic-driven 1D growth. When the reaction continues, $\{10\bar{1}0\}$ surfaces of the formed structures would become partially covered due to the insufficient PVP capping. Since $\{10\bar{1}0\}$ surfaces have the lowest free energy in tellurium, the growth of $\{10\bar{1}0\}$ surfaces along the $\langle 1\bar{2}10 \rangle$ direction significantly increases through the thermodynamic-driven assembly, giving rise to the observed intermediate structures. The enhanced growth along the $\langle 1\bar{2}10 \rangle$ directions together with the continued $\langle 0001 \rangle$ growth leads to the formation of 2D tellurene.

The sizes and thicknesses of tellurene can also be effectively modulated by controlling the ratio between sodium tellurite and PVP (Figure 2.4c). The width of tellurene monotonically decreases with the reduction of PVP level; the thickness is minimized when a medium level of PVP is used (e.g., Na_2TeO_3/PVP ratio $\sim 52.4/1$, Group No. 12 in Figure 2.4c), and increases with both the increase and decrease of PVP (Figure 2.4c). With a small amount of PVP, the solution is supersaturated with Te source, and homogeneous nucleation of Te can occur in large scale, consuming resource for subsequent growth. As a result, the Ostwald ripening of Te nuclei is shortened, and the final tellurene crystals have smaller sizes compared to samples grown at higher PVP concentrations. The low PVP level also leads to more significant growth along thickness directions. On the other hand, when the PVP level is high, the fewer nucleation events allow the sufficient supply of Te source for subsequent growth, leading to the increased width and thickness. Also, the productivity of tellurene increases with the reaction temperature from 160 °Cto 180 °C This is likely because higher temperature promotes the forward reaction rate in the half reaction of endothermic hydrazine oxidation. However, when temperature increases from 180 °C to 200 °C
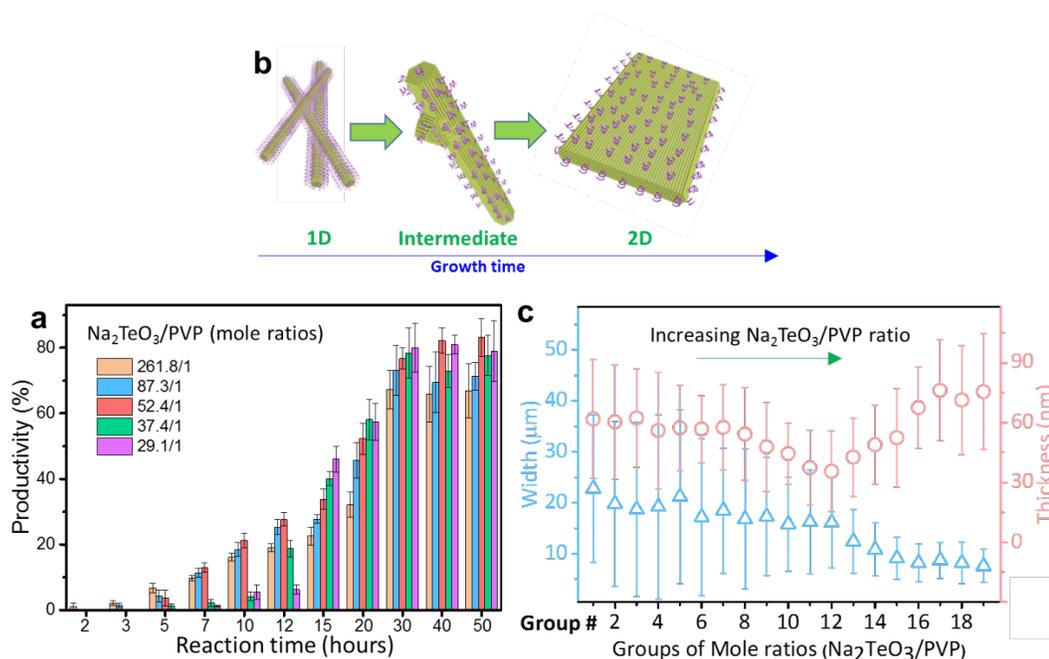
Fig. 2.4. Solution processing for tellurene. (a), Growth outcome for different PVP concentrations with different reaction time. Mean values from 5 technical replicates are indicated. Error bars represent s.d.(b) Morphology evolution from 1D Te structures to 2D Te. (c) Thickness and width modulation of 2D Te. Mean values from 8 technical replicates are indicated. Error bars represent s.d.

the possible breaking of the van der Waals bonds between Te chains by the excessive energy could lead to the saturated productivity.

2.3 Crystal Structure and TEM Analysis

Te has a unique chiral-chain crystal lattice where individual helical chains of Te atoms are stacked together by van der Waals (vdW) type bonds and spiral around axes parallel to the [0001] direction at the center and corners of the hexagonal elementary cell (Figure 2.5a). Each tellurium atom is covalently bonded with its two nearest neighbors on the same chain. Earlier studies revealed bulk Te has small effective masses and high hole mobilities due to spin-orbit coupling [63]. The lone-pair and

anti-bonding orbitals give rise to a slightly indirect bandgap in the infrared regime
(∼0.35 eV) in bulk Te [64], which has a conduction band minimum (CBM) located
at the H-point of the Brillouin zone, and a valence band maximum (VBM) that is
slightly shifted from the H-point along the chain direction, giving rise to hole pockets
near H-point40. When the thickness is reduced, the indirect feature becomes more
prominent, as shown by our first-principles calculations. For example, the VBM of
4-layer Te (Figure 2.5b) is further shifted to (0.43, 0.34) (in the unit of the surface
reciprocal cell), while CBM remains at (1/2, 1/3). Accompanied by the shift of VBM,
the band gap also increases (Figure 2.5c), due to the quantum confinement effect, and
eventually reaches ∼ 1 eV for monolayer Te [59].
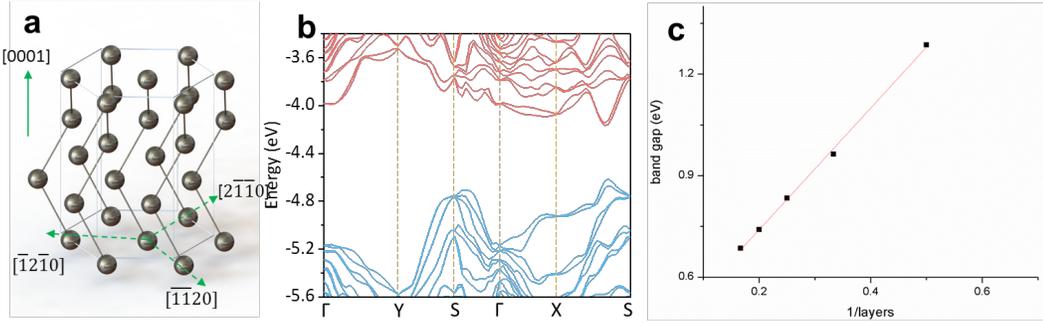
Fig. 2.5. Band structure of few-layer tellurene. (a) Atomic structure of
tellurium. (b) The band structure of 4-layer Te, calculated by using
PBE functional. Valence bands are shown in blue, and conduction
bands are in red. (c) Thickness-dependent bandgap for tellurene,
calculated by HSE functional.

The structure, composition, and quality of these tellurene crystals have been an-
alyzed by high angle annular dark field scanning transmission electron microscopy
(HAADF-STEM), high-resolution transmission electron microscopy (HRTEM), en-
ergy dispersive X-ray spectroscopy (EDS), and X-ray diffraction (XRD). Figure 2.6a
shows a typical atomically-resolved HAADF-STEM image of a tellurene flake. The
helical chains and a threefold screw symmetry along ⟨0001⟩ are clearly visible. The
inter-planar spacing is 2.2 and 6.0 , corresponding to Te (1$\bar{2}$10) and (0001) planes [65],

respectively. No point defects or dislocations were observed over a large area within single crystals. Figure 2.6b shows the selective area electron diffraction (SAED) pattern along the $[10\bar{1}0]$ zone axis, which is perpendicular to the top surface of the flake. Similar characterizations and analyses of dozens of 2D Te flakes with different sizes indicate that all samples grow laterally along the $\langle 0001 \rangle$ and $\langle 1\bar{2}10 \rangle$ directions, with the vertical stacking along the $\langle 10\bar{1}0 \rangle$ directions (Figure 2.6c).
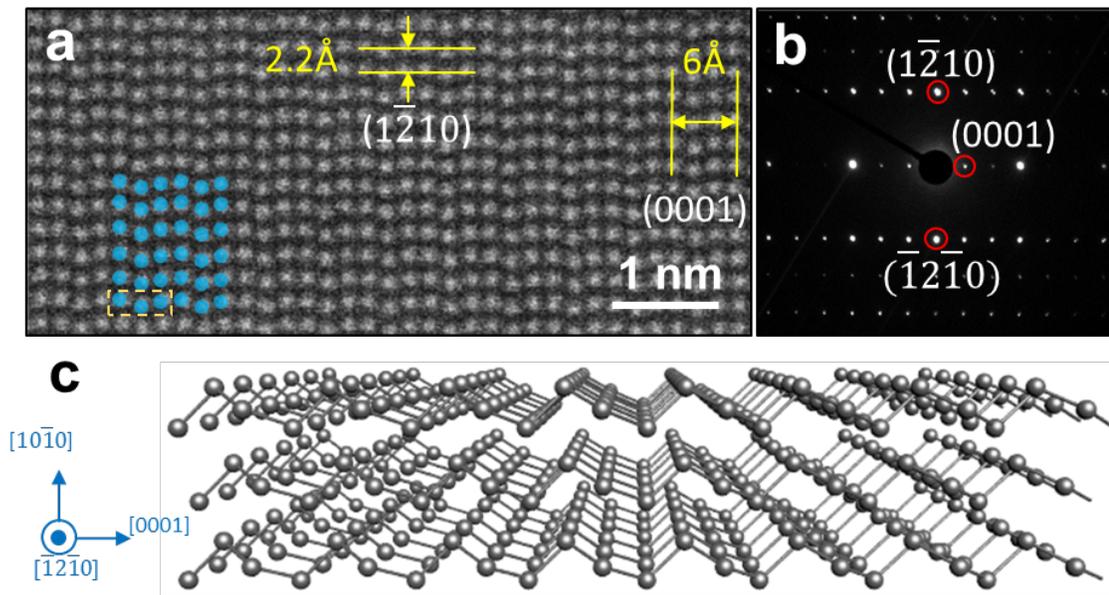
Fig. 2.6. TEM image of few-layer tellurene. (a) (HAADF)-STEM image of tellurene. The false-colored (in blue) atoms are superimposed to the original STEM image for highlighting the helical structure. (b) Diffraction pattern of tellurene. (c) 3D illustration of tellurene structure.

2.4 Thickness and Angle-Dependent Raman Spectroscopy

These high-quality ultrathin tellurene crystals with controlled thicknesses provide an ideal system to explore their intrinsic properties in the 2D limit. We first characterized the optical properties of as-synthesized tellurene with a wide range of thickness (from a monolayer to 37.4 nm) by angle-resolved polarized Raman spec-

troscopy at room temperature. The incident light comes in along the $[10\bar{1}0]$ direction and is polarized into the $[0001]$ helical chain direction of the tellurene. The Raman spectra of tellurene samples with different thickness (Figure 2.7a) exhibits three main Raman-active modes, with one A-mode and two E-modes which correspond to the chain expansion in basal plane, bond-bending around $[1\bar{2}10]$ direction and asymmetric stretching mainly along $[0001]$ helical chain [66], respectively. For the 2D Te samples thicker than 20.5 nm, three Raman-active modes locating at 92 cm^{-1} (E_1 transverse (TO) phonon mode), 121 cm^{-1} (A_1-mode) and 143 cm^{-1} (E_2-mode) were identified, which agrees well with previous observations in bulk and nanostructured tellurium [53,67–69], indicating that although these thicker crystals possess 2D morphology, their symmetric properties can still be characterized as bulk. The appreciable effective dynamic charge induced for the E_1 mode in tellurium leads to a split of E_1 doublets at 92 cm^{-1} and 105 cm^{-1} for transverse (TO) or longitudinal (LO) phonons, respectively [68]. The absence of E_1 (LO) mode in our observed results for 2D Te thicker than 20.5 nm, similar to previous reports on bulk and nanostructured tellurium [53,67–69], may be attributed to the different signs in the deformation potential and electro-optic contribution to the Raman scattering tensor, which gives rise to the cancellation if both contributions have the same magnitude [70]. As the thickness decreases from 20.5 nm to 9.1 nm, the deformation potential in tellurene lattice increases while the electro-optic effect weakens, leading to the appearance of E_1 (LO) mode in the Raman spectra for 2D Te crystals with intermediate thickness. When the 2D Tes thickness further reduces (smaller than 9.1 nm in Figure 2.7a), the degeneracy in the E_1 TO and LO modes occurs with peak broadening, possibly due to the intra-chain atomic displacement, the electronic band structure changes and the symmetry assignments for each band, all of which are affected by the sample thickness.

hen tellurenes thickness decreases, there are significant blue-shifts for both A_1 (shift to 136 cm^{-1} for monolayer) and E_2 modes (shift to 149 cm^{-1} for monolayer). The hardened in-plane E_2 vibration mode in thinner tellurene, similar to reported ob-
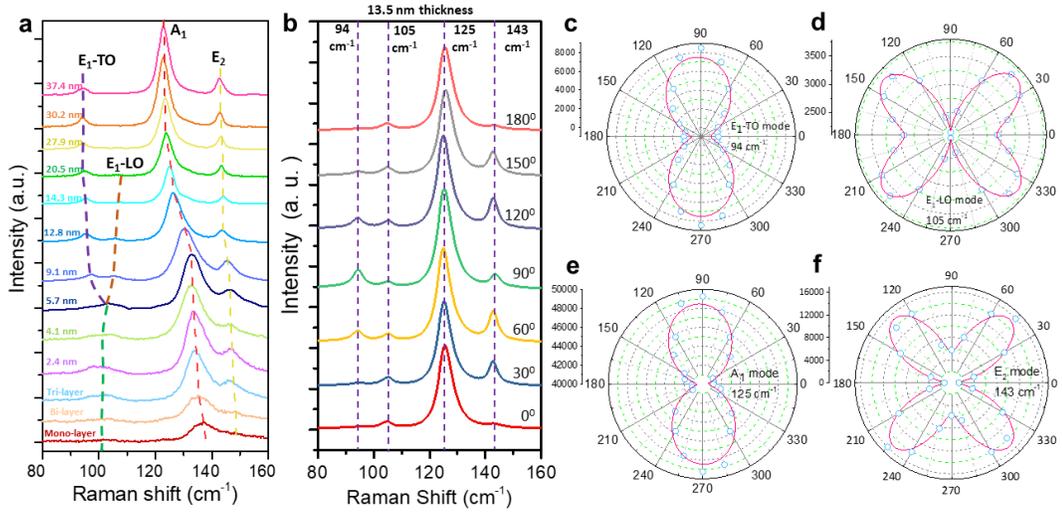
Fig. 2.7. (a) Raman spectra for 2D Te with different thicknesses. (b) - (f) Angle-resolved Raman spectra for a 13.5-nm-thick flake. b, Evolution with angles between crystal orientation and incident laser polarization. (c) - (f) Polar figures of Raman Intensity corresponding to A_1 and two E modes located at 94 (E_1-TO), 105 (E_1-LO), 125 (A_1), and 143 (E_2) cm^{-1}.

servations for black phosphorus [71] and MoS_2 [72], may be attributed to the enhanced interlayer long-range Coulombic interactions when thinned down. The observed blue-shift for the A_1 mode in 2D Te, in strong contrast to 2D layered vdW materials which usually witness red-shift for the out-of-plane vibration mode when thinned down, is thought to be closely related to the unique chiral-chain vdW structure of tellurene. When thinned down, the lattice deformation within the 2D plane gave rise to the attenuated inter-chain vdW interactions and enhanced intra-chain covalent interactions in the individual tellurene layer, leading to more effective restoring forces on tellurium atoms and hence hardened out-of-plane A_1 vibration mode. Such unique structure of tellurene also results in the giant thickness-dependent shift in Raman vibrational modes, which is unseen in 2D layered vdW materials. The interaction between the substrate (SiO_2/Si) and 2D Te flakes could also contribute to the hardened A_1 and

E_2 modes. The stiffening of vibrational modes in monolayer tellurene (Figure 2.7a) is consistent with its structure reconstruction where extra bonds are formed between neighboring chains in the single layer tellurium [58, 59].

Reduced in-plane symmetry in the chiral-chain vdW structure of tellurene indicates a strong in-plane anisotropy for its material properties. We further characterized the anisotropic optical properties of as-synthesized tellurene with three different thicknesses (28.5 nm, 13.5 nm, and 9.7 nm) by angle-resolved polarized Raman spectroscopy at room temperature. By rotating the tellurene flakes in steps of 15°, we observed the changes in the angle-resolved Raman peak intensities (Figure 2.7b). We extracted the peak intensities of different modes by fitting with Lorentz function and plotted them into the corresponding polar figures (Figure 2.7c-f). While all the modes change in intensity with the polarization angle, we find that the peak for the A_1 mode in all samples exhibits the largest sensitivity to the relative orientation between the [0001] direction and the polarization of the excitation laser (middle panels of Figure 2.7b). The angle-resolved Raman results also confirm that the helical Te atom chains in the as-synthesized tellurene are oriented along the growth direction of the tellurene flake, which matches the TEM results (Figure 2.6a).

2.5 Anisotropic Strain Response of Raman Spectroscopy

We also investigated the evolution of the Raman spectra of Te with uniaxial tensile and compressive strains, summarized in Figure 2.8a. The laser polarization is aligned along the a-axis of Te thin film, and the strain direction is along c-axis based on our apparatus set-up. In our work, we used Lorentzian function to fit the Raman spectra and obtained the peak frequency of each mode at different strain strengths. For unstrained Te, consistent with previous reports [69, 73], we observe the A_1 mode at 122 cm^{-1}, and modes of E_1 and E_2 at 94 cm^{-1} and 142 cm^{-1}, respectively. The A_1 and E_2 modes show the same linear trend of Raman frequency shift with respect to the applied strains, while the rates of frequency shift are different

in these two modes. Both A_1 and E_2 modes experience a blue-shift when Te is under compressive strains along the c-axis, with a slope of 1.1 cm^{-1}%$^{-1}$ and 0.9 cm^{-1}%$^{-1}$, respectively. On the other hand, A_1 and E_2 have a red-shift at a rate of cm^{-1}%$^{-1}$ and 1.2 cm^{-1}%$^{-1}$ under uniaxial tensile strains along the c-axis, as shown in Figure 2.8b and 2.8c. Note that we did not observe a measurable Raman shift in the E_1 mode, where the E_1 peak position remains the same with various c-axis strains and we ascribe it to the fact E_1 mode is responsible to a-axis rotation and is not sensitive to c-axis deformation [68,69]. The different responses of Raman spectra with strains can be explained by analyzing the types of vibration mode involved. Let us take the E_2 mode as an example in the first place, where the atomic motions of E_2 mode occurs along the 1D c-axis direction. The red-shift of the E_2 mode under tensile strain along the c-axis, with a slope of cm^{-1}%$^{-1}$, can be understood based on the elongation of the Te-Te covalent bond length, which weakens the interatomic interactions and therefore reducing the vibration frequency. Meanwhile, blue-shift with a slope of 0.9 cm^{-1}%$^{-1}$ under compressive strain indicates the enhancement of interatomic interaction, thus interpreted as a result of the shortened covalent Te-Te bond under compressive deformation. Furthermore, tensile strain not only enlarges the Te-Te bond length assigned to E_2 mode along c-axis, but also influences the basal plane displacement pattern which is associated with A_1 mode. The red-shifted/blue-shifted Raman frequency of the A_1 mode is attributed to the decreased/increased equilateral triangle projection of the chain on basal plane perpendicular to the c-axis, thus manipulating the basal plane vibration frequency and leading to Raman shift of A_1 mode.

To apply strain along the a-axis, the Te sample substrate was rotated by 90°, and the Raman spectroscopy was introduced along the c-axis on the same sample. The corresponding Raman spectra of a-axis strained Te are presented in Figure 2.8d, where the E_1 mode has disappeared due to the optical anisotropic property reported previously that E_1 mode maximizes when Raman polarization is along a-axis, and vanishes when it is along c-axis19. Figure 2.8e and 2.8f illustrate the A_1 and E_2 peak

positions as a function of tensile and compressive a-axis strains. Interestingly, both A_1 and E_2 have no response with various tensile and compressive strains, and the A_1 and E_2 Raman peak positions are independent of applied strains. The response along a-axis strain is totally different from that along c-axis, providing strong evidences of its anisotropic behavior. More importantly, the significant strain response along c-axis, together with no response along a-axis has conclusively verified the 1D van der Waals nature of Te thin film. The pronounced strain response when the deformation is applied along c-axis is directly associated with interatomic interactions between 1D covalent Te-Te bonds, while the absence of strain response in a-axis strains demonstrates no covalent bond, but pure weak van der Waals interaction in 2D plane of Te thin films.

2.6 Summary

The single element 2D materials are some of the most well-known 2D materials, not only because of its simple crystal and electronic structures, but also because they are beautiful systems with profound and intriguing physical phenomena. For example, graphene hosts massless Dirac fermions that can be described with relativistic Dirac Hamiltonian; Stanane is predicted to be a topological insulator to study quantum spin Hall effect. Our progress in synthesizing 2D Te adds a new member to this exciting family. Unlike conventional 2D semiconductors obtained by mechanical exfoliation which only yield small nanofilms, our 2D Te films have lateral size over 10^3 um^2 which is about two orders larger than other exfoliated 2D materials and shows much more promising manufacturing potential. The AFM results show that the films have an atomically flat surface, and the controllable thickness can be tuned from tens of nanometers all the way down to few layers. TEM image determines the crystal orientation and also confirms astonishingly high crystal quality. The thickness-dependent Raman spectroscopy shows the phonon vibration modes are shifted as we approaching 2D limit. And anisotropic strain response of Raman spectroscopy also reveals the

1D nature of 2D Te. The synthesis and characterization results paved the way for implementing Te-based electronics and further study the quantum transport of 2D Te.
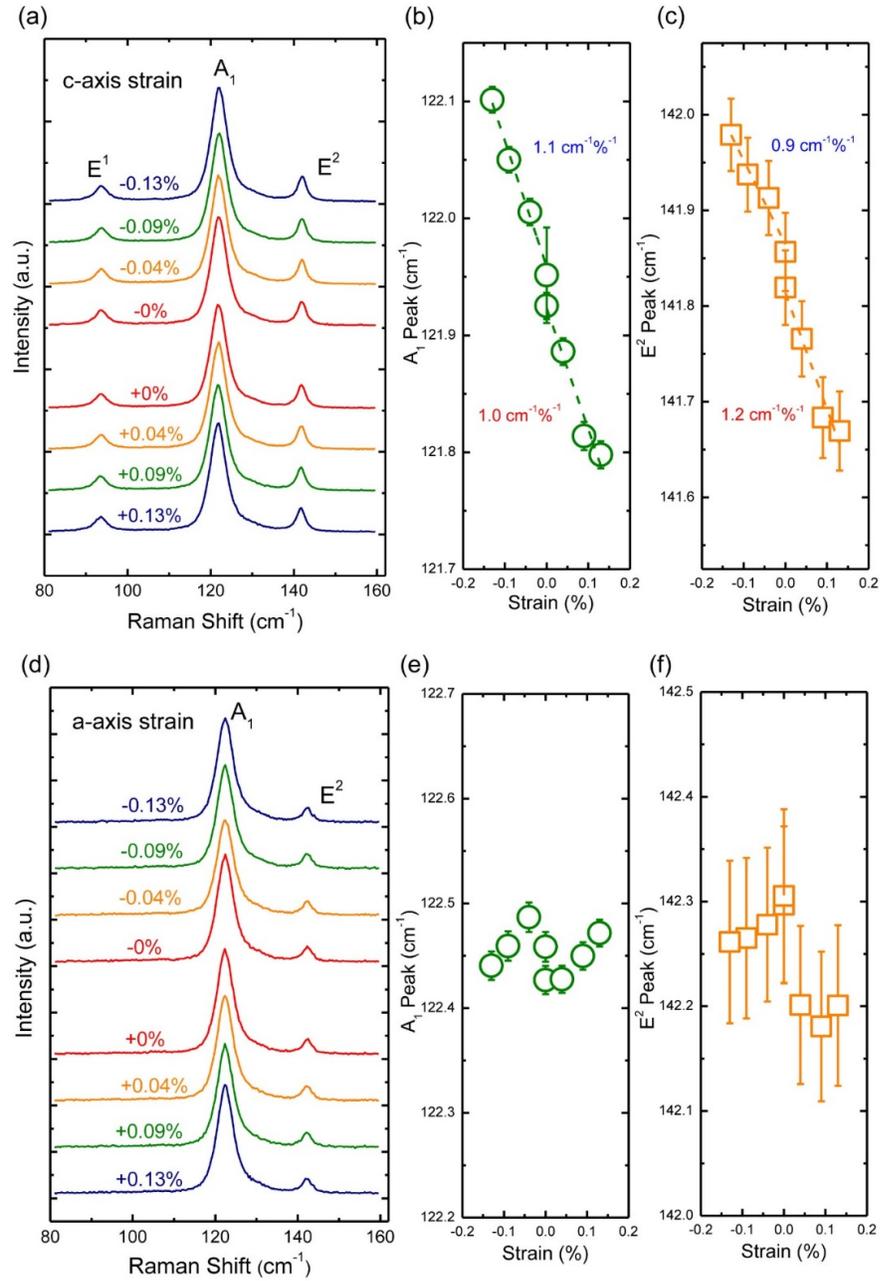
Fig. 2.8. Raman evolution under uniaxial strained Te. (a) Raman spectra of Te thin film for both tensile and compressive c-axis strains. Raman shift of (b) A_1 and (c) $E_2$ modes in c-axis strained Te. (d) Raman spectra of Te thin film for both tensile and compressive a-axis strains. Raman shift of (e) A_1 and (f) E_2 modes in a-axis strained Te. The dashed lines show linear fit results, and error bars are determined from Lorentzian peak fittings.

3. DESIGNING AND OPTIMIZING P-TYPE TELLURENE FETS

In this chapter we will cover a comprehensive investigation of designing and optimizing p-type Tellurene FETs. Due to the unintentional doping of Te, the Fermi level of Te is closer to the valence band and Te exhibits p-type semiconductor behavior in general. Therefore it is simple and straightforward to investigate the electrical properties and build FETs starting from p-type. Here in this chapter, we will first survey the fundamental electrical performance of tellurene as a brand new 2D material with different thickness. Carrier mobility along two major axis will also be measured to determine the preferable direction for fabricating transistors. To design a device that is competitive with state-of-the-art 2D transistors, we scaled the channel length and effective oxide thickness to further boost the on-state current to over 1 A/mm. With high mobility, the drive current and the speed of Te transistors are comparable to top-of-the-line commercial silicon devices. We also thoroughly studied the correlation between the film thickness, channel length, on-current and on/off ratios to serve as a broad guideline in designing tellurene transistors. The contact resistance was also measured with high work function metal. Here we also developed a unique selective chemical transform method to form a lateral contact with low R_c that only specifically works for Te, which further allows us to fabricate high-performance top-gate devices. Finally we present a process to deposit self-aligned top gate stack with promising scaling potential.

3.1   Tellurene Based Transistor Performance

Here we first explored the electrical performance of tellurene field-effect transistors (FETs) to demonstrate its great potential for logic electronics application. Back-gate

devices were fabricated on high-k dielectric substrates and source/drain regions were patterned by electron beam lithography with the channel parallel to the [0001] direction of tellurene. We chose Pd/Au (50/50 nm) as metal contacts since Pd has relatively high work function that can reduce the contact resistance in p-type transistors. Long channel devices were first examined (channel length 3 μm) where the contact resistance is negligible, and the transistor behavior is dominated by intrinsic electrical properties of channel material. Figure 3.1a shows the transfer curve of a typical 7.5-nm-thick 2D Te FET measured at room temperature. The device exhibits p-type characteristics with slight ambipolar transport behavior due to its narrow bandgap nature, with large drain current over 300 mA/mm and high on/off ratio on the order of 10^5. The p-type behavior originates from the high level of Te valance band edge, as shown by our first-principles calculations. Meanwhile, the process-tunable thickness of tellurene allows the modulation of electrical performance in tellurene transistors. Overall, important metrics of tellurene-based transistors such as on/off ratio, mobility, and on-state current level are superior or comparable to transistors based on other 2D materials.

We further investigated the thickness dependence of two key metrics of device performance, namely on/off ratios and field-effect mobilities, for more than 50 2D Te long channel devices with flake thicknesses ranging from over 35 nm down to a monolayer (0.5 nm), to elucidate the transport mechanism of 2D Te FETs (Figure 3.1b). The linear behavior of the output curves in the low $V_d s$ region suggests that the contact resistance is low which ensures the soundness of the field-effect mobility extraction from the slope of the linear region of the transfer curves. The field-effect mobilities of 2D Te transistors peak with $\sim$700 cm^2/Vs at room temperature at around 16 nm thickness and decreases gradually with further increase of the thickness. A benchmark comparison with black phosphorus, which is also a narrow bandgap p-type 2D material, shows that solution-synthesized 2D Te has $\sim$2-3 times higher mobility than black phosphorus when the same device structure, geometry, and mobility extraction method are adopted. This thickness-dependence is similar to other layered mate-
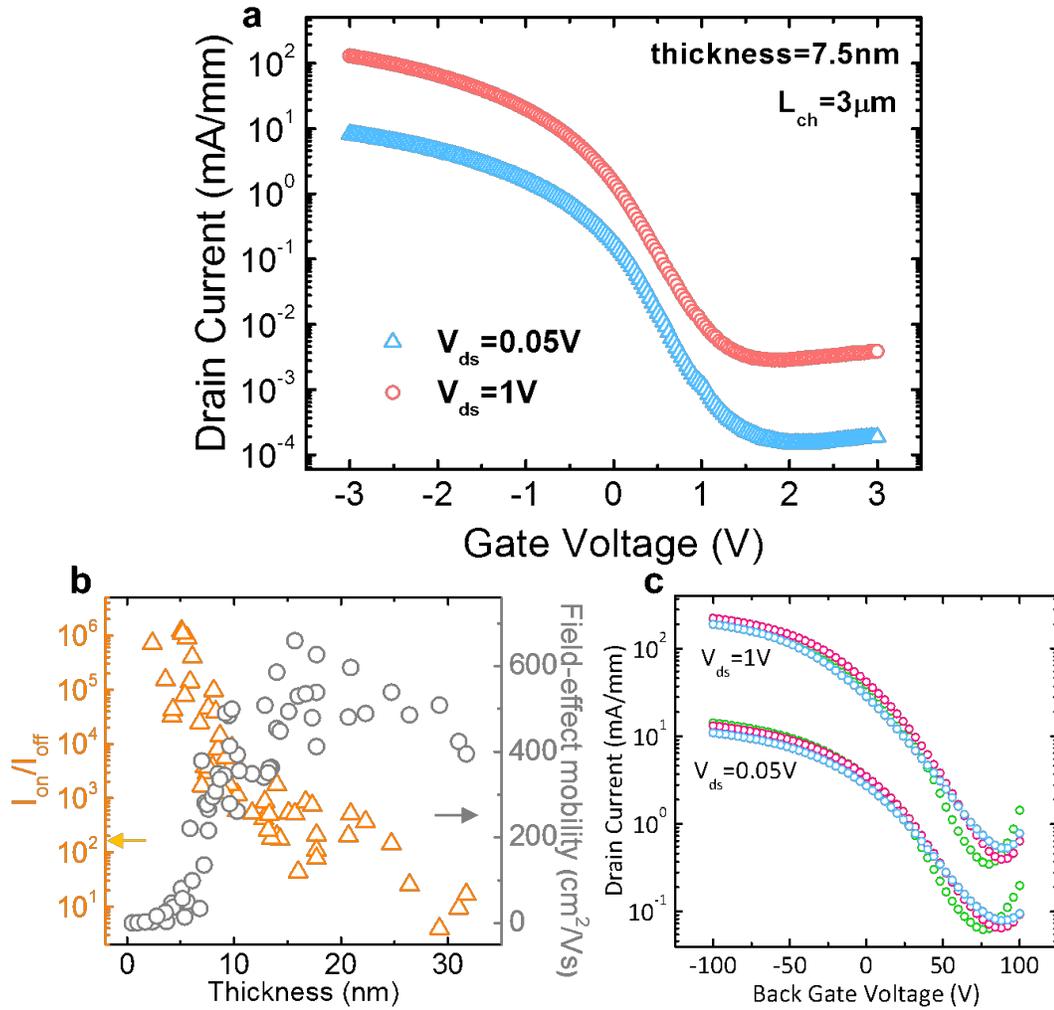
Fig. 3.1. P-type tellurene device performance.(a) transfer curve of a typical long channel tellurene transistors with flake thickness of 7.5 nm. (b) Thickness-dependent on/off ratio (orange triangles) and field-effect mobility (gray circles) for 2D Te transistors. The non-monotonic dependence of mobility on thickness can be fitted using Thomas-Fermi screening model. (c) Air-stability of the same device measured over 2 months.

rials that experience screening and interlayer coupling. The field-effect mobility is also affected by the contribution of the carriers from layers near the semiconductor-oxide interface. Thinner samples are more susceptible to the charge impurities at the interface and surface scattering, which explains the decrease in the mobility of

the few-layer tellurene transistors. We expect to be able to improve the mobility of tellurene through approaches such as improving interface quality with high-k dielectric92 or h-BN encapsulation to reduce the substrate phonon scattering and charge impurity. For bi-layered tellurene transistors, external field-effect mobility is dropped to ~1 cm²/Vs. This is due to bandgap increasing in few-layer tellurene to form much higher Schottky barrier, which may introduce large deviation in extracting mobility due to the drastically increased contact resistance. Because of the reduced gate electrostatic control in thicker flakes, the thickness-dependent on/off ratios steeply decrease from 106 to less than 10 once the crystal thickness approaches the maximum depletion width of the films, with a trend similar to other reported narrow bandgap depletion-mode 2D FETs.

Great air-stability was also demonstrated in tellurene transistors with different flake thickness. Electrical performance of a 15-nm-thick transistor was monitored after being exposed in air for two months without any encapsulation, as shown in Figure 3.1c. No significant degradation was observed in the same device during two-month period, except slight threshold voltage shift probably coming from sequential measurement variation. We further demonstrated that such good air-stability is valid for almost the entire thickness range from thick flakes down to 3 nm. For even thinner flakes, the thin films are no longer conducting after first couple of days.

3.2 Anisotropic Electrical Transport

The in-plane anisotropic electrical transport properties were also studied at room temperature. To minimize flake-to-flake variation and geometric non-ideality, we applied dry-etching method to trim two identical rectangles from the same 2D Te flake. One of the rectangles was aligned along the 1D atomic chain [0001] direction and the other along [12 10] direction (Figure 3.2a). To evaluate the transport anisotropy, long channel FETs (channel length 8 m) were fabricated to minimize contact influence and manifest the intrinsic material properties. The extracted field-effect mobilities
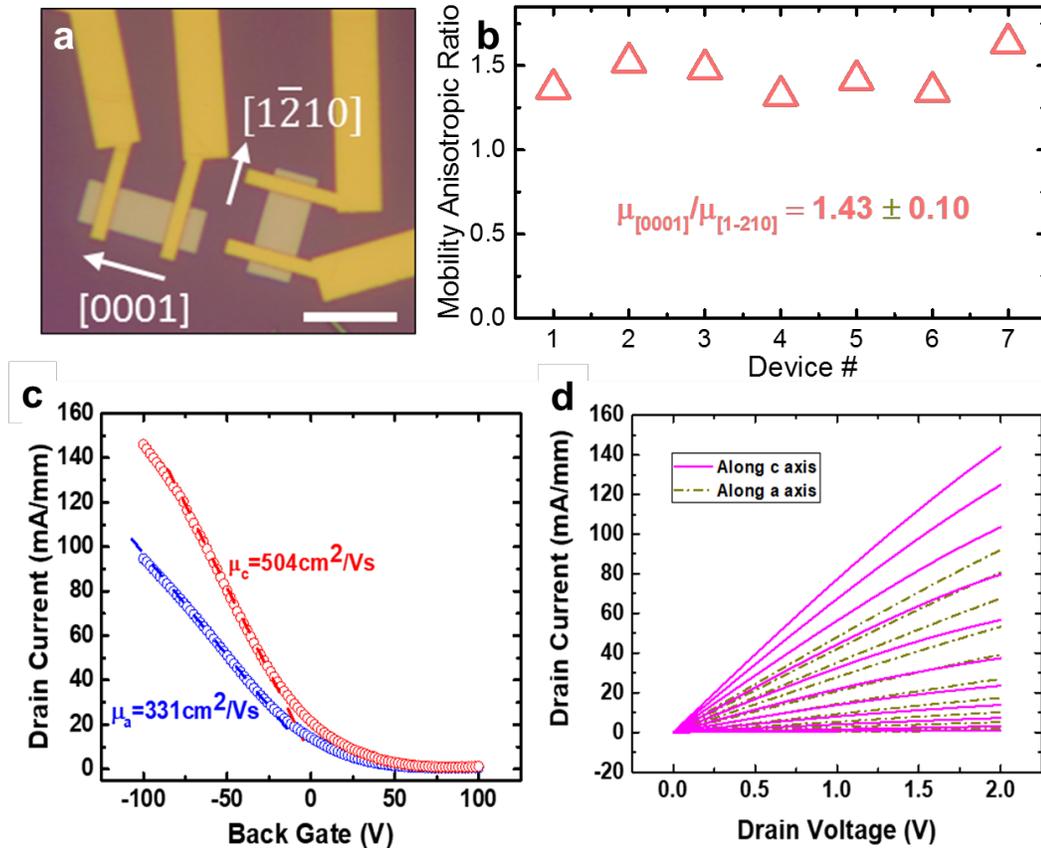
Fig. 3.2. Electrical anisotropy of tellurene. (a) Optical image of a typical device for anisotropic transport measurement. The scale bar is 10 m. (b) Anisotropic mobility measurements along [0001] and [1$\bar{2}$10] directions. (c) Transfer and (d) output curves of a typical set of devices.

along these two primary directions from seven 2D Te samples exhibit an average anisotropic mobility ratio of 1.43±0.10 (Figure 3.2b). A typical set of results measured from a 22-nm-thick sample is shown in Figure 3.2c and 3.2d. This anisotropic ratio in mobility is slightly lower than that reported for bulk tellurium [74], possibly due to the enhanced surface scattering in our ultrathin Te samples. First-principle calculations also show that unusually strong inter-chain coupling in Te [56] is also responsible for the relatively lower electrical anisotropy than one would intuitively expect.

3.3   Device Scaling and Record-high Drain Current
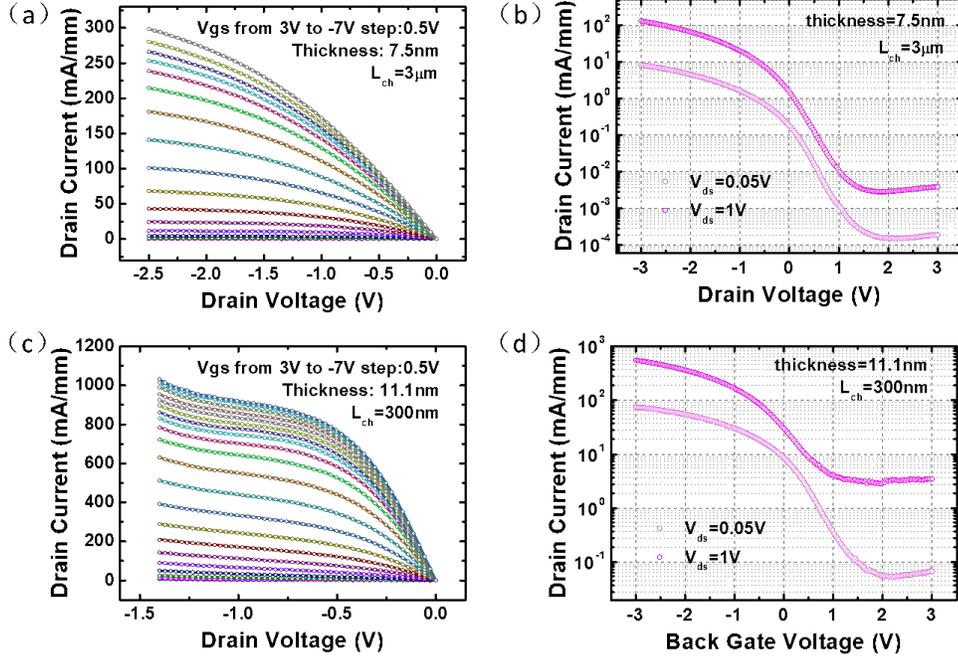
Fig. 3.3. (a) Output curve and (b) transfer curve of a typical long channel tellurene transistors with flake thickness of 7.5 nm. (c) Output curve and (d) transfer curve of a 11.1-nm-thick tellurene transistor with channel length 300 nm.

More strikingly, by scaling down the channel length and integrating with our ALD-grown high-k dielectrics, we achieved record high drive current of over 1 A/mm at relatively low $V_d s$=1.4 V. Figure 3.3c and 3.3d represent I-V curves of a short channel device with channel length of 300 nm fabricated on an 11-nm-thick Te flake. Similarly, Figure 3.3a and 3.3b represent I-V curves of a typical long channel device with channel length of 3 m for comparison. The on/off ratio of the short channel device at small drain bias ($V_d s$=-0.05 V) is over 10^3, which is still a decent value, considering its narrow bandgap of 0.4 eV. The off-state performance is slightly deteriorated at large drain voltage ($V_d s$=-1 V, pink circles in Figure 3.3d) due to the short channel effect. Large drain voltage reduces the barrier height for electron branch and electron

current is unhindered, which is also reflected in the upswing of drain current at large $V_d s$ in output curve (Figure 3.3c). Such effect is common in narrow-bandgap short channel devices and can be mediated through proper contact engineering. Figure 3.4b shows the relationship between two transistor key parameters, on/off ratio and maximum drain current, of over 30 devices with different channel thickness. Generally speaking, a short channel device with flake thickness around 7-8 nm offers the best performance with on/off ratio 10^4 and maximum drain current over 600 mA/mm. It is also worth mentioning that the maximum drain current we achieved is 1.06 A/mm, with several devices exceeding 1 A/mm, which is so far the highest value among all the two dimensional material transistors to our best knowledge. This number is also comparable to that of conventional semiconductor devices.
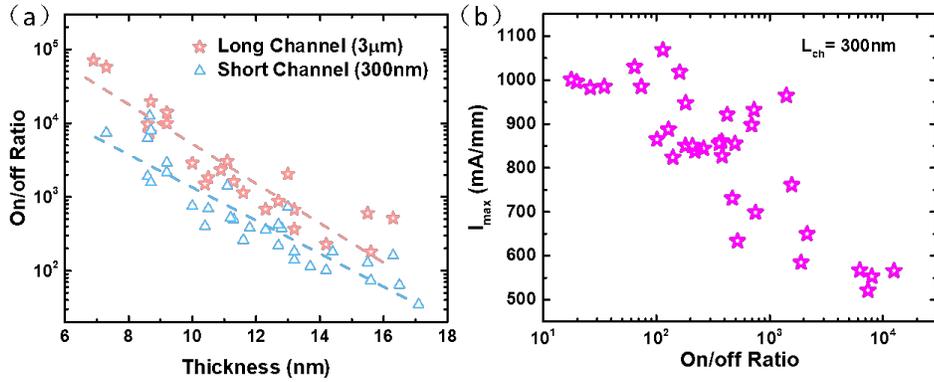
Fig. 3.4. Designing rules for on/off ratio and drive current trade off. (a) Thickness dependence of on/off ratio for both long channel devices and short channel devices. (b) Trade-off between on/off ratio and maximum drain current measured in over 30 device with same geometry and dimension as in Figure 3.3c.

3.4 Contact Engineering for PMOS

In order to optimize the device performance, high quality metal-to-semiconductor contacts is very crucial. In general it is difficult to make direct contact from metal

to semiconductor due to the existence of Schottky barrier. And the Schottky barrier height can barely be tuned by simply changing different types of metal with direct work functions, which is referred to as Fermi level pinning effect. It is widely acknowledged that the Fermi level pinning effect is less severe in 2D vdW semiconductors than in traditional bulk 3D semiconductors thanks to their dangling bond-free crystal facet. It is reported that the pinning factor in 2D material can reach near unity using transferred contact technique [75]. The first strategy is to use high work function metal, for instance palladium (work function 5.2 eV), to accommodate its p-type hole transport by reducing Schottky barrier height. The contact resistance is extracted from transmission line method (TLM). Multiple transistors with different channel length ranging from 200 nm to 3 μm were fabricated and total resistance were measured at small drain voltage -50 mV under different gate bias. Different types of metal were deposited on the same flake to rule out the flake to flake variation. We found that the high work function metal Pd has the best contact performance compared to other types of metal contacts, as shown in Figure 3.5. More importantly, we found that the Pd-Te interface actually formed accumulation-type contacts without Schottky barrier which is very rare, especially in p-type semiconductors. We will continue the discussion of accumulation contact in next chapter where we used photocurrent mapping to visualize the band bending.

We here also propose a surface treatment process to further reduce the contact resistance. Oxygen/argon plasma etching was used to clean the flake surface by removing the PVP residue and the native oxide layer on tellurium after source and drain windows are opened. The controlled trials were performed onto the same flake to rule out flake-to-flake variation and thickness influence. By linear extrapolating total resistance versus channel length curve (Figure 3.6), we find that the on-state contact resistance has been effectively reduced by 20% after plasma cleaning. The contact resistance at on-state (V_g= -100V) can be as low as 0.46 Ω·mm with plasma etching and using high work function Pd contact, which is among the lowest contact resistance we can achieve in all 2D material transistors.
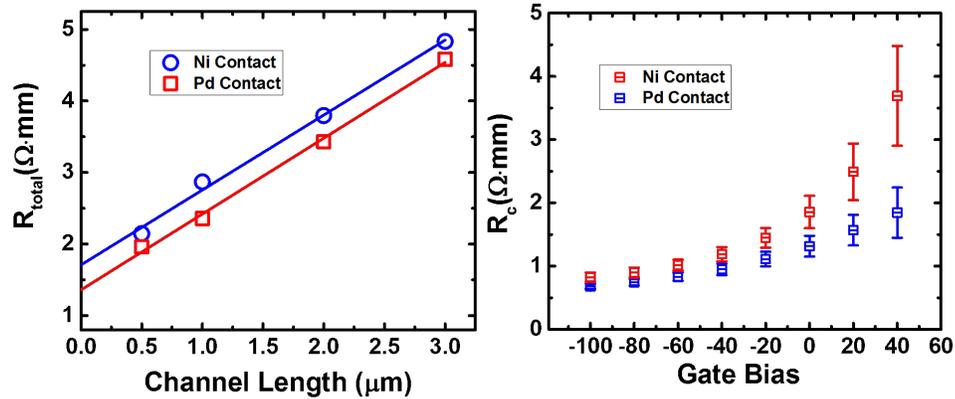
Fig. 3.5. Contact resistance with different metals. (a) Extracting contact resistance of different metal types with transmission line method (TLM). High work function metal Pd forms better contacts. (b) Contact resistance under different gate bias.
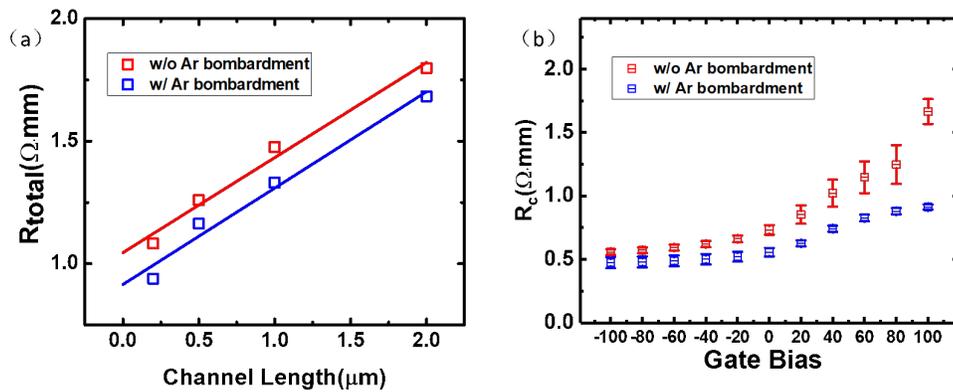
Fig. 3.6. Contact resistance improvement with argon bombardment treatment. (a) Transfer length method to calculate contact resistance w/ and w/o plasma cleaning. (b) Contact resistance measured at different gate bias. With argon bombardment treatment, the contact resistance was reduced to 0.46 mm which is the lowest among all 2D materials.

3.5   Self-aligned Top Gate Devices

In this part we will present a simple and novel method to fabricate self-aligned top gate device on tellurene. Unlike previous similar process of self-aligned top-gate

device on MoS_2 which requires self-oxidation of aluminum and an additional step of deposition [76], we found that by simply depositing aluminum onto tellurene once and without further process, a thin insulating layer of aluminum oxide is already formed automatically in between and therefore a metal-oxide-semiconductor (MOS) structure is instantly obtained. Since aluminum electrode is deposited in a high vacuum physical vapor deposition (PVD) chamber with pressure lower than 10^{-7} Torr, we can rule out the possibility of aluminum being oxidized during deposition. Although the mechanism is not fully understood, the discovery does provide us a one-step process to simultaneously form top gate metal and oxide MOS stack to simplify the overall fabrication process. The simplified self-aligned gate process (although not the same concept as in conventional CMOS process) also has great scaling potential in the sense that the lithography steps are reduced and the overlay accuracy can be increased.

To microscopically investigate the MOS stack structure, a cross-sectional transmission electron microscopy (TEM) image was taken at the gate area. As shown in Figure 3.6a, a 5 nm thick amorphous layer was formed between Te and Al layers. Energy dispersive X-ray spectrometry (EDS) elemental mapping results (shown in Figure 3.6b-d) reveal the presence of oxygen atoms in the amorphous layer. EDS line scan (Figure 3.6e and 3.6f) shows that oxygen atoms only exist at the interface of Te and Al, and its peak is overlapped with Al line, confirming the formation of aluminum oxide layer. We also found that the oxide layer thickness is also independent on flake thickness.

We then fabricated dual-gate tellurene transistors based on self-aligned top gate process. Figure 3.14a shows the schematics of a dual-gate device. The back is heavily doped silicon substrate capped with 300 nm SiO_2, and the top gate is 300 nm wide self-aligned aluminum electrode, with gate to S/D spacing 100 nm. The transfer curves of both top gate and back gate are plotted in the same figure for comparison. As shown in Figure 3.7b, both gates can modulate the device with similar on/off ratio, but by sweeping back gate we can drive three times higher drain current, and
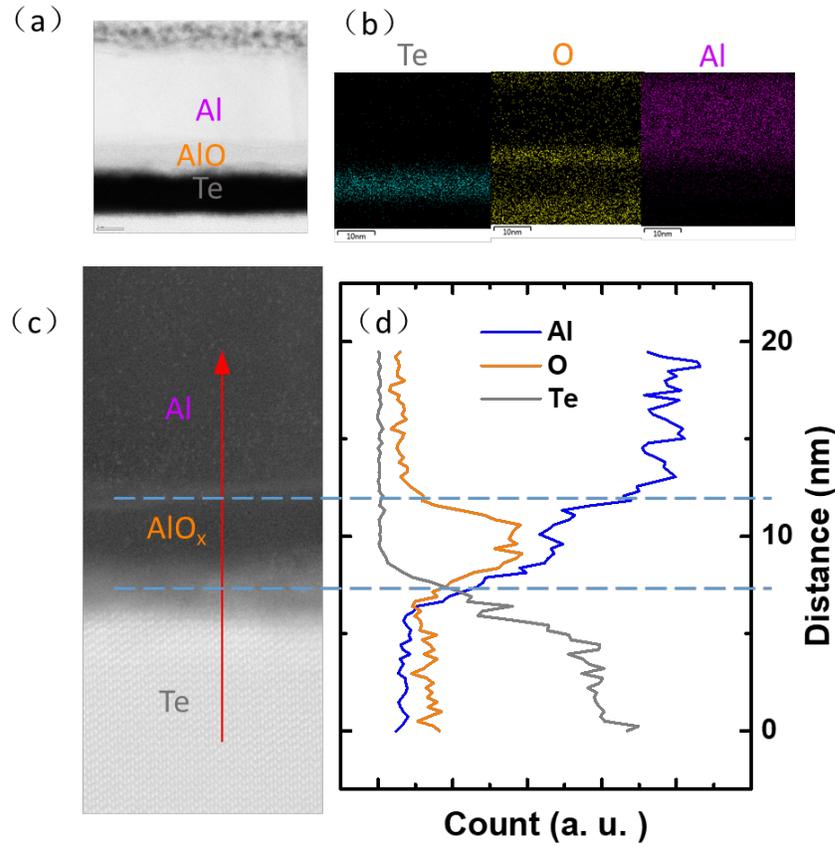
Fig. 3.7. Cross-sectional TEM and XDS analysis of self-aligned top gate device. (a) High resolution annular bright field (ABF) cross-section image of self-aligned top gate. (b) EDS mapping of tellurium, oxygen and aluminum atoms distribution; (c) high resolution TEM image of the gate area cross section; (d) EDS line scan of Te, O and Al atoms.

strong ambipolar behavior is also observed. This is because back gate can universally modulate the device including the contact regions by changing the carrier density under source/drain contact and therefore the contact resistance is reduced at on-state (negative bias). Whereas the top gate can only control the region under the gate which means the spacing between gate and S/D as well as the contacts are equivalent to two large resistance in series with the channel. These two spacing regions are also

responsible for suppressing the ambipolar behavior since there are almost no electrons without the gate tuning.
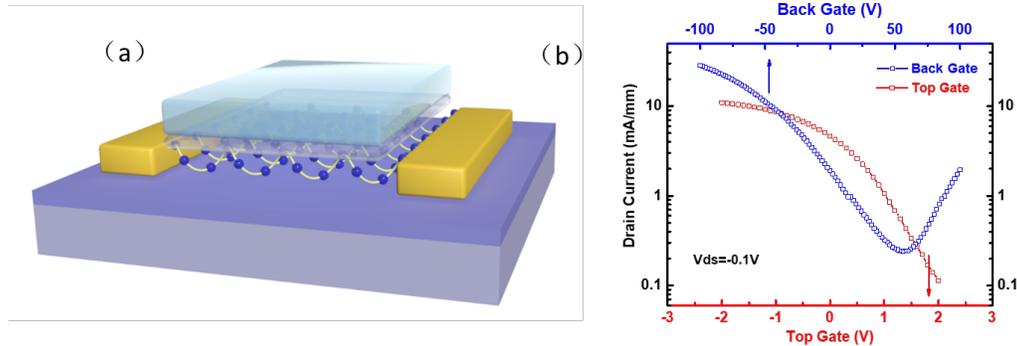
Fig. 3.8. Self-aligned dual gate tellurene transistors. (a) Schematic image of a self-aligned dual gate device. In the real device gate length is 300 nm and the spacing between top gate and source/drain contact is 100nm. The substrate is heavily doped Si wafer with 300 nm SiO_2 capping layer which can be used as back gate and dielectric. (b) Transfer curves of the dual gate device. Red curve is obtained by sweeping the top gate from -2V to 2V and the blue curve is obtained by sweeping back gate from -100V to 100 V. The drain voltage is biased at -100 mV for both curves.

We can also use this dual gate structure to engineer the device performance and change the carrier density or even carrier polarity. Figure 3.8a shows that when top gate is utilized to electrostatically dope the channel, the transfer curve of back gate is shifted significantly and ambipolar characteristic is also enhanced at positive top gate bias because of increased electron density from top gate doping. Threshold voltage (V_{th}) was extracted by extrapolating the linear region of the transfer curve and almost a linear V_{th} shift was observed for both n-type and p-type because of the different doping level from the top gate (see Figure 3.8b). Likewise, we can also tune the top gate device performance by stepping the back gate as shown in Figure 3.8c. In this case we can flip the polarity of the transistor from p-type (with negative back gate bias) to n-type (with positive back gate bias). The combined dual-gate modulation of drain current was plotted in color map as illustrated in Figure 3.8d. The upper
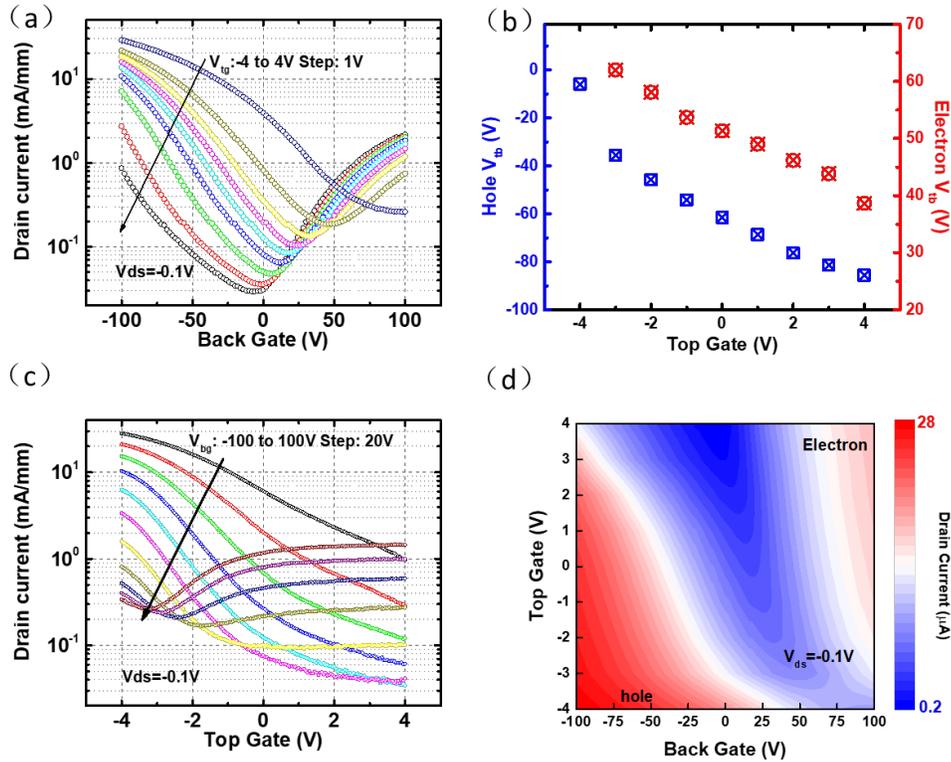
Fig. 3.9. Dual gate tellurene device with different operation modes. (a) Back gate transfer curves sweeping from -100 to 100 V with top gate with the top gate stepping from -4 V to 4 V. (b) Back gate threshold voltage shift depending on the top gate doping level. (c) Top gate transfer curves sweeping from -4 V to 4 V with the back gate stepping from -100 to 100 V. The device underwent a transition from p-type to n-type due to the electrostatic doping. (c) Color mapping of drain current (log scale) with different top gate and back gate. The drain current is measured at -100 mV drain voltage. The upper right corner is corresponding to positive bias for both top and back gate where the device is operated at n-type region whereas the lower left corner is p-type region with both gates negatively biased.

right corner represents the scenario of both back gate and top gate being positively biased and electron current is maximized whereas the lower left corner stands for the hole dominated case with both negative bias for dual-gates.

3.6 Te Nanowire Transistors

Finally in this section we will briefly cover the efforts of fabricating Te nanowire (NW) transistors. As a byproduct of tellurene liquid-phase growth, a certain amount of Te nanowires can be also obtained simultaneously. We also measured the electrical performance of these filaments as well. Te NWs were synthesized and transferred onto SiO_2/Si substrate with the same technique as tellurene. Ni/Au contacts were deposited and Figure 3.9 shows a typical Te-NW transistor electrical performance with 1 m channel length and 14 nm diameter. The on/off ratio reaches near 10^5 and the maximum current approaches 10 μA. If we treat the device as a planar transistor and normalize the current with the diameter, we can obtain a drive current over 0.71 A/mm. The hysteresis and noise are quite large for Te NW devices though, probably due to the large surface-to-volume ratio where interface traps plays a larger role in the device performance. This problem can be mediated with proper surface passivation.
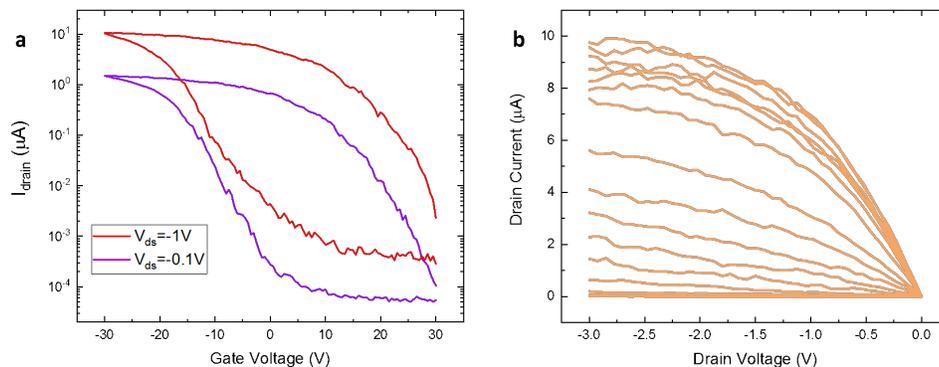
Fig. 3.10. Electrical performance of Te-NW transistors. (a) Transfer curves and (b) output curves of a typical Te-NW transistor with 1 μm channel length and 14 nm nanowire diameter.

We also extracted field-effect mobility from the slope of transfer curve linear region (at V_ds=-0.1V) as shown in Figure 3.10. The transconductance shows a peak as a typical transistors and the peak field-effect mobility reads about 2,000 and 900

cm^2/Vs for forward and backward sweep direction. The charging and discharging of interface traps can cause overestimation/underestimation of field-effect mobility in forward/reverse sweep directions, and we can anticipate a real field effect mobility somewhere in between these two values. It is quite surprising that the NW device actually has slightly higher mobility than 2D films, and one possible explanation is that Te-NW is volume-inversion type device where the carriers are pushed to the center of the NW and reduce the surface scattering. Similar effects has been observed in III-V nanowires as well [77].
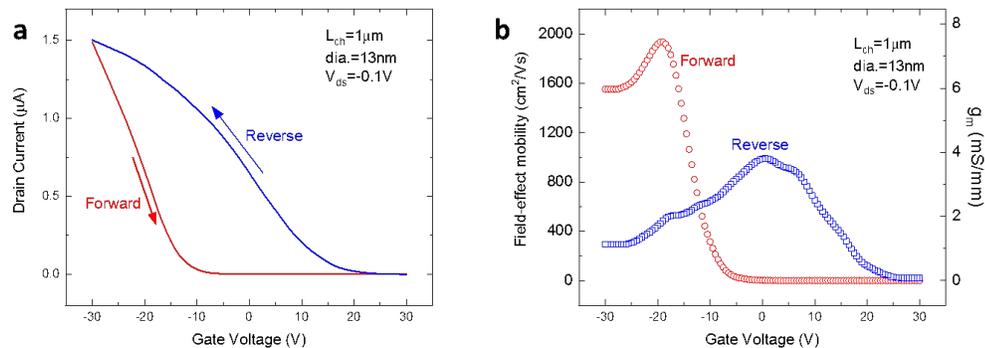
Fig. 3.11. Extraction of Field-effect mobility of Te-NW transistors. (a) Transfer curves plotted in a linear scale. (b) Transconductance and field-effect mobility measured in forward and reverse sweep directions.

Finally we systematically studied the transistor performance as a function of NW diameters (see Figure 3.11). We investigated over 30 NWs with diameters ranging from 5 nm up to 40 nm. The transistors with NW diameter below 5 nm are not measureable due to the degradation of overwhelming defects. For NWs thicker than 5 nm, the on-current increase monotonically with the diameter. Similar to 2D trasistors, the thinner NWs also has larger on/off ratio due to better gate electrostatic control. We normalized the on-current with the crosssection area of NW and found an average saturation ampacity of 2.6 MA/cm^2.

3.7 Summary

Since the emergence of MoS_2, 2D materials, especially semiconductors, has been considered the saver for Moores Law as a successor of silicon. However, after over a decade of intensive study, the 2D material based transistors still seems to be the star of university labs and far away for commercialization. Many technical challenges need to be addressed for different 2D materials. We introduce 2D Te, a new 2D material system to the community, as a promising candidate for building transistors and circuits.

Tellurene has a lot of unique properties that gives it an edge over other layered materials for electronics application. For example, it has the highest hole mobility among all p-type 2D materials, and Ohmic contacts are relatively easy to realize. It also shows great air-stability, and the lateral size of liquid grown tellurene films are also much larger than other exfoliated 2D materials. Due to the unintentional doping, Te and tellurene naturally exhibit p-type transport behavior, thus in this
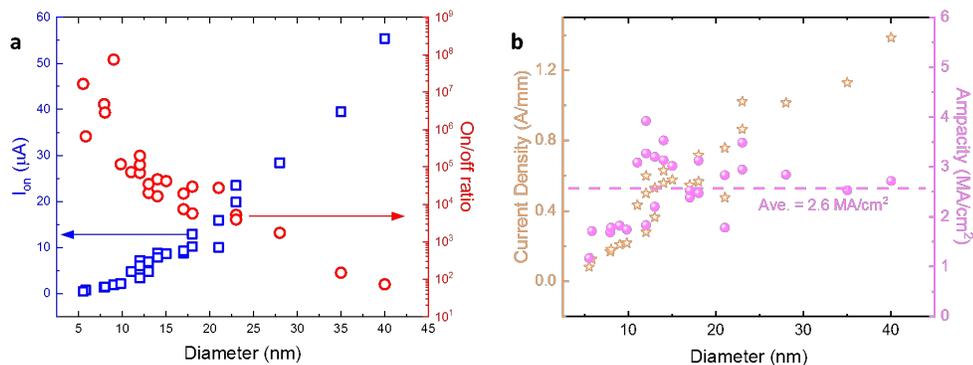
Fig. 3.12. Statistic study of Te-NW transistor performance as a function of diameters. (a) The on-state current and on/off ratio extracted from NWs ranging from 5 nm to 40 nm. (b) The saturation current normalized with diameter (left axis) and area (right axis). The average saturation ampacity is 2.6 MA/cm^2.

chapter we only focused on demonstrating the extraordinary electrical performance of p-type transistors. Our major achievements are:

Tellurene transistors were systematically investigated with different channel length and thickness;

High hole mobility (700 cm^2/Vs), large on-state current (over 1 A/mm), and large on/off ratio (10^6) were achieved;

Device performance were further improved through scaling and contact engineering;

The top gate devices were also fabricated with outstanding performance among all 2D material top-gated device;

A self-aligned top gate fabrication technique with great scaling potential.

Nonetheless, this is still the primitive exploration of tellurene electronics and just like other materials, further efforts need to be made to realize the full potential of this material system. For example, we are still struggling with the transistor performance of films thinner than 3 nm. And to implement CMOS logic circuits, an effective doping scheme is needed in order to achieve NMOS device, which will be discussed in the next chapter.

4. TOWARDS TELLURENE-BASED CMOS AND BEYOND

The modern digital logic circuits relies heavily on the advance of Si CMOS technology, which has the advantage of high fidelity, high reliability and low standby power. However, to construct CMOS circuits with both NMOS and PMOS devices with almost symmetric operation, a controllable doping technique is essential. For silicon, sophisticated doping technique, mainly implantation and diffusion, has been well-developed in the last several decades. However, for the rising 2D materials, the doping method is always an obstacle to preventing 2D transistors from being commercialized. Most materials, like MoS_2 and black phosphorus, shows superb electrical performance in one species of carriers yet can hardly be tuned into the other polarity due to the intrinsic doping. Some other materials like $ReSe_2$ has a Fermi level close to the middle of the band gap and thus both p-type and n-type branches suffer from large Schottky contacts. Here in this chapter, we will introduce a very effective doping method to achieve n-type Te transistors. Te NMOS shows almost symmetric performance as PMOS and prototypical CMOS devices were demonstrated. Also in this chapter, we will extend the functionality tellurene a little bit further and discuss its applications beyond CMOS.

4.1 N-type Transistors Enabled by ALD Doping

In the previous session, we have demonstrated that Te is capable of making p-type transistors. However, like most of other 2D materials, the lack of doping techniques [78, 79] to obtain its counterpart n-FETs is a major roadblock against the realization of Te CMOS or steep-slope devices such as tunneling FETs. In this session, for the first time, we demonstrated Te n-FETs enabled by atomic layer deposited (ALD)

dielectric doping technique with large drive current (200 mA/mm) and reasonable on/off ratio ($\sim 10^3$). The n-FETs show almost symmetric operation as p-FETs and comparable field-effect mobility of 612 cm^2/Vs. Using low work function metal, the on-state contact resistance is reduced to 4.3 $k\Omega \cdot \mu m$. The impacts of oxide layer type and thickness on doping effect are also systematically studied.

We first fabricated Te back gated transistors with the same method as in session 4.1. We found that an ALD-grown thin oxide capping layer on Te transistors can effectively dope the channel to n-type and change the device polarity into n-type. In the right panels of Figure 4.1a and 4.1b, the transfer and output curves of a typical Te n-FET device with 10 nm HfO$_2$ capping layer are presented. The device shows n-type dominated transport behavior, with slightly ambipolar tail due to its narrow bandgap nature. The on-state current of the n-FET reaches 200 mA/mm with a decent on/off ratio over 10^3. The intrinsic field-effect mobility in n-FETs (612 cm^2/Vs) is comparable to that in p-FETs (817 cm^2/Vs). More importantly, the operations of p-FET and n-FET devices are almost symmetric, indicating great potential for future CMOS applications. Here we shall mention that we chose low work function metal Ti for n-FET contact metal. However, at small Vds region, the n-FET still exhibits slight non-linear behavior, an indication of Schottky-type contacts. With transmission line model (TLM) method, we can extract a reasonable contact resistance value of 4.3 $k\Omega \cdot \mu m$, but still much higher than that in p-FET (0.46 $k\Omega \cdot \mu m$).

The mechanism of ALD doping effect is so far still elusive. One plausible explanation is the fixed charges from the remnant carbon atoms in ALD metal-organic precursors. Similar doping effect has also been observed in ALD dielectric on black phosphorus [80]. We systematically investigated the impact of different types of ALD oxides and oxide layer thicknesses on doping effect. The voltage at which the current minima occur in transfer curves is used as a gauge of doping levels, corresponding to the scenario where the Fermi level is at charge neutral level of the bandgap. We found that the doping effect becomes stronger as we increase the oxide thickness as

we expected (shown in Figure 4.2a). ZrO_2 and Al_2O_3 show slightly stronger n-type doping effect than HfO_2 as demonstrated in Figure 4.2b.

Here with the proposed ALD doping technique, we also demonstrated a simple Te based CMOS inverter devices. Top gate PMOS transistor was first fabricated with Ni contacts and capped with 20 nm SiO_2. An NMOS device was subsequently fabricated
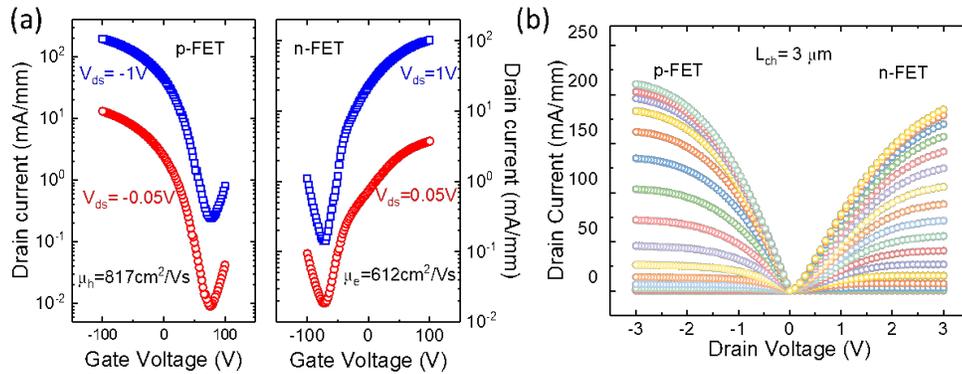
Fig. 4.1. Electrical characteristics of Te n-FETs and p-FETs. (a) Transfer and (b) output curves of Te n-FET and p-FET show almost symmetric operations. (c) Contact resistance of Te n-FET extracted from transmission line model (TLM) method.
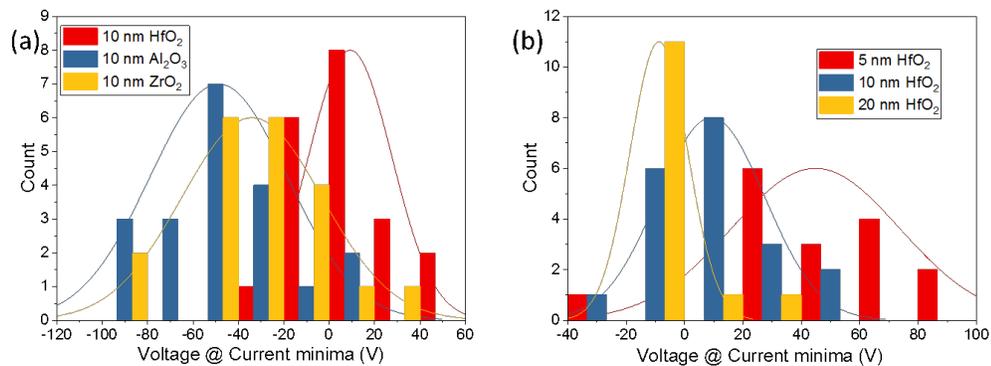
Fig. 4.2. Statistic study of doping effects as a function of oxide layer thickness and ALD oxide type. (a) The impact of ALD oxide thickness on doping effects. (b) The impact of different ALD oxide types on doping effects.

with ALD doping technique (20 nm HfO$_2$) and connected to the PMOS. Common top gate was used as input signal. Because the top gate metal of the PMOS device covers the entire channel region, it will effectively screen out the ALD doping effect, therefore the PMOS remains undoped after ALD growth. The inverter transfer curves are shown in Figure 4.3. This is a simple demonstration of feasibility to construct CMOS circuits with complex functionalities based on Te devices. More work will be carried out to further explore the potential of Te transistors.
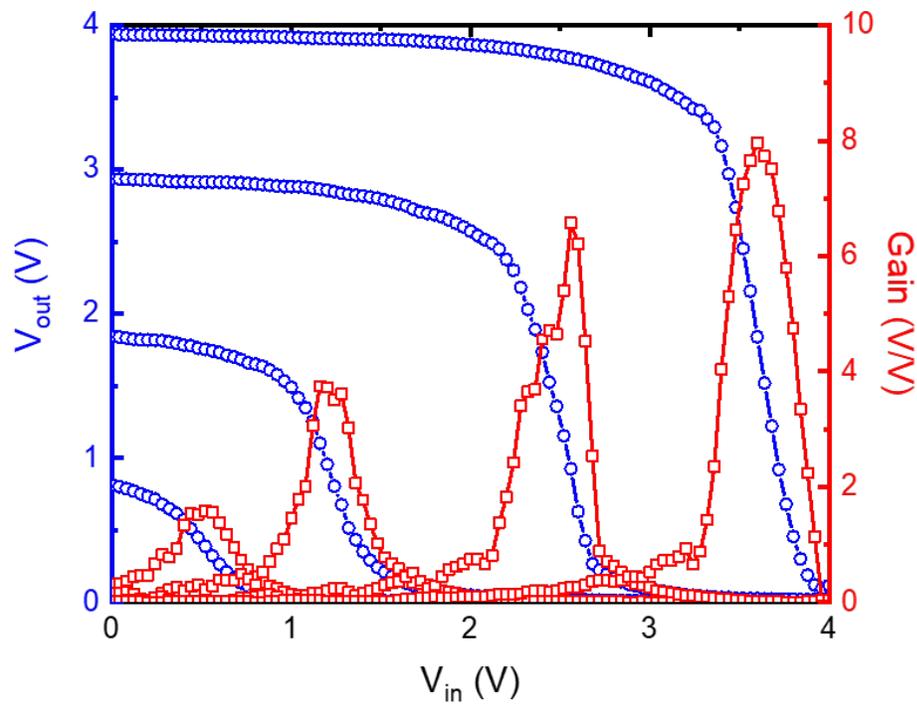
Fig. 4.3. Demonstration of 2D Te-based CMOS inverter device.

4.2 Enhanced Themoelectric Performance of Tellurium Approaching 2D Limit

Thermoelectricity emerges as one of the most promising solutions to the energy crisis we are facing in 21st century. It generates electricity by harvesting thermal energy which is a sustainable and environmental-friendly route compared to consuming fossil fuels. The efficiency of converting heat to electricity is evaluated by the key thermoelectrical figure of merit: $ZT = S^2 \frac{\sigma}{\kappa} T$, where S is the Seebeck coefficient defined as $S = \frac{\Delta V}{\Delta T}$, σ and κ are electrical and thermal conductivity and T is the operating temperature. However the ZT value has not been significantly enhanced since 1960s [81] and so far the most state-of-the-art materials can merely surpass 1 at room temperature [82,83]. This is because the parameters in defining ZT, Seebeck coefficient, electrical conductivity and thermal conductivity are usually correlated and by engineering one parameter, generally the other parameters will compensate the change, which poses a dilemma for drastically improve ZT.

For the past decades enormous efforts have been made to increase thermoelectric efficiency along two major pathways: either by adopting new high-efficiency thermoelectric materials or developing novel thermoelectrical nano-structures [84]. From material perspective, the paradigm of an excellent thermoelectric material should be a heavily doped narrow-bandgap semiconductor which shows good conductivity meanwhile because of the existence of the bandgap, the separation of electrons and holes can avoid the opposite signs of contribution in Seebeck coefficient. Also, heavy elements are preferred which provide more efficient phonon scattering centers and reduce the thermal conductivity. Furthermore, valley engineering is also proposed recently [85], where higher valley degeneracy can provide multiple carrier conducting channels without affecting the Seebeck coefficient and thermal conductivity.

Structural-wise, low-dimensional nanostructures are emerging thermoelectric research hot fields. The first advantage of low-dimensional nanostructure is the boundaries of the crystal will scatter the phonons more effectively than electrons due to

the different scattering length of these two species. The disruptive lattice period in low-dimensional nanostructures can block the acoustic phonon propagating whereas electrons can be transmitted normally. Therefore the thermal conductivity is the material system is reduced without degrading electrical conductivity. Moreover, when the characteristic length of the nanostructure geometry is small enough to modify the band structure because of quantum confinement effect, depending on the dimension of the nano-structures, the profile of density of states (DOS) will evolve into sharp shapes at band edges, which will significantly boost the Seebeck coefficient, since Seebeck coefficient is related with how fast DOS changes near the Fermi energy [84].

2D Te is an ideal material system for thermoelectric application which meets almost all the aforementioned criteria of a good thermoelectric material. Bulk Te has been theoretically predicted [40] and experimentally demonstrated [86] to be a good elemental thermoelectric material because it is an intrinsically p-type doped narrow band gap semiconductor with good electrical conductivity. On the other hand Te is the heaviest non-radioactive nonmetal element (excluding noble gases), therefore it has very low thermal conductivity due to the heavy atom mass and low acoustic phonon frequency, which also contributes to higher thermoelectrical efficiency. Recently, with more comprehensive band structure of Te being revealed, it has been revisited for new generation thermoelectric application recently due to its strong spin-orbit coupling which leads to a band splitting and quadruple band degeneracy near the edge of valence band [87].

In order to directly measure the Seebeck coefficient and conductivity, micro-thermoelectric measurement system was designed (optical image shown in Figure 4.4a), similar to the measurement setup for other low-dimensional materials such as graphene [88], MoS_2 [89] and SnS_2 [90]. Four-terminal micro-thermometers are placed at two ends of a Te flake to measure the local temperature. The filament of the thermometers was made of 100-nm-thick platinum (Pt) nano-strip because Pt shows good linearity of temperature versus resistance curve at the room temperature region. 10 nm Ti was deposited underneath Pt for better adhesion. A microheater

was fabricated near one side of the flake to generate temperature gradient. The microheater was intentionally made much longer (200 m) than the spacing and the flake size so that 1D thermal transport approximation is applicable. Two additional contacts were placed for measuring the resistivity of Te with four-terminal configuration. By applying certain voltage onto the microheater, the heating power was added to the system. The voltage drop was measured across the flake with a Keithley 2182A nanovoltmeter using pin x and pin x after sufficiently long time of waiting until the system reaches equilibrium. The resistance of the thermometer was also measured with four-terminal configuration with the Delta mode of synchronized Keithley 6221 current source and Keithley 2182A nanovoltmeter and was converted into local temperature using temperature vs. resistance curve. We observed monotonic increase of the voltage drop and the temperature increase as we increase the input power (Figure 4.4b), and the temperature rise at thermometer 1 is slightly higher compared to thermometer 2 since it is closer to the heat source. The voltage drop is plotted against the temperature gradient across the flake (see Figure 4.4c) with a linear trend from whose slope we can extract the Seebeck coefficient to be 413 μV/K. Furthermore, the conductivity of the same flake can also be measured with four-terminal configuration, and without the heating source, assuming that the temperature rise caused by the heater is negligible compared to room temperature and the conductivity is invariant with or without the heater. The measured Seebeck coefficient and conductivity gives a high value of Power factor 31.7 $\mu W/cm \cdot K^2$.

The thermal conductivity along the 1D chain direction of a 35-nm-thick Te film is measured using the micro-Raman spectroscopy technique35 on the suspended 2D Te film (Figure 4.5). The micro-Raman method uses the calibrated temperature-dependent Raman shift as a micro thermometer (Figure 4.5a). The laser focal line heats up the suspended tellurium film, measures temperature using the induced Raman scattering at the same time. Comparing to the numerical model (Figure 4.5b), the thermal conductivity is extracted to be about 1.50 W/m·K. This thermal conductivity value is lower than that of bulk Te around 3 W/m·K, which is reasonable

considering phonon scattering at the surfaces reduces thermal conductivity of thin films. Based on the measured thermal conductivity of Te films, we can derive a room temperature ZT value of 0.63, a significant boost from the ZT value reported in bulk Te (0.2~0.3).
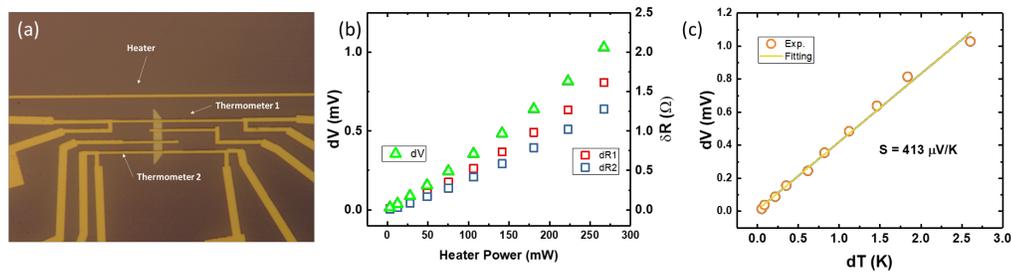
Fig. 4.4. Seebeck coefficient measurement of 2D Te. (a) Optical image of a device to measure Seebeck coefficient, electrical conductivity, and power factor. (b)The temperature rise and the thermoelectric induced voltage gradient measured under different microheater output power. (c) Extraction of Seebeck coefficient.
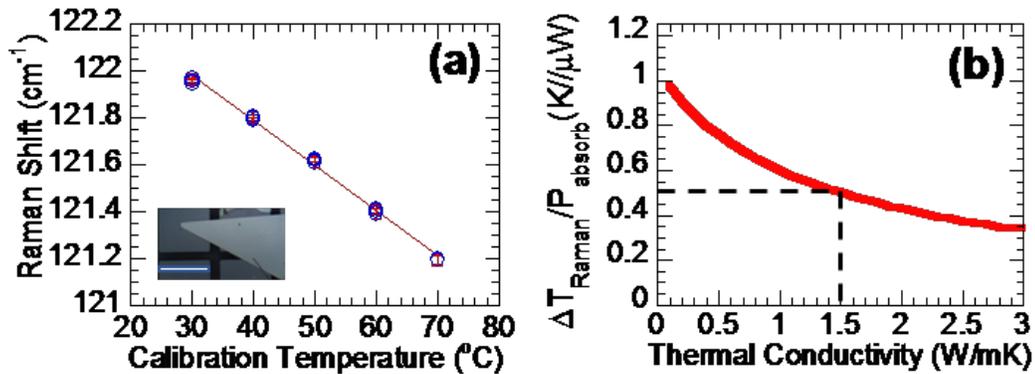
Fig. 4.5. Measurement of in-plane thermal conductivity using micro-Raman thermometry. (a) Calibrated Raman spectrum (A_1 mode) v.s. temperature as the micro-thermometry. Inset: optical image of the Te thin-film, scale bar 30 μm. (b) Numerical modeling result of temperature rise per absorbed laser power. Dashed lines indicate the in-plane thermal conductivity of 1.50 W/m·K, corresponding to the measurement temperature rise per absorbed laser power of 0.503 K/μW.

4.3   Photo-current Mapping and Accumulation-type Contacts

To exploit the advantage of thermoelectric effect in nanostructures, we not only need an excellent thermoelectric material to convert the thermal energy into electricity, but also well-engineered devices to efficiently collect the electricity, especially in nanoscale devices. One of the fundamental challenges of semiconductor device is the Schottky contact, which is usually formed on metal-semiconductor interface with large contact resistance and reduces the device efficiency and consume additional power. In the next section we will discuss how different kinds of metal contacts will affect the efficiency of harvesting thermoelectric power and use the laser induced thermoelectrical (LITE) current mapping technique to visualize the depletion-mode, neutral-mode and accumulation-mode contacts as well as the thermoelectric current distribution across the 2D Te devices.

A He-Ne laser with wavelength of 633 nm was used to locally heat the flake and create a temperature gradient. The short-circuit thermoelectric current was monitored by connecting a source meter to the two metal contacts and by moving the sample stage we can spatially map the photo-thermoelectric current as shown in Figure 4.6a and 4.6b. The laser beam size was focused to   1 μm through a confocal microscope. When the laser shines on the left side of the flake, the local temperature of the left will be higher than right. Therefore the carrier concentration of the left end will also be higher which creates the density gradient and diffusion current will flow from the left to the right, as seen in Figure 4.5b. Similarly when the laser spot moves to the right, the thermoelectric current will flip the sign. Also it is worth to mention that we achieved over 3 μA thermoelectric current under 3 mW laser power, which is at least orders higher (Normalized with laser power) than other reported 2D thin film devices such as SnS_2 [90] and MoS_2 [89] with similar photo-thermoelectric measurement. For fair comparison, we conducted the same experiment on black phosphorus which share many similar properties with Te including bandgap, room temperature

mobility, conductivity, and carrier polarity. It turns out the thermoelectric current of black phosphorus device is still two orders lower than that of Te.
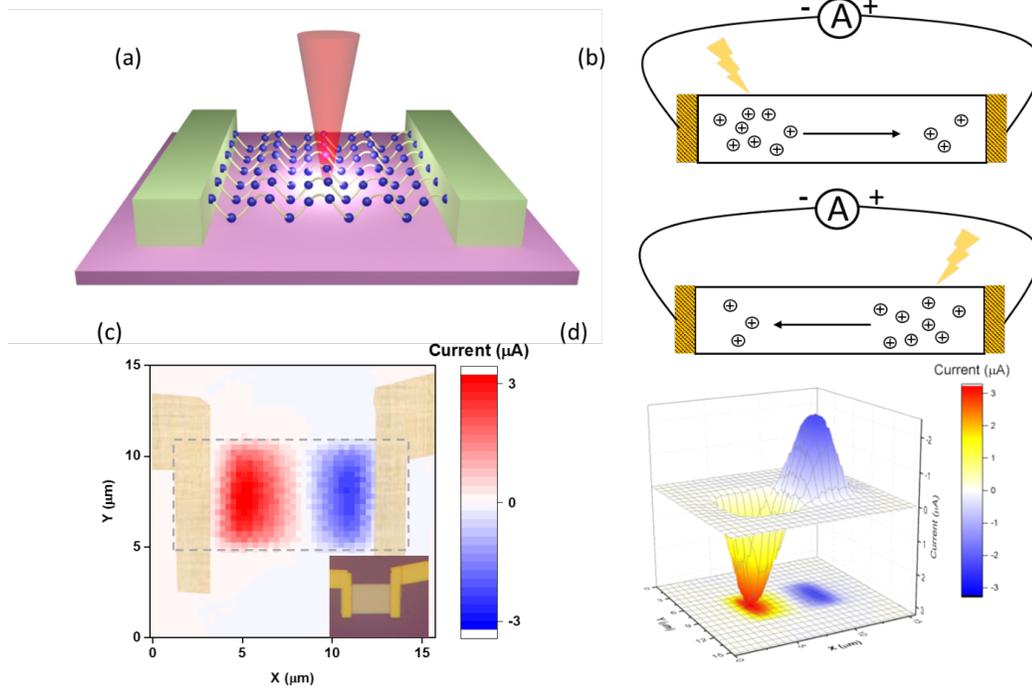

Fig. 4.6. Measurement of in-plane thermal conductivity using micro-Raman thermometry. (a) Calibrated Raman spectrum (A_1 mode) v.s. temperature as the micro-thermometry. Inset: optical image of the Te thin-film, scale bar 30 μm. (b) Numerical modeling result of temperature rise per absorbed laser power. Dashed lines indicate the in-plane thermal conductivity of 1.50 W/m·K, corresponding to the measurement temperature rise per absorbed laser power of 0.503 K/μW.

One major concerns of this photo-thermoelectric measurement is that besides the thermoelectric effect, there will also be photovoltaic effect mixing into the total current. The photovoltaic effect occurs when the laser spot moves to the metal-to-semiconductor interface where the misalignment of the metal work function and semiconductor Fermi level causes a build-in potential. This potential will induce a band bending where the photo-generated electron and hole pairs can be collected by

this electrical field. Noted that, in a symmetric device structure as in Figure 4.6c, the electrical field at two contacts will be in the opposite direction, and the photovoltaic current mapping profiles show some resemblance to the thermoelectrical current. One needs to carefully treat this issue and isolate these two components. One easy way is to spatially separate them as discussed by M. Lee et al. in SnS_2 [90] device. The band-bending region, characterized as depletion width which is determined by carrier concentration, is usually less than 100 nm. Hence the photovoltaic current should be confined within the narrow region of metal-semiconductor interface, whereas the thermoelectric current should be observed on the entire flake with a gradual change from positive to negative value. We can use this difference to spatially separate these two components.

Here we also changed metals with different work function to visualize the impact of contact metals on photovoltaic effect. There are in general three types of metal-semiconductor contacts: accumulation, neutral and depletion, depending on the alignment of metal work function and semiconductor Fermi level, as shown in Figure 4.7a, 4.7d and 4.7g. In principle by changing the metal work function we should be able to achieve all three types of contacts on the same semiconductor. However, the contact shape is difficult to alter experimentally in most of traditional 3D semiconductors such as Si, Ge and GaAs due to the Fermi Level pinning effect. For instance, in p-Si the contact is always pinned somewhere near 1/3 of the bandgap below conduction band to form a depletion contact no matter what metal contact is used. It is believed that the dangling bonds at semiconductor interface will introduce high density of mid-bandgap defect states that should be preferentially filled when the metal encounters the semiconductor. Therefore, it is difficult to form an accumulation contact (especially in p-type semiconductors) which is preferred contact type to form good Ohmic contacts. In 2D material scenario, the Fermi pinning effect will be eliminated or mitigated due to its bond-free surface. Here we adopted three different metals: Pd (work function = 5.4 eV), Ni (5.0 eV) and Cr (4.5 eV).

The results of photo-current mapping is shown in Figure 4.7. The Cr-contacted device shows four distinctive areas with different current origin (see Figure 4.7d): the middle red and blue area is thermally generated current and the outer zones are the photovoltaic current generated at the Schottky contacts. According to the polarity of the photovoltaic current, we can deduce that the band at the semiconductor boundary is bending downwards to form a depletion-type contact, which is the most common case.
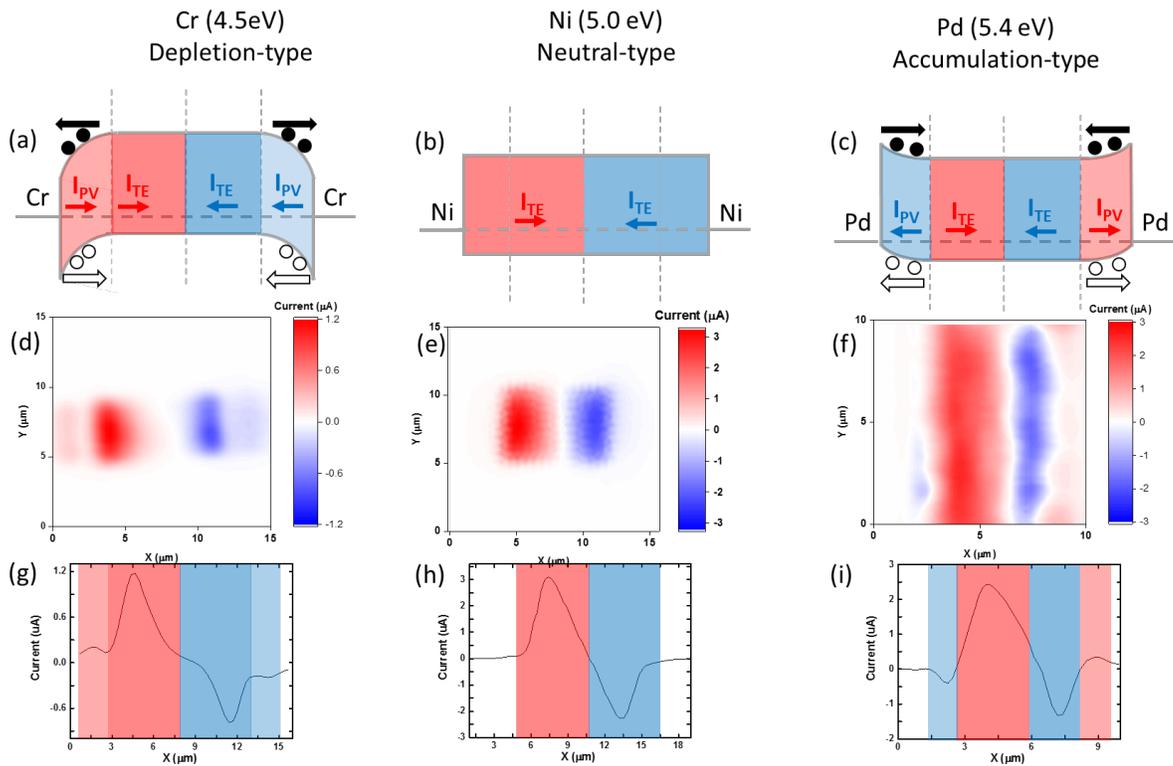
Fig. 4.7. Photo-thermoelectric measurement with different contact metals.(a)-(c) Band diagram and current flowing direction in Cr-, Ni- and Pd-contacted Te devices. (b)-(f) Photocurrent mapping of Cr-, Ni- and Pd-contacted Te devices.(g)-(i) Photocurrent distribution measured along a line cut parallel to the device orientation.

In contrast, the Ni-contacted device only have two distinctive thermoelectric current area (Figure 4.7b and 4.7e), indicating there is almost no band bending within

our instrument detecting range at the contact region (Figure 4.7h). This corresponds to the flat band situation which is represented in Figure 4.7b. As we adopting higher work function metal Pd, we noticed that the polarity of photovoltaic current has inverted compared to Cr-contacted device (Figure 4.7f and Figure 4.7i), indicating an accumulation-type contact is formed. This suggests Ni and Pd can form ideal metal-to-semiconductor contacts with essentially no Schottky barrier, which explains why we can achieve the record low contact resistance in 2D Te transistors with Pd contacts. The only contribution of the contact resistance comes from the thermionic emission which should be quite low considering the fact that the Fermi level of Te is very close to the valence band maxima. It is worth mentioning that such accumulation type contacts are very rare cases, especially in p-type semiconductors. The tunable contact band bending is owning to the de-pinning effect from vdW interface. We also noticed that the thermoelectric current is 3 times larger in Pd- and Ni- contacted devices compared to Cr-contacted device, indicating that high quality contacts are necessary to collect thermally generated carriers and harvest the thermoelectric energy more efficiently.

4.4   Summary

This chapter offers an important route of converting p-type tellurene films into its n-type counterparts, which outruns tellurene over many of its other 2D competitors that are struggling achieving CMOS devices due to lacking of doping scheme. Prototypical CMOS inverter was also demonstrated, which shows the feasibility of building CMOS logic circuits based on 2D tellurene.

Looking beyond electronics, we have also investigated the thermoelectric performance of Te when approaching 2D limit. Tellurium and telluride compounds have been long considered as good thermoelectric materials due to the heavy atoms of Te which induces strong phonon scattering. Due to the discrepancy between the electron and phonon mean free path, we managed to decouple the thermal conductivity and

electrical conductivity by reducing the film thickness and increase more phonon scattering without degrading electrical conductivity. A record high room temperature ZT value of 0.62 was achieved among all single element materials.

We showed in the chapter that the physical properties of tellurium can be tuned by confining the carriers into 2D limit. Meanwhile the ALD dielectric doping technique also grants us the access to the conduction band for the first time. In the next chapter, we will take advantage of these achievements and study the magneto-transport of both 2D electron gas and 2D hole gas in tellurene system.

5. QUANTUM TRANSPORT IN TELLURENE

Magneto-transport is a common method to manifest the electron behavior and reveal band information of the material system. Under low magnetic field, weak localization (WL)/antilocalization (WAL) effect can be observed as a peak/dip in the resistivity of the sample at zero field. This behavior is related to the wave function interference of electrons circling around a disorder in two opposite directions. In a normal metal the interference gives the destructive term which localizes the electrons near the disorder and this term can be broken with external magnetic field and experimentally it is manifested as a resistance peak at B=0. However in material systems with strong SOC, the interference term picks up a phase and reverses the sign. As a result, these materials shows a minima in resistivity at zero field. Through the study of WAL, we can extract the strength of SOC, and estimate the coherence length of the material system.

Under large magnetic field, the magneto-transport becomes much more interesting because of the Landau quantization. By solving the Schrodinger equation of 2DEGs under magnetic field, the eigen energy becomes a set of evenly spaced discrete energy level which will cross the Landau level as we increase magnetic field. This effect, referred to as SdH oscillations, is a macroscopic manifestation of quantum transport and the prelude of quantum Hall effect. With sufficiently high sample quality, high magnetic field and low temperature, the 2DEG system enters quantum Hall region where Hall resistance is quantized into integer fraction of h/e^2 and the longitudinal resistance drops to zero due to the dissipationless edge states.

In this chapter we report the comprehensive magneto-transport measurements in both n-type and n-type tellurene films. For p-type samples, thanks to the stronger 2D quantum confinement imposed by physical limit of 2D films, we observed much better developed SdH oscillations and signs of quantum Hall states. WAL effect was

also studied along different axis to show the 1D structure related transport behavior. More surprisingly in n-type samples, we observed well-developed quantum Hall plateaus and SdH oscillations with eight-fold degeneracy. Topologically non-trivial Berry phase was detected in the quantum Hall sequence as an indication of Weyl fermions. A new species of topological states of matter – Weyl semiconductors with massive Weyl fermions were experimentally confirmed, with Weyl nodes arising from protected symmetry of chiral crystal instead of conventional band inversion.

5.1 Magneto-transport in p-type Tellurene

5.1.1 Shubnikov-de Haas Oscillations and Quantum Hall Effect

Two-dimensional electron gas (2DEGs) is an important subject in condensed-matter physics for being a host to many exotic and conceptual physical phenomena. Quantum Hall Effect (QHE), which refers to the effect of the transverse resistance being quantized into integer fractions of quantity h/e^2 in Hall measurement, is such a phenomenon that can only be observed in high-mobility 2DEGs. Traditionally, the confinement of electron motions within a two-dimensional plane is realized by quantum wells formed in inversion channel of silicon metal-oxide-semiconductor field-effect transistors (MOSFETs) [91] or AlGaAs/GaAs heterojunctions [92]. In the last decade, the emergence of 2D materials offers an alternative approach to achieving high mobility 2DEGs in atomically thin layers. 2D materials are formed by an assembly of atomic layers bonded by weak van der Waals forces. The crystal structure of 2D materials yields a dangling-bond-free surface and consequently the 2D material systems are less susceptible to mobility degradation with thickness shrinking down to a few nanometers than bulk materials. QHE has been observed only in a few high-mobility 2D material systems such as graphene [3, 4, 93], InSe [94] and encapsulated few-layer phosphorene [95–97] among thousands of predicted 2D materials [45]. Shubnikov-de-Haas (SdH) oscillations were observed in several other 2D materials

such as WSe$_2$ [98, 99], MoS$_2$ [100–102], ZrTe$_5$ [103], and Bi$_2$O$_2$Se [104]. Here for the first time, we report pronounced SdH oscillations and QHE in tellurene.

The broken spatial-inversion-symmetry of Te lattice structure gives rise to strong Rashba-like spin-orbit interaction [42], therefore a camelback-like electronic structure at the edge of the valence band [40] were predicted by the density functional theory (DFT) calculations. Weyl nodes were also theoretically predicted [24] and experimentally observed deeply embedded in the valence band of Te [27]. The earliest study on surface quantum states in bulk Te dates back to the early 1970s by von Klitzing, et al. [105–107], who later discovered QHE in silicon MOSFETs in 198097. However, to our best knowledge, the evidence of QHE in Te is so far still missing, and even the reported quantum oscillations were so weak that it could only be seen in the second derivative d^2R_{xx}/dB^2 [105, 106]. Since Te has superior mobility compared to silicon, it is intriguing why quantum phenomena are so weak in Te. We postulate that this is due to the weak quantization of Te surface states in the wide triangular potential well. The characteristic width of the surface potential well is proportional to $\sqrt{\epsilon_s}$ where ϵ_s is the permittivity of the semiconductor. The large permittivity of tellurium ($\sim$30) only induces a relatively small electrical field and wide potential well in tellurium surface. Therefore, the carriers are not tightly restrained near the surface to meet the rigid criteria of 2D confinement. In this work, we adopted a different strategy to impose stronger quantum confinement by employing 2D Te films. To study quantum transport, flakes with thickness around 8-10 nm are desired because (1) high crystal quality is still preserved with hole mobility nearly 3,000 cm^2/Vs at liquid Helium temperature; (2) the physical confinement in the out-of-plane direction is strong enough to impose sufficient 2D confinement. A Hall bar device image is shown in Figure 5.1a.

Figure 5.1b shows the typical longitudinal resistance (R$_{xx}$) and transverse resistance (R$_{xy}$) of a 10-nm-thick sample as a function of out-of-plane magnetic field measured at 300 mK with -85V gate bias. From the slope of Rxy in the small B-field regime, the sheet carrier density of $8.7 \times 10^{12} cm^{-2}$ (positive slope indicates hole
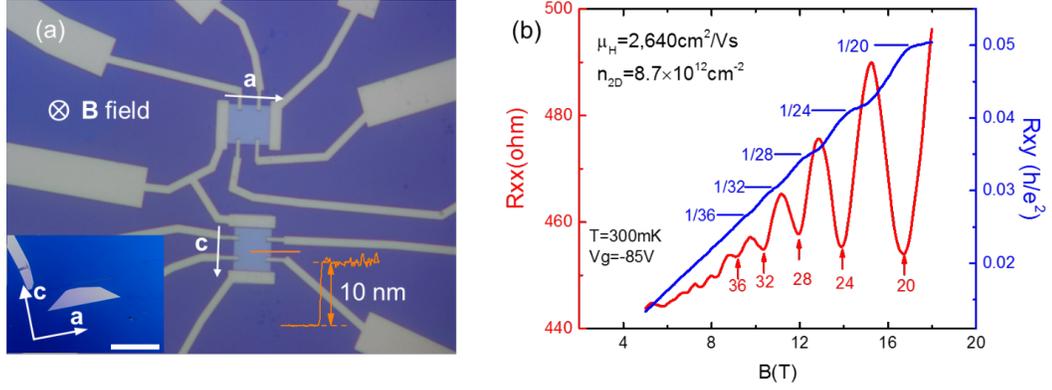
Fig. 5.1. SdH and QHE in p-type tellurene. (a) Optical image of Hall-bar devices along different crystal orientations that were fabricated from the same flake. Inset: as-grown flakes are usually in rectangular or trapezoidal shapes where the 1D direction is along the longer edge of the flake. The scale bar is 50 um. (b) QHE and SdH oscillations measured from a 10-nm-thick flake.

is dominant carrier type) was extracted from the equation $n_{2D} = 1/(eR_H)$, where R_H is the Hall coefficient, with corresponding Hall mobility of 2,640 cm^2/Vs derived from $\mu_{Hall} = \frac{L}{W} \frac{1}{R_{xx}n_{2D}e}$. Well-developed SdH oscillations were observed in longitudinal resistance, and the onset occurs at about 5 Tesla, from which we can estimate the quantum mobility to be 2,000 cm^2/Vs from the criteria of SdH oscillation onset: $\omega_c \tau > 1$ (cyclotron frequency $\omega_c = eB/m^*$, is the relaxation time and m^* is the hole effective mass in Te films), close to the mobility value obtained from Hall measurement. At large B-fields the transverse resistance shows a series of quantum Hall plateaus at the values of integer fraction of resistance quanta h/e^2, although the plateaus are not completely flat due to the broadening effect. The filling factors were calculated by normalizing Rxy with metrological standard value of h/e^2. With the capacity of our equipment of 18 Tesla magnetic field, the lowest filling factor ν we can observe is 20. An interval of 4 was found between the filling factors of neighboring plateaus, indicating a four-fold Landau level degeneracy. The four-fold degeneracy can be factored into two parts: (1) the spin degeneracy factor $g_s = 2$; and (2) valley

degeneracy factor $g_v = 2$ originating from H and H' point in Brillouin zone, similar to the case in graphene (K and K' points). Our tellurene samples show much better-resolved SdH oscillations than previously works on surface states of bulk Te, due to the high quality of 2D tellurene films and enhanced quantum confinement.

We then applied different gate bias to tune the carrier density and studied the gate-dependence of oscillation frequencies. The oscillation amplitudes were extracted by subtracting a smooth background from original data of R_{xx} and were plotted versus $1/B$ in Figure 5.2a. Strong oscillations with constant frequency $\Delta(1/B)$ are well-developed with a negative gate bias over -40 V. However, at lower (absolute value of) gate bias, no pronounced oscillations can be observed, because of the lower mobility at subthreshold regime where the carrier concentration is low. It indicates the impurity scattering is still dominant like most of the 2D materials and there is still large room to enhance transport properties through methods such as hexagonal boron nitride (h-BN) capping. Landau fan diagram was constructed by plotting the value of 1/B where the V_{th} minimum of R_{xx} occurs against its corresponding filling factor as a common practice. Landau index n is related to the filling factor ν through the equation: $\nu = g_s g_v(n)$, where g_s and g_v are spin and valley degeneracy of two respectively. All the data points fall onto a line that can be extrapolated towards zero intercept (fitting error within $\pm$ 0.2), indicating the standard phase of oscillations. The oscillation frequency B_F are derived from slope of the Landau fan diagram in Figure 5.2b, from which 2D carrier density n_s can be estimated by substituting the frequency into the equation of frequency-density relationship: $n_s = (g_s g_v e B_F)/h$. We also compared the oscillation carrier density (blue spheres) and Hall density (red pentagrams) in Figure 5.2c. The orange dash line is calculated from the gate capacitance model $n_{2D} = 1/eC_g(V_g - V_{th})$. The Hall densities, oscillation densities and densities calculated from capacitance model match quite well within a reasonable margin.

To better understand the two-dimensionality of Fermi surface in tellurene, we carried out angle-resolved SdH oscillation measurements in tilted magnetic fields. The
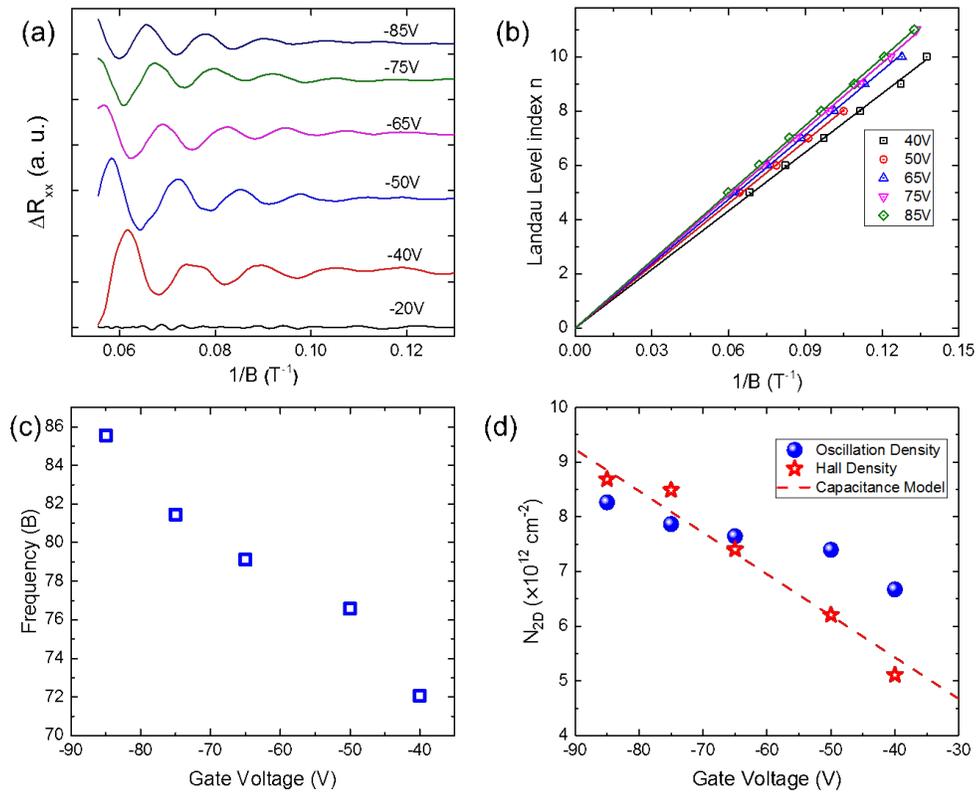
Fig. 5.2. Gate-dependence of Shubnikov-de-Haas oscillations versus 1/B. (a) The oscillation amplitude under different gate bias. Oscillations were revolved only when the negative gate bias is large enough. The amplitudes were extracted by subtracting a smooth back ground in R_{xx}. (b) Landau fan diagram under different gate bias. Each data points represent a minima in oscillation amplitudes. All the lines has interception near zero, indicating standard phase of oscillations. (c) Oscillation frequencies as a function of gate bias. The frequencies were extracted from the slope in (b). (d) Comparison of 2D carrier density measured from oscillation frequencies (pink sphere), Hall resistance (orange pentagrams) and calculated from capacitance model (dotted line).

experiment configuration is illustrated in Figure 5.3a. The sample was rotated along a-axis by angle α, and the corresponding 2D Fermi surface is associated with SdH oscillation frequency through the equation: $B_F(\alpha) = hS_F(\alpha)/4\pi^2 e$. The oscillation amplitudes with different angles were plotted in a color map in Figure 5.3b. A shift

of oscillation features towards higher magnetic field was captured as the tilted angle increases. For clarity, the angle-resolved SdH oscillation amplitudes were plotted against perpendicular magnetic field component $B_\perp = B \times cos(\alpha)$ in Figure 5.3c, where the minima of oscillations occur at the same value. The oscillations are too vague to be distinguished for $\alpha > 35°$, and in $0° < \alpha < 32°$ regime, the oscillation features also diminishes as we increase the angle (see Figure 5.3d, right axis). The physics origin of the fast damping of oscillation amplitudes in tilted magnetic fields is under further investigation. By performing fast Fourier transform, we found that the oscillation frequency $B_F(\alpha)$, or the projection of Fermi surface $S_F(\alpha)$, is linear dependent on the factor $1/cos(\alpha)$, another signature of two dimensionality of cyclotron motions.

5.1.2 Anomaly in SdH Oscillations and Band Evolution under Magnetic Field

Finally, we studied the temperature-dependence of SdH oscillations and the evidence of the band structure evolution with large magnetic field originated from the interplay of Zeeman splitting and spin-orbit coupling. Temperature-dependent SdH oscillation amplitudes were first investigated as a common practice to extract effective mass. As seen in Figure 5.4a, the period and the phase of the oscillations are independent of temperature, and the amplitudes exhibit a diminishing trend with rising temperature in general. For temperature higher than 5 K, the amplitudes decrease monotonically as we expected and can be fitted with the classical Lifshitz-Kosevich equation:

$$\Delta R_{xx} \propto (2\pi^2 m^* k_B T/\hbar e B)/sinh(2\pi^2 m^* k_B T/\hbar e B))$$

The fitted curves are plotted as solid lines in Figure 5.4c, and the effective mass m^* can be extracted to be $\sim 0.26 m_0$ (here m_0 is the free electron mass) correspondingly, which is very close to our DFT calculation. From the extracted effective mass and quantum mobility, we can estimate the Landau level broadening on the scale of $\Gamma =$
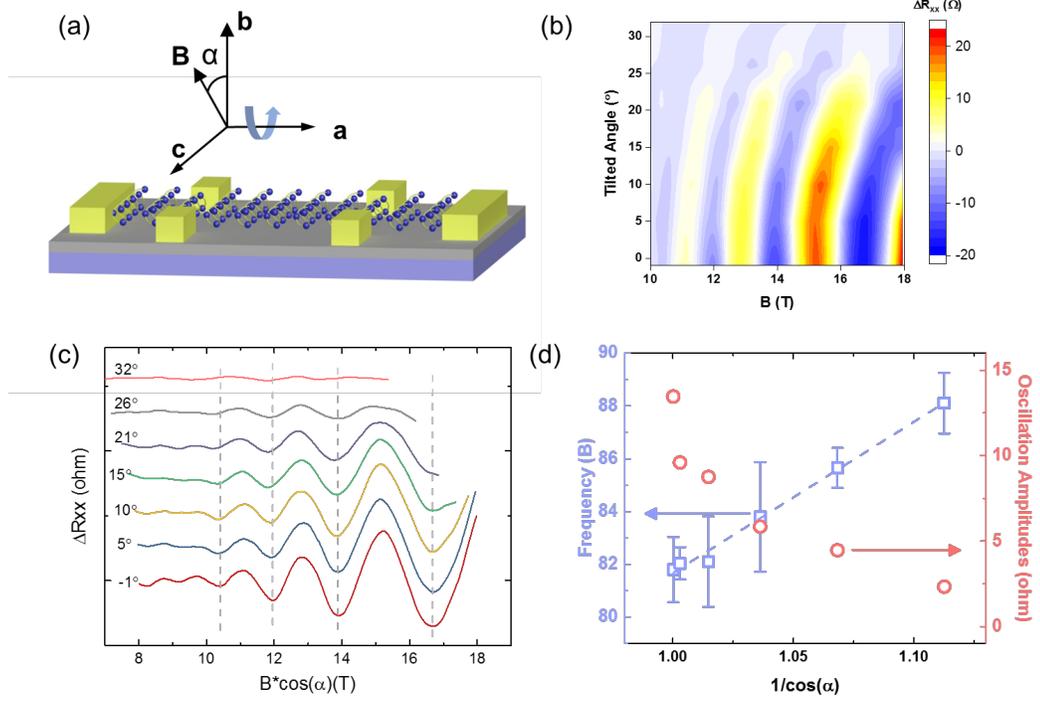
Fig. 5.3. Angle-dependence of oscillation frequencies. (a) Schematic configuration for angle-resolved oscillation frequency measurement. (b) Color map of oscillation amplitude as a function of B field and tilted angle. A shift towards higher magnetic field was observed at larger tilted angle. (c) Oscillation amplitudes plotted against perpendicular magnetic field component $B \times cos(\alpha)$. (d) Oscillation frequencies shows a linear relationship with $1/cos(\alpha)$, a signature of 2D Fermi surface.

$\hbar e/(\mu_q m^*) \approx 25K$ which is much more dominant than temperature broadening of 300 mK, indicating the limitation of experimental resolution comes from the disorders in the system. The carrier lifetime τ can also be extracted by combining the thermal factor as well as the Dingle factor $R_{xx} \propto R_T R_D$ where the Dingle factor R_D takes the form $R_D = exp(-\pi m^*/\tau eB)$. By reshaping the first equation and taking the semiology plot, we shall get: $ln(R_{xx} \cdot B \cdot sinh\lambda(T)) = -(\pi m^*)/\tau eB + const.$. Therefore, a linear trend is observed in $ln(R_{xx} \cdot B \cdot sinh\lambda(T))$ against $1/B$ plot where the carrier lifetime of 0.10 ps can be extracted from the slope.
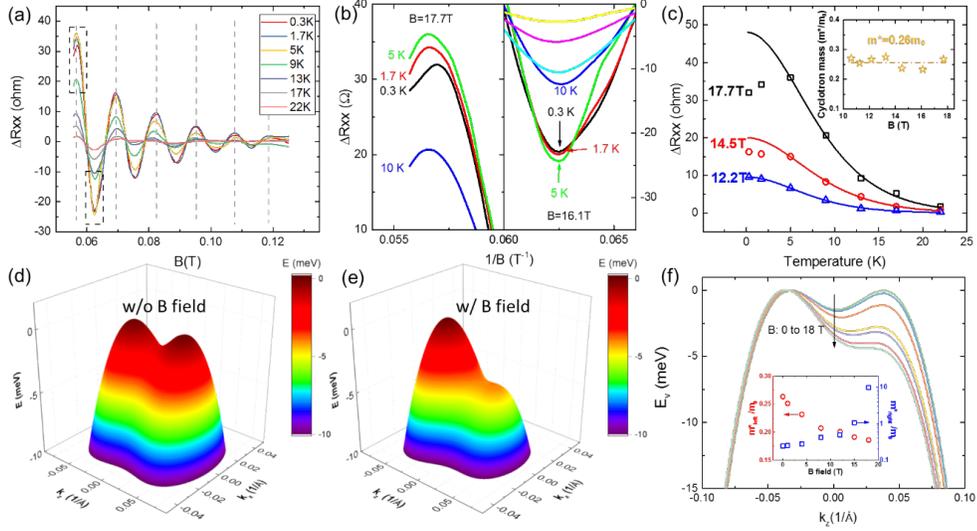
Fig. 5.4. (a) Temperature-dependence of oscillation amplitudes. The phase and frequency are invariant of temperature and the oscillation amplitudes in general show a decaying trend with increasing temperature following Lifshitz-Kosevich equation. (b) Zoomed-in features of two dash boxes in (a). (c) Extracted oscillation peak amplitudes under different magnetic field as a function of temperature. Under large magnetic field, the low-temperature data points deviated from fitting curves, which was also captured in (b). Inset: the effective cyclotron mass was extracted to be 0.26 m_0. (d) and (e): the camel-back shape of valence band maxima vicinity w/o and w external B field. The time-reversal-symmetry was broken by magnetic field. (f) A cross-section of valence band edge cut along k_z direction.

carefully examining the amplitude at each oscillation peak (zoomed in features are plotted in Figure 5.4b), we found that at temperature lower than 5 K the data points do not coincide with fitted curves, as shown in Figure 5.4b and 5.4c, and the discrepancy is more significant at larger B field. The deviation of oscillation amplitudes is abnormal, suggesting the average effective mass is heavier under the conditions of large magnetic fields and low temperatures. This can be tentatively explained by the band structure reshaping with the existence of external magnetic field. An insightful picture of the band structure evolution is given by DFT calculations under magnetic field perpendicular to the helical axis, with spin-orbit coupling taken into considera-

tion, as shown in Figure 5.4d-e. The broken spatial-inversion-symmetry of Te crystal introduces Rashba-like spin-orbit coupling (SOC), which causes a lateral shift of spin-up and spin-down subbands in different directions along kz axis in band dispersion diagram and forms a camelback structure as shown in Figure 5.4d. With the presence of external B field, the degenerate energy levels for spin-up and spin-down states will also be lifted by Zeeman splitting energy: $E_z = g\mu_B B$, where g is the g-factor and μ_B is the Bohr magneton. The interplay of SOC and Zeeman splitting introduces band evolution as shown in Figure 5.4e. If we take a cross-section of band dispersion along the camelback direction (k_z direction), we can clearly see that the two degenerate valleys will be split into one heavy hole pocket and one light hole pocket with increasing magnetic field (Figure 5.4f). Noted that the oscillation features were captured under large negative gate bias, which is equivalent to pulling the Fermi level slightly inside the valence band, as shown in the dashed line in Figure 5.4c. At sufficiently low temperature condition, the Boltzmann distribution ensures that the states responsible for transport will be confined within a very narrow range (several kT) near Fermi level, and the carriers in the right branch of Figure 5.4f will dominate the transport behavior, which exhibits larger effective mass. As the temperature rises, such effect will be mitigated by temperature broadening as the fine electrical structure becomes undetectable and the carriers in both pockets will participate in transport, hence the average effective mass will fall back to the classical value. The DFT calculation (see inset of Figure 5.4f) suggests that as we increase the external B-field to 18 T, the calculated effective mass of the light hole pocket slightly drops from 0.26 to 0.19 m_0, whereas the effective mass in the heavy hole pocket increases drastically to about 9.8 m_0 (see inset of Figure 5.4f), which qualitatively matches with our experiment results.

Another evidence related to this effect is the anomalous transfer characteristics of $R_x x$ versus gate bias under large magnetic field. For normal 2DEG systems, in the linear regime, the channel resistance should drop inversely as we raise overdrive voltage $|V_g - V_{th}|$. Here, Vth is the threshold voltage from which the channel is
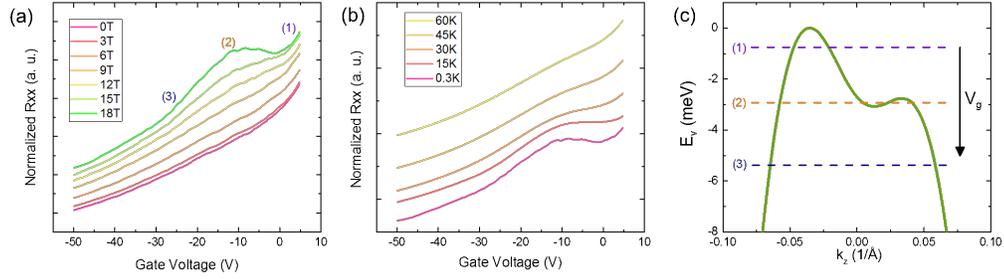
Fig. 5.5. Anomalous increase in R_{xx} when sweep gate voltage towards negative bias under different (a) magnetic field and (b) temperature. (c) Explanation of abnormally increasing resistance. As we sweep gate in reverse direction, the Fermi energy will be pulled downwards and slightly enters the valence band. (1), (2) and (3) represent three typical scenarios corresponding to the points in (a).

turned on. However, in tellurene films under large external magnetic fields and at low temperatures, as we sweep the gate voltage in reverse direction, the resistance sees an abnormal rise around -5 V which peaks at round -10 V, and drops again at around -20 V as shown in the top curve in Figure 5.5a. We further verified that this anomalous increase in resistance has a strong dependence on the magnetic field (see Figure 5.5a). Therefore we believe it is also related to the aforementioned Zeeman effect induced band structure evolution. We denote three representative situations (1), (2) and (3) as we lower the Fermi level in Figure 5.5c, corresponding to spots (1), (2) and (3) in the transfer curves in Figure 5a. At positions (1) and (3), the transport behavior can be explained with classical semiconductor picture. At position (2) however, the carriers in the heavy pocket start to dominate the transport and the resistance will increase because of larger average effective mass. This anomalous resistance bump will also vanish at higher temperature (shown in Figure 5.5b) as the temperature broadens the Boltzmann distribution, making it difficult to distinguish such fine structures in the electronic band. In general, the camel-like electronic structure remains same in 2D tellurene flakes with the thickness of 8-12 nm, similar to trigonal Te bulks.

5.1.3   Weak Anti-localization Effect in B$_z$ Direction

Several literatures have previously studied the anisotropic electrical behaviors of bulk Te, showing that resistivities of intrinsic Te at room temperature are $\rho_\parallel = 0.26\Omega \cdot cm$ and $\rho_\perp = 0.51\Omega \cdot cm$, parallel and perpendicular to the c-axis, respectively [108]. However, the anisotropic magneto-transport properties of synthesized 1D van der Waals Te thin film have never been reported. The anisotropic magneto-transport properties with their temperature dependence are presented below. In the first experiment, the applied magnetic field is in z-direction and perpendicular to the x-y thin film plane. In this experiment, the magnetic field is in y-direction along the a-axis of Te thin film. In the third experiment, the magnetic field is aligned to 1D Te atomic chains, c-axis, which is defined as the x-direction (Figure 5.6b). We first present the magneto-transport results of Te in B_z direction, in which the magnetic field is applied perpendicularly to the 2D thin film plane. Magneto-resistance (R_{xx}) measurements of a typical Te thin film at different temperatures from 0.4 K to 5.0 K are presented in Figure 5.6a. R_{xx} exhibits a characteristic dip at small magnetic field regime, and this phenomenon is identified as WAL, indicating an existence of strong spin-orbit interaction in Te originated from its high atomic number and large electronic polarizability [58]. The WAL effect comes from a system with spin-orbit coupling in which the spin of a carrier is coupled to its orbit momentum. The spin of the carrier rotates as its goes around a self-intersecting path, and the direction of this rotation is opposite for the two branches of the loop. Because of this, the two paths along any loop interfere destructively, which leads to a lower net resistivity. The importance of WAL is based on the consequence of spin-momentum locking and the full suppression of backscattering, resulting in a relative Berry phase acquired by carriers executing time-reversed paths. WAL is not an effect possessed only by Dirac materials, such as topological insulators and graphene, but a generic characteristic of the materials with strong spin-orbit coupling. WAL is temperature dependent as shown in Figure 5.6a. We measured more than 10 devices with different film thick-

ness, charge density and mobility. All show WAL characteristic. We use another sample with a similar thickness of 27.0 nm but more pronounced WAL features for the quantitatively analysis presented here (Figure 5.6d). As expected, the effect is strongly temperature-dependent and shows a deep peak at base temperature of 0.4 K. In addition, the effect diminishes when the temperature increases to 10 K, at which the localization is suppressed due to the decreased phase coherence length and spin-orbit scattering length at higher temperatures. We consider Hikami-Larkin-Nagaoka (HLN) formula [109] in the presence of spin-orbit coupling to discuss the WAL effect in Bz field. We fit the low-field portion of the magneto-conductance curves using the HLN model,

$$\Delta\sigma(B) = \sigma(B) - \sigma(B=0) = n_s n_v (F(\frac{B}{B_\phi + B_{so}}) - \frac{1}{n_s}(F(\frac{B}{B_\phi}) -$$

$$F(\frac{B}{B_\phi + 2B_{so}})))$$

$$F(Z) = \Phi(\frac{1}{2} + \frac{1}{Z} + ln(Z)), B_\phi = \frac{\hbar}{4eL_\phi^2}, B_{so} = \frac{\hbar}{4eL_{so}^2}$$

where Φ is the digamma function, L_ϕ is the phase coherence length, L_{so} is the spin-orbit scattering length, e is the electronic charge, $\hbar$ is the reduced Plancks constant, B is the magnetic field, and n_s and n_v are spin degeneracy and valley degeneracy, respectively. Figure 5.6e shows the phase coherence length L_ϕ and the spin-orbit scattering length L_{so} as a function of temperature. We should note that the maximum phase coherence length extracted from the small magnetic field portion is 1.8 m at 0.4 K at -30 V back gate bias. As we increase the temperature from 0.4 K to 10 K, the temperature dependence of the phase coherence length demonstrates a strong power-law behavior of $L_{so} \sim T^{-\gamma}$ with a power exponent γ approximately 0.5. This value matches the observation from previous studies that electron-electron or hole-hole scattering would give L_ϕ proportional to $T^{-0.5}$ in a 2D system31. However, more refined experiments are needed to reveal its special transport property of 1D van der Waals structure in 2D thin film system when the magnetic field is perpendicular to

the 2D plane. We find that L_{so} is also temperature dependent, and the maximum spin-orbit scattering length at base temperature of 0.4 K is $\sim 1.1~\mu$m, and this number is promising for future Te-based spintronics applications.
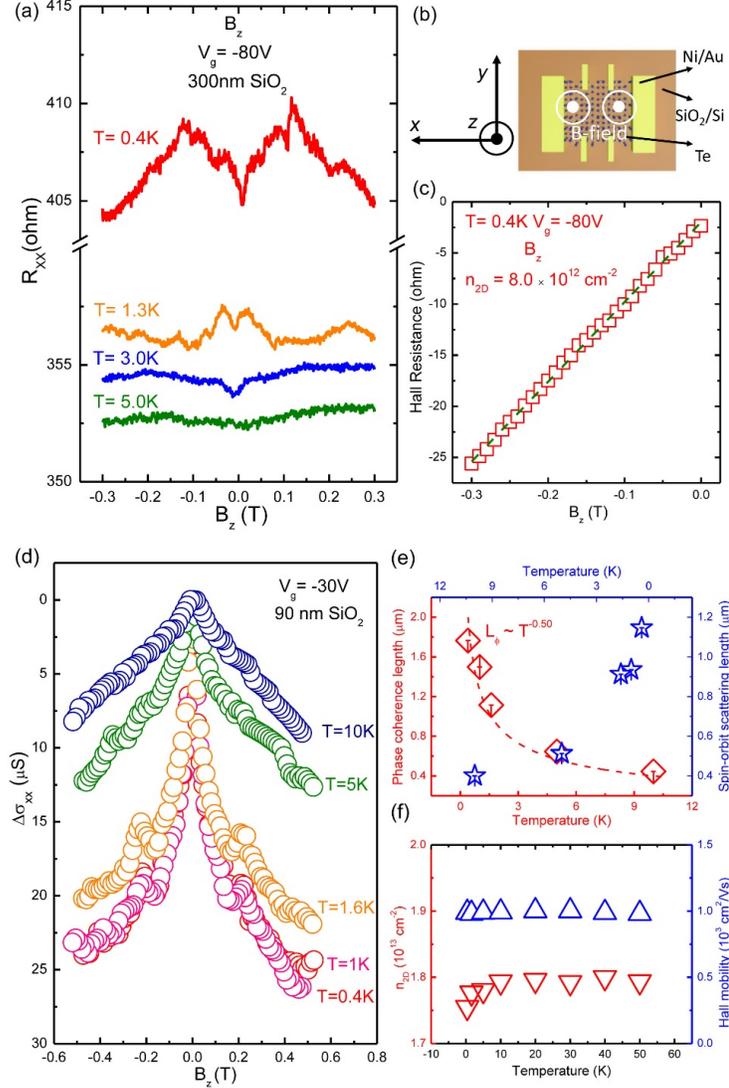
Fig. 5.6. (a) Magneto-resistance of Te thin film with varied B_z field for different temperatures. (b) Device scheme configuration and magnetic field indicator. (c) Hall effect of Te thin film with varied B_z field at base temperature of 0.4 K, and -80 V. (d) A different sample that has a pronounced WAL effect. (d) Phase coherence length and spin-orbit scattering length extracted from WAL effect vary with measured temperatures. Error bars are determined from HNL fittings. (f) 2D carrier density and Hall mobility as a function of temperatures.

Temperature dependence of carrier concentration and mobility of Te are examined in this work as well, as depicted in Figure 5.6f. The 2D carrier density n_2D is determined from $n_{2D} = \frac{B}{e\rho_{xy}})$, with a magnitude of $1.8 \times 10^{13} cm^{-2}$ in thin film Te is recorded at -30 V back gate bias and 0.4 K. Hall mobility, obtained from $_H = \frac{L}{W} \frac{1}{R_{xx} n_{2D} e}$, where L is the channel length, W is the channel width, and R_{xx} is the longitude resistance, has been measured with various temperatures. The Hall mobility remains constant at cryogenic temperatures with a maximum value of 1,002 cm^2/Vs. We calculate the mean free path of Te thin films by applying equation, $l_m = \tau v_F$, where τ is the carrier lifetime and v_F is Fermi velocity. Related mobility and 2D carrier density are extracted from Figure 5.6e and 5.6f. The estimated mean free path is $\sim$ 700 nm at $\mu = 1,002$ cm^2/Vs and $n_{2D} = 1.8 \times 10^{13} cm^{-2}$ which is comparable with our coherence length extracted from WAL effect. In our experiment, more than 10 samples have been systematically fabricated and measured, and a maximum mean free path of $\sim 1\mu m$ is obtained with a sample that has $\mu \sim 2000$ cm^2/Vs and $n_{2D} = 8 \times 10^{12} cm^{-2}$, which indicates a decent quality of our single crystal Te thin films.

5.1.4   Magneto-transport of Te in B$_x$ Direction

Figure 5.7a shows the magneto-resistance of Te at different temperatures, in which the WAL effect is also observed within small magnetic field regime. In addition, Universal conductance fluctuation (UCF) effect has been observed in our Te thin film at high fields. UCF is a quantum interference effect of diffusive charge carriers, observed commonly in the mesoscopic systems of semiconductors, metals, and 2D Dirac graphene. The mesoscopic nature or finite size of a weakly disordered sample results in the loss of the self-averaging of its physical properties [110]. Applying a magnetic field in semiconductors varies the phase of the wave function of a charge carrier, where the magnitude and interval of conductance fluctuation are closely related to the phase coherence length. The UCF effect, as presented in Figure 5.7c, is observed in our Te thin film sample within the moderate magnetic field and low temperature regime,
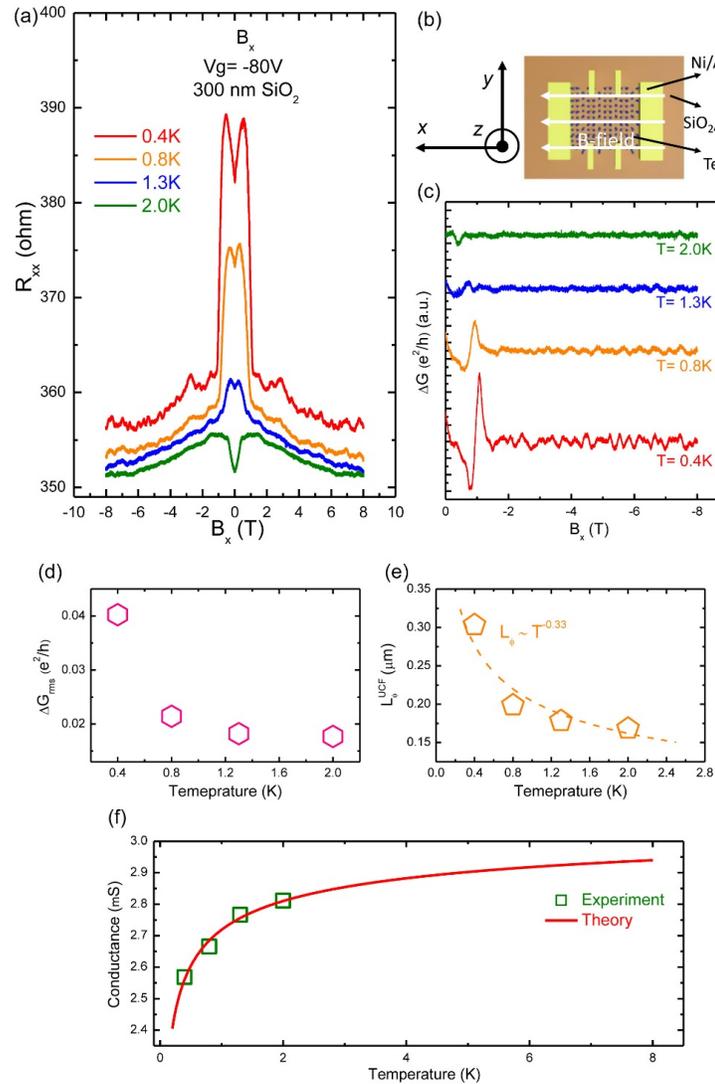
Fig. 5.7. (a) Magneto-resistance of Te thin film with varied B_x field for different temperatures. (b) Device scheme configuration and magnetic field indicator. (c) $\Delta G(T)$ curves with varied B_x field. The UCF effect is robust, and persisting to increased temperature up to 2 K. (d) ΔG_{rms} changes with different measured temperatures. (e) The phase coherence length has demonstrated a strong power-law behavior. (f) Temperature dependence of the conductance at zero magnetic field.

and this phenomenon is robust, and persisting to increased temperature up to 2 K. The periodic conductance fluctuation patterns can be observed repeatedly, and they present the similar features in the different magneto-conductance curves measured at

different temperatures. To quantitatively compare the measured UCF magnitudes with theoretical predictions, we have generated root-mean-square (rms) magnitude of the magneto-conductivity fluctuations,

$$\Delta G_{rms} = \sqrt{\langle [\Delta G(B) - \langle \Delta G(B) \rangle]^2 \rangle}$$

where $\langle ... \rangle$ denotes an average over the magnetic field which is an ensemble average over impurity configurations. Extracted ΔG_{rms} is demonstrated in Figure 5.7d with different temperatures. UCF theory predicts a fluctuation magnitude of 0.73 e^2/h for a weakly disordered, 1D mesoscopic wire at T=0 K and at zero magnetic field31. At T 0 K, we limit our discussion to the 1D regime where the coherence length is much shorter than the sample size L (6 μm), and the Te chain can be considered as a series of uncorrelated segments of length L_ϕ^{UCF}. The relation between fluctuations rms and L_ϕ^{UCF} can be described in 1D system as [111, 112],

$$\Delta G_{rms} = \sqrt{12} \frac{2e^2}{h} \left(\frac{L_\phi^{UCF}}{L} \right)^{3/2}$$

The obtained values of L_ϕ^{UCF} extracted from observed UCF amplitudes can be used to verify the anisotropic property by comparing with L_ϕ from WAL effect along B$_z$. As shown in Figure 5.7e, the behavior of L_ϕ^{UCF} is significantly different from what we saw in Figure 5.6e, and we interpret it as the result of the anisotropic transport in Te where 1D chain transport differs from 2D thin film transport. The extracted phase coherence lengths from UCF follow a power law dependence of temperature $L_\phi \sim T^{-0.33}$, consistent with the dephasing mechanism being the carrier-carrier collisions with small energy transfers as observed commonly in 1D nanowire systems with an exponent value of [111, 112]. Finally, we discuss the pronounced temperature dependent features of the conductance near zero magnetic field, presented in Figure 5.7a as huge peaks in magneto-resistance. Due to the localization effect within the small magnetic fields, it is hard to determine the real conductance at exact zero magnetic field. Instead of reading the numbers at magnetic field equals to zero, we use peak

conductance near ± 0.5 T as $\sigma(\text{B}=0)$ which we believe this value is approximately the intrinsic zero-field magneto-conductance with localization effect excluded. For the maximum gate bias of -80 V, conductance in 1D system is given by,

$$\sigma(T) = \sigma_0 - \frac{2e^2}{h}\frac{L_\phi}{L}$$

since we have found that $L_\phi \sim T^{-0.33}$, we can rearrange our equation by replacing with phase coherence length with temperature. We fitted our experimental data from 0.4 K up to 2.0 K with a constant Drude conductance, and theoretical prediction is shown in red solid line as depicted in Figure 5.7f. The functional form of the fit is consistent with the experimental data within low temperature, since our discussions are in quantum coherent regime. This result further confirms the 1D transport nature of Te thin films when the applied magnetic field is aligned with the helical atomic chains.

5.2 Magneto-Transport of n-type Tellurene

5.2.1 SdH Oscillations and Quantum Hall Effect

Due to the unintentional p-type dopants in Te, the chemical potential is usually fixed near the valence band edge. Therefore so far most of the experiments are limited to holes and little about the properties of the conduction band has been investigated via transport measurements [67, 87, 113]. Here we managed to dope tellurene films into n-type using atomic layer deposited (ALD) dielectric doping technique without degrading electron mobility [114, 115], which grants us the access to the conduction band and explore much more exotic physics. The schematic and the optical image of an n-typed doped device is demonstrated in Figure 5.8a and 5.8b. The as-synthesized tellurene films were dispersed on to a degenerately doped silicon substrate with a 90 nm SiO_2 insulating layer on top, followed by patterning and deposition of Ti/Au metal contacts. Here we chose low work function metal contacts Ti to reduce the electron

Schottky barrier height and accommodate n-type transport. A layer of alumina was subsequently deposited onto tellurene film by ALD grown at 200 °C, converting the tellurene film underneath from p-type to n-type, as confirmed by I_d-V_g transfer curves of a tellurene field-effect transistor (FET) at both room temperature and cryogenic temperature (see Figure 5.8c). Similar ALD doping method has also been reported on other material systems like black phosphorus [22,23,116] and silicon [117]. The doping mechanism is attributed to the threshold voltage shift caused by positive fix charges in low-temperature ALD-grown films [22] or the interface electric dipole field [117].
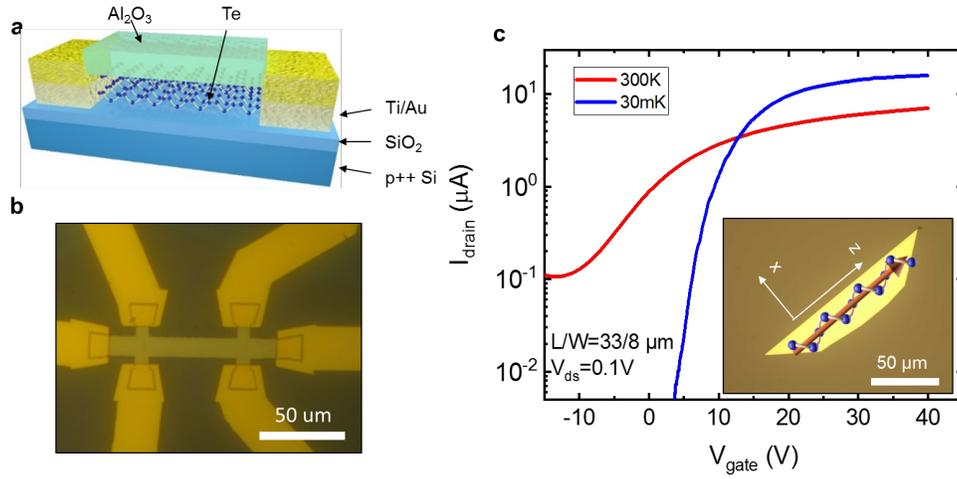
Fig. 5.8. Device structure for n-type QHE measurement. (a) Schematics of ALD doped n-type device. (b) The optical image of n-type Hall bar device. (c) Transfer curves of the Hall bar device measured at room temperature and cryogenic temperature confirming the n-type doping effect.

We investigated over 20 devices with typical film thickness ranging from 10 to 20 nm, and all of them exhibit similar and reproducible behaviors in general. Here all the data presented is from one high-quality device, unless otherwise specified. The global back gate allows us to tune the 2D electron density from 2 to $10 \times 10^{12}\,cm^{-2}$. Representative longitudinal (R_{xx}) and transverse (R_{xy}) magnetoresistance curves measured at V_g=10V are plotted in Fig. 5.9a, with Hall density of $2.5 \times 10^{12}\,cm^{-2}$ and Hall mobility of 6,000 cm^2/Vs. The onset of SdH oscillations is around 2 T, leading to an

estimated quantum mobility of 5,000 cm^2/Vs, which is close to Hall mobility within a reasonable margin. At B field around 24 T and 32 T, Rxy is fully quantized into integer fraction of h/e^2 (corresponding to filling factor of 3 and 4), and Rxx also drops to 0 – a hallmark of QHE [91]. As shown in Fig. 5.9b, by fixing B field at 42 T and sweeping back gate, all filling factors from 2-8 are resolved (although not all fully quantized due to Landau level broadening), suggesting all the degeneracies, including spin and valley, have been lifted and the system reaches quantum Hall ferromagnetism regime.
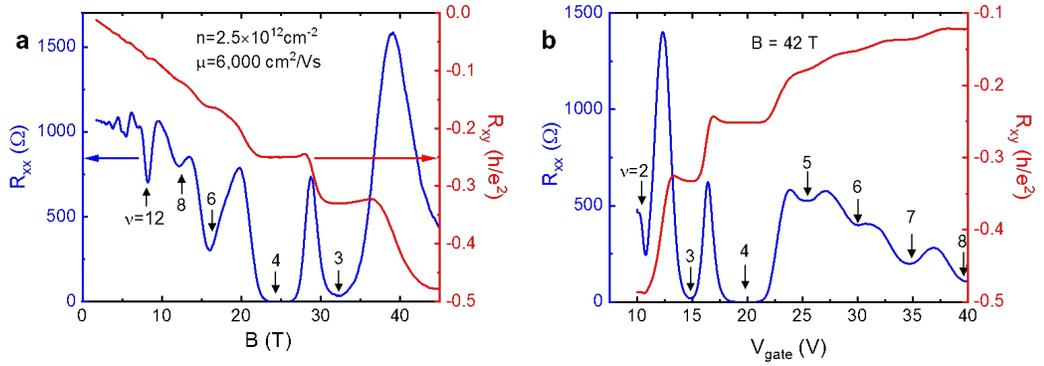
Fig. 5.9. QHE in n-type 2DEGs in tellurene films. (a) Longitudinal (R$_{xx}$, in blue) and transverse (R$_{xy}$, in red) resistance as a function of magnetic field. (b) R$_{xx}$ and R$_{xy}$ a function of back gate voltage. The gate oxide is 90 nm SiO$_2$.

By mapping out R$_{xx}$ through the Vg-B parameter space, we can construct the Landau fan diagram in a color map as in Figure 5.10. The data section from 0 to 12 T and from 12 T to 45 T were acquired from two different magnet systems at 30 mK and 300 mK, respectively, therefore the data shows slight discontinuity at B=12 T. Since the conduction band edge is located at two inequivalent H (H') points in the first Brillouin zone accounting for two-fold valley degeneracy, it is intuitively conceivable that each Landau level consists of four degenerate energy states (2 for valley degeneracy and 2 for spin degeneracy) like graphene, with cyclotron energy gap $E_c = \hbar\omega_c = \frac{\hbar e B}{m^*}$ at filling factor of 4, 8, 12 . Following this argument, we

should expect the energy gap to increase monotonically in the sequence of 4n as we approach lower filling factors, since the cyclotron energy $\frac{\hbar eB}{m^*}$ increases linearly with the magnetic field. Yet we notice from Fig. 2b that the gap at ν=12 is larger than that at ν=8, suggesting the origin of these two gaps are different and the four-level single particle picture cannot explain these unconventional sequence, hence another degree of freedom needs to be taken into account.
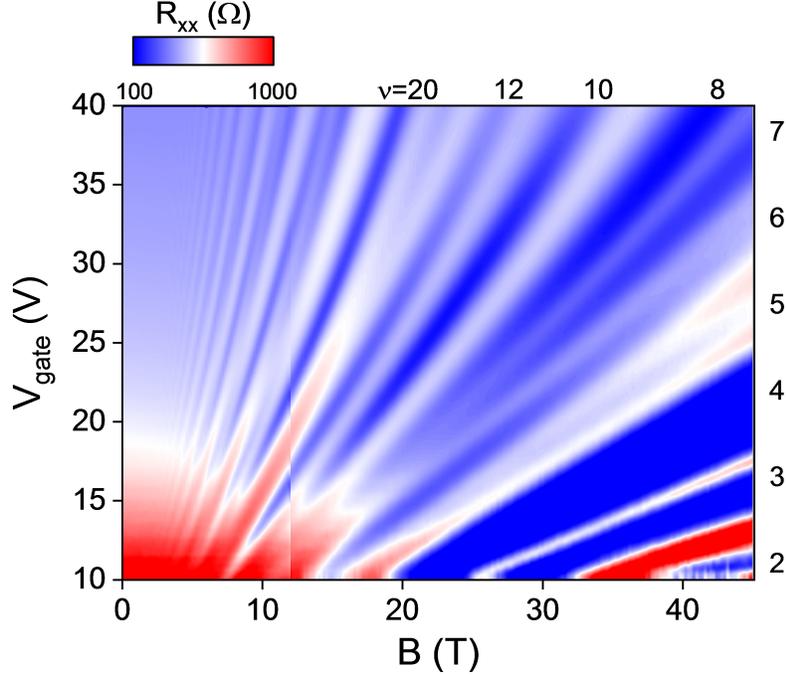
Fig. 5.10. Color mapping of R$_{xx}$ by sweeping both back gate voltage and magnetic field. The data from 0-12 T and 12-45 T are measured from the same device in a superconducting magnetic system at 30 mK and a hybrid magnetic system at 300 mK, respectively.

5.2.2   QHE in a Wide Quantum Well and SU(8) Symmetry

To understand this anomaly, we first focus on SdH oscillation features at relatively low B field regime (see Figure 5.11a). When B field is below approximately 7 T, only one set of oscillations is observed, and the oscillation frequency BF can be used to extract carrier density: $n_{SdH} = (eB_F)/h = 1.02 \times 10^{12} \, cm^{-2}$, where degree of

degeneracy is not taken into account. Meanwhile we can also calculate the total carrier density from the slope of R_{xy} to be $n_{Hall} = 8.75 \times 10^{12} \, cm^{-2}$, which is approximately 8 times larger than n_{SdH}, implying that there is eight-fold degeneracy. At B field over 7 T, two sets of oscillations are resolved as marked by red and blue arrows alternatively in Figure 5.11a.
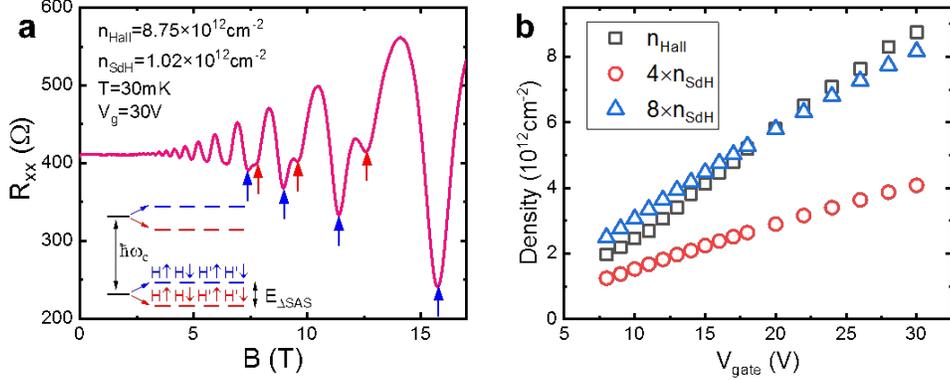
Fig. 5.11. Approximate SU(8) symmetry of isospin space in QHE regime. (a) SdH oscillations evolving from eight-fold degeneracy to two sets of resonant oscillation features (blue and red arrows). Inset: illustration of degenerate energy levels with symmetric-antisymmetric energy splitting. (b) Comparison of Hall density and SdH density under different gate biases.

There are several plausible explanations of two sets of oscillations: (a) a second sub-band; (b) another electron pocket at other point(s) of Brillouin zone; (3) two coupled layers of charge at the top and bottom of a wide quantum well [118–121]. However, both multiple sub-bands and pockets assumptions involve two Fermi surfaces and introduce two sets of independent oscillations with different frequencies since BF is proportional to the area of the Fermi surface, and the ratio of two Fermi surface areas can be modulated by tuning the carrier density. This will be reflected in two independent oscillation frequencies in the fast Fourier transform. However, in our experiments only one frequency (and its higher order of harmonics) can be found in frequency domain (see Figure 5.12), and the ratio of n_{Hall}/n_{SdH} remains to be 8

throughout the entire gate range that we can probe (Figure 5.11b). This solidifies the coupled wide quantum well assumption to be the only reasonable explanation. Because of the doping profile of ALD dielectrics, two layers of carriers are induced at the top and the bottom of the Te film when appropriate gate bias is applied (Figure 5.14a top panel). Should the central potential barrier be low enough, electron tunneling is permitted between two layers, and their wave functions will interfere and be reconstructed into symmetric and anti-symmetric states (bottom panels of Figure 5.14a and b). In this case, the Landau levels in two layers will become resonant despite a small energy gap ΔE_{SAS}, which is related to the width of the quantum well (film thickness) and applied gate voltage. When ΔE_{SAS} is sufficiently small compared to Landau level gaps (as shown in the inset of Figure 5.12a), we can treat the near degenerate symmetric-antisymmetric energy levels as another type of isospin which, along with real spin and valley isospin, yields an approximate SU(8) symmetry group [122].
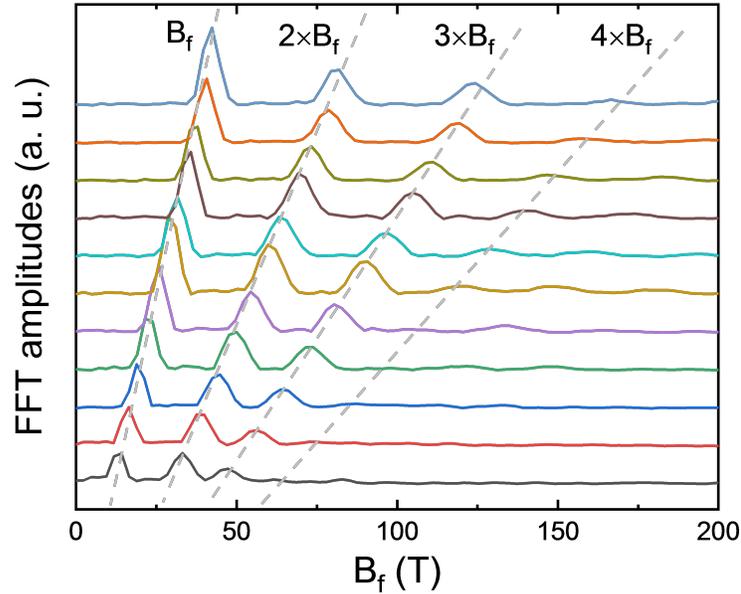

Fig. 5.12. FFT amplitudes of SdH oscillations. Only one set of frequency and its higher order harmonics can be detected.

To further verify the wide quantum well assumption, we fabricated a double-gate device by adding a metal gate on top of ALD alumina, as shown in Figure 5.13a. R_{xx} is mapped out as a function of both top gate voltage and back gate voltage at a fixed B field of 7 T in Figure 5.13c. The tilted strips in the lower left corner with negative slope suggest that two layers of electrons are coupled and the Fermi level can be tuned by both of the gates. However when both gates are strongly positive biased (in the upper right corner of Figure 5.13c), the electrons are strictly localized near two surfaces and each gate can only modulate one set of oscillations. In this case the tilted lines will evolve into straight lines, which is a signature of wide quantum well and has been observed in other quantum well systems [123,124]. Ideally, in the upper right regime of Figure 5.13c, we should observe a chessboard feature with two sets of oscillations each controlled by one gate independently [124]. However the horizontal patterns are almost indiscernible, probably due to the low mobility at top interface between tellurene and ALD alumina.

We now focus on assigning the quantum Hall isospin ferromagnetic states to each filling factor by fixing the perpendicular magnetic field $B_\perp$ and increasing the total magnetic field B_{total}. Three competing mechanisms can break SU(8) isospin symmetry: (1) the real spin can be resolved by Zeeman splitting with an energy gap proportional to the total magnetic field: $\Delta E_z = g^* \mu_B B_{total}$, where g^* is effective g-factor and μ_B is the Bohr magneton; (2) ΔE_{SAS} is in general irrelevant to perpendicular magnetic field $B_\perp$, but the in-plane magnetic field can destroy this energy gap and collapse the symmetric and anti-symmetric energy levels [118]; (3) the valley isospin is usually polarized by breaking inversion symmetry or electron interactions [125,126]. Figure 5.14a shows R_{xx} versus V_{bg} at fixed $B_\perp$=25 T and B_{total} is increased from 25 T to 45 T. The gaps in ν=5 and ν=7 start to collapse with increasing B_{total}, which can be attributed to the in-plane magnetic field destroying ΔE_{SAS} [118] (another plausible explanation of band crossing due to large Zeeman splitting like in WSe$_2$ case [127] can also be ruled out by absence of coincident effect, see Supporting Information 2). Therefore we can assign the odd filling factors to the symmetric-antisymmetric en-
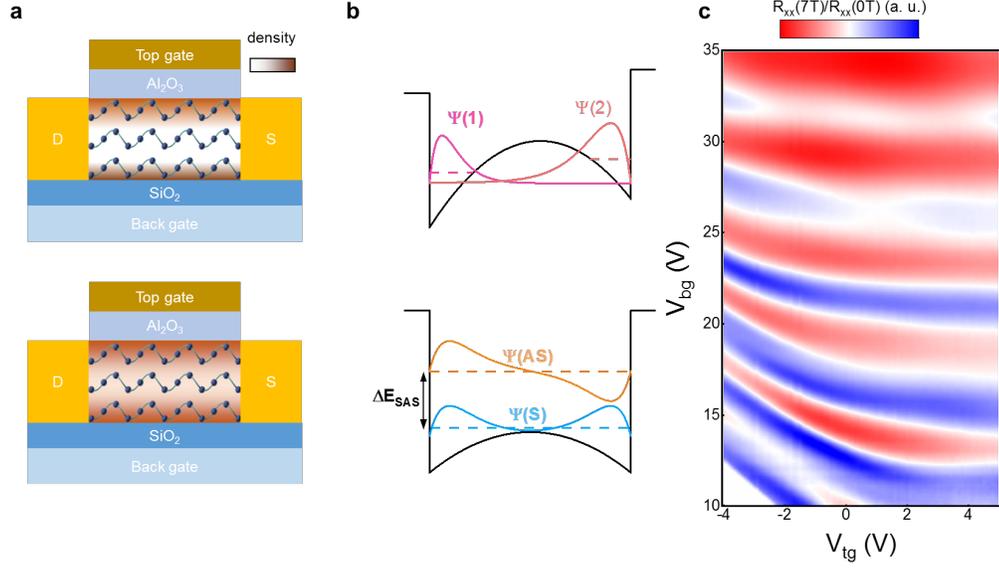
Fig. 5.13. Wide quantum well in tellurene. (a) Schematics of double-gated devices and carrier distribution of separate layers (top) and correlated layers (bottom). (b) Potential profile and wave function distribution of separate layers (top) and correlated layers (bottom). (c) Color mapping of normalized $R_{xx}/R_{xx}(B=0)$ by sweeping both top gate and back gate. The data is acquired at a magnetic field of 7 T. — FFT amplitudes of SdH oscillations. Only one set of frequency and its higher order harmonics can be detected.

ergy gap ΔE_{SAS}. On the contrary, the gaps in filling factor ν=6 and 8 are expanded, however this can be related to either the increasing of the Zeeman energy gap, or the collapsing of ΔE_{SAS} in neighboring odd filling factors. Hence, at this point we cannot explicitly determine the sequence of spin and valley splitting, and further investigation is needed to completely understand the mechanism that drives the system to fully polarized ferromagnetism regime.

5.2.3 Weyl Semiconductors and Massive Weyl Fermions

Finally we present the evidence of massive Weyl fermions in conduction band edge of Te. Weak anti-localization (WAL) effect is observed in near-zero magnetic field,
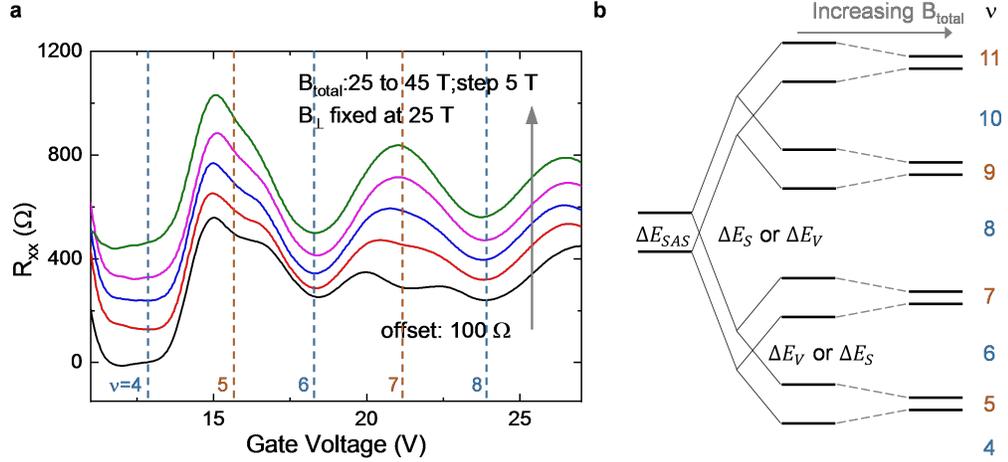
Fig. 5.14. Quantum Hall ferromagnetic states under a titled B field. (a) R_{xx} versus gate voltage measured at a fixed perpendicular magnetic field 25 T and increasing total magnetic fields (with 100 Ω offset). Here the dashed lines correspond to filling factors from 4 to 8. (b) Sequence of competing mechanism lifting degeneracies within a Landau level.

manifesting strong SOC effect in Te system – a direct consequence of lacking inversion symmetry and heavy atoms of Te. The strong SOC gives rise to spin-polarized band crossing at H and H' point (as shown in Figure 5.15a), which is protected by three-fold rotational symmetry. This point at H (H') can be classified as a Weyl node that can be viewed as a Berry curvature monopole in the momentum space. We shall address that unlike normal band-inversion-induced Weyl points which usually lead to linear band dispersion of Weyl semimetals that can hardly be tuned by gate, the chirality-induced Weyl nodes in Te are located at the edge of the conduction band, and therefore Te belongs to a new type of topological material – Weyl semiconductor, which grants us more freedom to probe the topological properties of Weyl nodes and to design novel electronic and quantum devices by taking advantage of the versatility of the semiconductors. Evidence of Weyl fermions such as negative magnetoresistance [128] and kinetic magnetoelectric [129] effect in bulk Te has been reported. Here we present a much more convincing evidence– the observation of non-trivial π Berry phase in

magneto-transport. The amplitude of SdH oscillations, when neglecting all degree of degeneracy, is described as:

$$\Delta R_{xx} \propto R(B,T) \times cos(2\pi(\frac{B_F}{B} + \frac{1}{2}) + \varphi),$$

where B_F is the oscillation frequency and φ is the Berry phase. To extract the Berry phase, we record the values of 1/B at each ΔR_{xx} minima and plot them against the Landau level index, as shown in Figure 5.15b. The extrapolated the linear fitting curves intercept with y-axis at 1/2 (see Figure 5.15c and 5.15d), which is the signature of non-trivial π Berry phase, as observed in many other Dirac or Weyl topological materials3 [3, 4, 101, 130–132]. The origin of the Berry phase is substantially rooted in the hedgehog-like spin texture [42, 63] near the chirality-induced Weyl nodes. The spin texture are either pointing at or away from the Weyl nodes as illustrated by red arrows in Figure 5.15a. Under magnetic field, when an electron completes a cyclotron motion in the real space, its momentum changes by 2π, corresponding to a closed loop trajectory around the Fermi surface in momentum space. Along this path, the spin of the electron also rotates by 2π, which picks up a π Berry phase, since electrons are spin-1/2 particles. The origin of Berry phase in Te resembles that near the Dirac points of graphene, except that in graphene the Berry phase in induced by radial pseudospin (valley isospin) texture rather than the real spin as in Te.

Band-inversion-induced nodal structures are usually accompanied with linear band dispersion that gives rise to the massless relativistic particles like Dirac/Weyl fermions. However this is not necessarily always the case. The Dirac/Weyl nodes only guarantee the topological properties, but the band dispersion can still be arbitrary, depending the energy scale of interest. Here we measure SdH oscillation amplitudes as a function of temperature (Figure 5.16a), which can be described by the LifshitzKosevich equation:

$$\Delta R_{xx} \propto \frac{2\pi^2 m^* k_B T/\hbar eB}{sinh(2\pi^2 m^* k_B T/\hbar eB)},$$
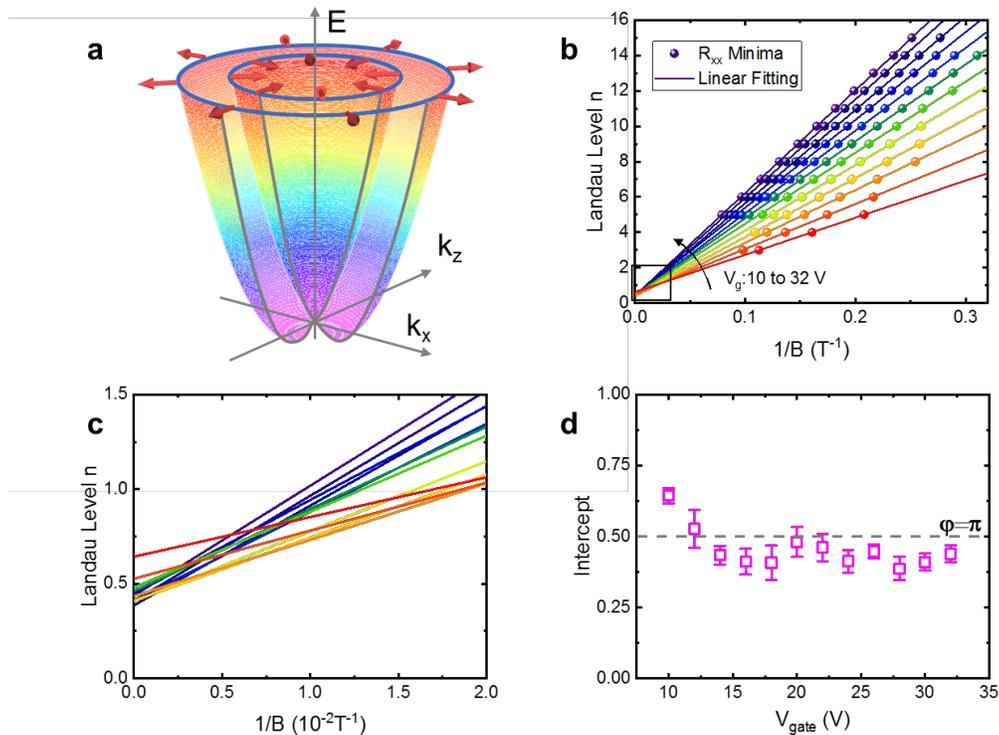
Fig. 5.15. Weyl nodes and Berry phase near Te conduction band edge. (a) Weyl node at H point induced by strong SOC in chiral crystal. The red arrows around the Fermi surface represent hedgehog-like spin texture. (b) Landau fan diagram under different gate bias. The scattered symbols are read off from the value 1/B of each minima in R_{xx} and plotted against the Landau level index. Straight lines are linear fitting under each gate bias. (c) Zoom in of black box in b with linear fittings extrapolated to the y-axis. (d) Intercept of linear fittings versus gate voltage. The error bars come from the linear fitting. The reference line at y=0.5 corresponds to π Berry phase.

. The effective mass is then extracted to be about 0.10 m_0 (where m_0 is the bare electron mass) throughout the entire gate range, which is consistent with previously reported value of bulk Te [133, 134]. This suggests that although the Weyl nodes reside only several meV above the conduction band edge, the topological properties (Berry phase) and the band mass carry over to a much broader energy window of at least 50 meV as the gate can access to. Therefore n-type tellurene film is an ideal

playground to study the behavior of massive Weyl fermions with tunable chemical potentials.
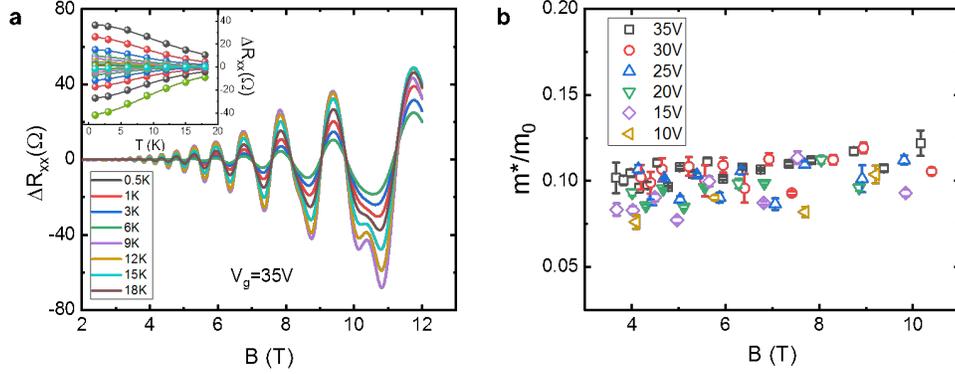
Fig. 5.16. Temperature-dependent SdH oscillations and effective mass of Weyl fermions. (a) SdH oscillation amplitudes (subtracting a smooth background) under various temperature from 0.5 K to 18 K. Inset: ΔR_{xx} versus temperature fitted by LifshitzKosevich equation. (b) The effective mass is extracted to be about 0.10 m_0, and it is independent on gate biases and magnetic fields.

5.3 Summary

In this chapter, we investigated magneto-transport in high mobility tellurene films with strong 2D confinement. For p-type devices, QHE was observed on Te for the first time with four-fold degeneracy. Well-developed Shubnikov-de-Haas oscillations were thoroughly studied under different gate bias, temperatures, and tilted magnetic fields. Anomaly in cyclotron effective mass and transfer characteristics at large magnetic fields and low temperatures were also observed, which is attributed to the interplay of Zeeman splitting and strong Rashba-like spin-orbit coupling in Te. Our work revealed the intriguing electronic structure of Te valence band through quantum transport and demonstrated high quality of the novel 2D tellurene material system which is suitable to even explore exotic topological phenomena in Te.

Using ALD dielectric doping on high-quality tellurene films, for the first time, we observed well-developed quantum Hall effect from 2D electrons in tellurene and accessed the electronic structure of its conduction band. A wide quantum well model with two correlated electron layers is proposed to explain the anomaly in SdH oscillations and quantum Hall sequences. Eight-fold degeneracies, including real spin, valley isospin and symmetric-antisymmetric isospin are all lifted under a 45 T external magnetic field, leading to fully polarized quantum Hall ferromagnetic states. Topologically non-trivial π Berry phase is ambiguously detected as a direct evidence of massive Weyl fermions in the vicinity of chirality-induced Weyl nodes with predicted hedgehog-like spin textures. Our work offers a material platform to explore the topological properties of massive relativistic quasiparticles in chiral semiconductors with strong SOC.

6. CONCLUSION

In 1972, eight years prior to his discovery of quantum Hall effect on silicon MOSFETs, Klaus von Klitzing completed his doctorate degree from University of Wurzburg and the title of his thesis was Galvanomagnetic Properties of Tellurium in Strong Magnetic Fields, where a comprehensive study of magneto-transport on high mobility bulk Te samples were carried out. At that time the key experimental requirements for quantum Hall effect were almost met: low temperature, high magnetic field and high mobility samples. The only missing piece of the puzzle that prevents the quantum Hall effect from being discovered eight years in advance was lacking strong 2D confinement.

In this dissertation, 2D Te film-tellurene was introduced to bridge the gap between the exotic physics of Te and the quest for realizing 2DEG in Te system. The work not only investigates tellurene as a potential candidate for future electronics but also lays a solid ground for exploring the physics of Te in 2D limit in device perspective. Here we will summarize the major achievements of this dissertation.

In **Chapter 2**, a solution based hydrothermal growth method was proposed to synthesize 2D Te films for the first time. The geometry, i.e. Thickness, lateral size, and aspect ratio, can be tuned by controlling the reaction time and starting material composition. Few-layer and even mono-layer tellurene was also achieved as confirmed by AFM. A comprehensive characterization was performed to determine the crystal structure and orientation using TEM and Raman technique. We also found that the Raman spectrum is also sensitive to the thickness, since Raman vibrational modes can be altered as stronger 2D confinement is imposed. Finally, anisotropic strain response were also measured, as a direct evidence of 1D vdW structure being confirmed by mechanical method.

Chapter 3 focuses on exploring the fundamental electrical performance of tellurene-based transistors. Long channel p-type FETs were first fabricated to study the in-

trinsic electrical properties and minimize the influence from contact resistance. Field-effect mobility and on/off ratio as a function of film thickness were statistically measured. The mobility peaks at 700 cm^2/Vs at around 15 nm thickness and the on/off ratio exceeds 10^6 in sub-5 nm films. An anisotropic mobility ratio of 1.43 were also determined, suggesting 1D chain direction is the favorable axis for fabricating devices. Through channel length and EOT scaling, along with contact engineering, the device performance were further boosted with large drive current over 1 A/mm. A self aligned top-gate stack formation process was developed, which shows great potential for fabricating ultra-scaled logic devices. Finally Te NW transistors were also briefly discussed.

In **chapter 4**, we further explored the potential applications of tellurene from CMOS to thermoelectric device. Due to the unintentional doping, the chemical potential of Te is pinned close to the valence band and it is in principle difficult to achieve n-type devices. We developed an ALD dielectric doping technique which uses the fixed charges in ALD layer to change V_{th} and effectively dope the Te transistors into n-type. The doping level can also be tuned with different ALD oxide type, thickness and deposition temperature. The mobility and device performance for both n-type and p-type devices are near symmetric and prototypical CMOS inverter was demonstrated. Te has also been considered an excellent thermoelectric material because of its high electric conductivity and low thermal conductivity. We also found the ZT value in 2D Te films was enhanced to 0.63, almost twice as high as its bulk value. The enhancement of thermoelectric efficiency arises from the difference of mean free paths between electrons and phonons. The reduced film thickness can block the phonon propagation yet electron transport is almost undisrupted. Finally we use photo-current mapping to visualize the laser induced thermoelectric current distribution. accumulation-type contacts between Te and Pd were also directly confirmed using photovoltaic effect.

In **chapter 5**, we summarized the magneto-transport measurement performed on both n-type and p-type tellurene. For p-type samples, SdH oscillations are well-

resolved due to enhanced 2D confinement. Anomaly in quantum transport were identified and can be explained with the interplay between SOC and Zeeman splitting, which causes the evolution of camelback-like valence band edge under external magnetic field. The WAL effect were also measured in p-type samples along different prime axis as a direct evidence of strong SOC effect. The electron mobility is even higher in n-type samples (near 6,000 cm^2/Vs), which enables the observation of well-developed quantum Hall states and SdH oscillations with near SU(8) symmetry in a wide quantum well structure. Evidence of massive Weyl fermions were also observed with topologically non-trivial π Berry phase, which opens a new era to study the behavior of relativistic particles in low energy spectrum of semiconductor materials.

REFERENCES

[1] M. Chhowalla, D. Jena, and H. Zhang, "Two-dimensional semiconductors for Transistors," *Nature Reviews*, vol. 1, p. 16052, 2016.

[2] A. H. Castro Neto, F. Guinea, N. M. R. Peres, K. S. Novoselov, and A. K. Geim, "The electronic properties of graphene," *Reviews of Modern Physics*, vol. 81, no. 1, pp. 109–162, 2009.

[3] K. S. Novoselov, A. K. Geim, S. V. Morozov, D. Jiang, M. I. Katsnelson, I. V. Grigorieva, S. V. Dubonos, and A. A. Firsov, "Two-dimensional gas of massless Dirac fermions in graphene," *Nature*, vol. 438, no. 7065, pp. 197–200, 2005.

[4] Y. B. Zhang, Y. W. Tan, H. L. Stormer, and P. Kim, "Experimental observation of the quantum Hall effect and Berry's phase in graphene," *Nature*, vol. 438, no. 7065, pp. 201–204, 2005.

[5] K. S. Novoselov, Z. Jiang, Y. Zhang, S. V. Morozov, H. L. Stormer, U. Zeitler, J. C. Maan, G. S. Boebinger, P. Kim, and A. K. Geim, "Room-Temperature Quantum Hall Effect in Graphene," *Science*, vol. 315, no. 5817, pp. 1379–1379, 2007.

[6] B. Hunt, T. Taniguchi, P. Moon, M. Koshino, and R. C. Ashoori, "Massive Dirac Fermions and Hofstadter Butterfly in a van der Waals Heterostructure," *Science*, vol. 340, no. June, pp. 1427–1431, 2013.

[7] Y. Cao, V. Fatemi, A. Demir, S. Fang, S. L. Tomarken, J. Y. Luo, J. D. Sanchez-Yamagishi, K. Watanabe, T. Taniguchi, E. Kaxiras, R. C. Ashoori, and P. Jarillo-Herrero, "Correlated insulator behaviour at half-filling in magic-angle graphene superlattices," *Nature*, vol. 556, no. 7699, pp. 80–84, 2018.

[8] Y. Cao, V. Fatemi, S. Fang, K. Watanabe, T. Taniguchi, E. Kaxiras, and P. Jarillo-Herrero, "Unconventional superconductivity in magic-angle graphene superlattices," *Nature*, vol. 556, no. 7699, pp. 43–50, 2018.

[9] C. Berger, Z. Song, T. Li, X. Li, A. Y. Ogbazghi, R. Feng, Z. Dai, N. Alexei, M. E. H. Conrad, P. N. First, and W. A. De Heer, "Ultrathin epitaxial graphite: 2D electron gas properties and a route toward graphene-based nanoelectronics," *Journal of Physical Chemistry B*, vol. 108, no. 52, pp. 19 912–19 916, 2004.

[10] A. Reina, X. Jia, J. Ho, D. Nezich, H. Son, V. Bulovic, M. S. Dresselhaus, and K. Jing, "Large area, few-layer graphene films on arbitrary substrates by chemical vapor deposition," *Nano Letters*, vol. 9, no. 1, pp. 30–35, 2009.

[11] K. S. Kim, Y. Zhao, H. Jang, S. Y. Lee, J. M. Kim, K. S. Kim, J.-H. Ahn, P. Kim, J.-Y. Choi, and B. H. Hong, "Large-scale pattern growth of graphene films for stretchable transparent electrodes." *Nature*, vol. 457, no. 7230, pp. 706–710, 2009.

[12] P. W. Bridgman, "Two new modifications of phosphorus," *Journal of the American Chemical Society*, vol. 36, no. 7, pp. 1344–1363, 1914.

[13] A. Brown and S. Rundqvist, "Refinement of the crystal structure of black phosphorus," *Acta Crystallographica*, vol. 19, no. 4, pp. 684–685, 1965.

[14] Y. Maruyama, S. Suzuki, K. Kobayashi, and S. Tanuma, "Synthesis and some properties of black phosphorus single crystals," *Physica B+ C*, pp. 99–102, 1981.

[15] M. Baba, F. Izumida, Y. Takeda, and A. Morita, "Preparation of black phosphorus single crystals by a completely closed bismuth-flux method and their crystal morphology," *Japanese Journal of Applied Physics*, vol. 28, no. 6 R, pp. 1019–1022, 1989.

[16] T. Nilges, M. Kersting, and T. Pfeifer, "A fast low-pressure transport route to large black phosphorus single crystals," *Journal of Solid State Chemistry*, vol. 181, no. 8, pp. 1707–1711, aug 2008.

[17] M. Köpf, N. Eckstein, D. Pfister, C. Grotz, I. Kroger, M. Greiwe, T. Hansen, H. Kohlmann, and T. Nilges, "Access and in situ growth of phosphorene-precursor black phosphorus," *Journal of Crystal Growth*, vol. 405, pp. 6–10, 2014.

[18] G. Qiu, Q. Nian, M. Motlag, S. Jin, B. Deng, Y. Deng, A. R. Charnas, P. D. Ye, and G. J. Cheng, "Ultrafast Laser-Shock-Induced Confined Metaphase Transformation for Direct Writing of Black Phosphorus Thin Films," *Advanced Materials*, vol. 30, no. 10, pp. 1–8, 2018.

[19] X. Li, B. Deng, X. Wang, S. Chen, M. Vaisman, S.-i. Karato, G. Pan, M. Larry Lee, J. Cha, H. Wang, and F. Xia, "Synthesis of thin-film black phosphorus on a flexible substrate," *2D Materials*, vol. 2, no. 3, p. 031002, 2015.

[20] H. Liu, A. Neal, Z. Zhu, Z. Luo, and X. Xu, "Phosphorene: An Unexplored 2D Semiconductor with a High Hole Mobility," *ACS nano*, vol. 8, no. 4, pp. 4033–4041, 2014.

[21] L. Li, Y. Yu, G. J. Ye, Q. Ge, X. Ou, H. Wu, D. Feng, X. H. Chen, and Y. Zhang, "Black phosphorus field-effect transistors," *Nature Nanotechnology*, vol. 9, no. 5, pp. 372–377, may 2014.

[22] D. J. Perello, S. H. Chae, S. Song, and Y. H. Lee, "High-performance n-type black phosphorus transistors with type control via thickness and contact-metal engineering." *Nature communications*, vol. 6, p. 7809, 2015.

[23] H. Liu, A. T. Neal, M. Si, Y. Du, and P. D. Ye, "The effect of dielectric capping on few-layer phosphorene transistors: Tuning the schottky barrier heights," *IEEE Electron Device Letters*, vol. 35, no. 7, pp. 795–797, 2014.

[24] M. Buscema, D. J. Groenendijk, G. a. Steele, H. S. J. van der Zant, and A. Castellanos-Gomez, "Photovoltaic effect in few-layer black phosphorus PN junctions defined by local electrostatic gating," *Nature Communications*, vol. 5, pp. 1–6, 2014.

[25] R. Fei and L. Yang, "Strain-engineering the anisotropic electrical conductance of few-layer black phosphorus," *Nano Letters*, vol. 14, no. 5, pp. 2884–2889, 2014.

[26] A. Avsar, I. J. Vera-Marun, J. Y. Tan, K. Watanabe, T. Taniguchi, A. H. Castro Neto, and B. OZyilmaz, "Air-stable transport in graphene-contacted, fully encapsulated ultrathin black phosphorus-based field-effect transistors," *ACS Nano*, vol. 9, no. 4, pp. 4138–4145, 2015.

[27] J. D. Wood, S. A. Wells, D. Jariwala, K.-S. Chen, E. Cho, V. K. Sangwan, X. Liu, L. J. Lauhon, T. J. Marks, and M. C. Hersam, "Effective Passivation of Exfoliated Black Phosphorus Transistors Against Ambient Degradation," *Nano letters*, vol. 14, pp. 6964–6970, 2014.

[28] A. Ayari, E. Cobas, O. Ogundadegbe, and M. S. Fuhrer, "Realization and electrical characterization of ultrathin crystals of layered transition-metal dichalcogenides," *Journal of Applied Physics*, vol. 101, no. 1, pp. 1–6, 2007.

[29] B. Radisavljevic, A. Radenovic, J. Brivio, V. Giacometti, and A. Kis, "Single-layer MoS_2 transistors." *Nature nanotechnology*, vol. 6, no. 3, pp. 147–150, 2011.

[30] H. Liu, A. T. Neal, and P. D. Ye, "Channel length scaling of MoS_2 MOSFETs," *ACS nano*, vol. 6, no. 10, pp. 8563–8569, 2012.

[31] L. Liu, Y. Lu, and J. Guo, "On monolayer MoS_2 field-effect transistors at the scaling limit," *IEEE Transactions on Electron Devices*, vol. 60, no. 12, pp. 4133–4139, 2013.

[32] S. B. Desai, S. R. Madhvapathy, A. B. Sachid, J. P. Llinas, Q. Wang, G. H. Ahn, G. Pitner, M. J. Kim, J. Bokor, C. Hu, and A. Javey, "MoS_2 transistors with 1-nanometer gate lengths," *Science*, vol. 354, no. 6308, pp. 99–102, 2016.

[33] Y. H. Lee, X. Q. Zhang, W. Zhang, M. T. Chang, C. T. Lin, K. D. Chang, Y. C. Yu, J. T. W. Wang, C. S. Chang, L. J. Li, and T. W. Lin, "Synthesis of large-area MoS_2 atomic layers with chemical vapor deposition," *Advanced Materials*, vol. 24, pp. 2320–2325, 2012.

[34] X. Duan, C. Wang, J. C. Shaw, R. Cheng, Y. Chen, H. Li, X. Wu, Y. Tang, Q. Zhang, A. Pan, J. Jiang, R. Yu, Y. Huang, and X. Duan, "Lateral epitaxial growth of two-dimensional layered semiconductor heterojunctions," *Nature Nanotechnology*, vol. 9, no. 12, pp. 1024–1030, 2014.

[35] S. M. Morrow, A. J. Bissette, and S. P. Fletcher, "Transmission of chirality through space and across length scales," *Nature Nanotechnology*, vol. 12, no. 5, pp. 410–419, 2017.

[36] Y. Ma, P. Oleynikov, and O. Terasaki, "Electron-crystallography approaches for determining the handedness of a chiral zeolite nano-crystal," *Nature Materials*, no. May, pp. 1–6, 2017.

[37] S. S. Tsirkin, I. Souza, and D. Vanderbilt, "Composite Weyl nodes stabilized by screw symmetry with and without time-reversal invariance," *Physical Review B*, vol. 96, no. 4, pp. 1–17, 2017.

[38] V. A. Shalygin, A. N. Sofronov, L. E. Vorob'ev, and I. I. Farbshtein, "Current-induced spin polarization of holes in tellurium," *Physics of the Solid State*, vol. 54, no. 12, pp. 2362–2373, 2012.

[39] V. A. Shalygin, M. D. Moldavskaya, S. N. Danilov, I. I. Farbshtein, and L. E. Golub, "Circular photon drag effect in bulk tellurium," *Physical Review B - Condensed Matter and Materials Physics*, vol. 93, no. 4, pp. 1–8, 2016.

[40] H. Peng, N. Kioussis, and G. J. Snyder, "Elemental tellurium as a chiral p-type thermoelectric material," *Physical Review B*, vol. 89, no. 19, p. 195206, 2014.

[41] K. Nakayama, M. Kuno, K. Yamauchi, S. Souma, K. Sugawara, T. Oguchi, T. Sato, and T. Takahashi, "Band splitting and Weyl nodes in trigonal tellurium studied by angle-resolved photoemission spectroscopy and density functional theory," *Physical Review B*, vol. 95, no. 12, p. 125204, 2017.

[42] M. Hirayama, R. Okugawa, S. Ishibashi, S. Murakami, and T. Miyake, "Weyl node and spin texture in trigonal tellurium and selenium," *Physical Review Letters*, vol. 114, no. 20, p. 206401, 2015.

[43] T. Furukawa, Y. Shimokawa, K. Kobayashi, and T. Itou, "Observation of current-induced bulk magnetization in elemental tellurium," *Nature Communications*, vol. 8, no. 1, pp. 1–5, 2017.

[44] Y. K. V.B. Anzin, V. Veselago, P. P.N.Press, G. Britain, I. Asymmetry, S. Of, L. Levelstellurium, S. Academy, H. P. Physics, and T. H. E. Effective, "Inversion asymmetry splitting of Landau levels in tellurium," *Solid State Communications*, vol. 8, pp. 1773–1777, 1970.

[45] N. Mounet, M. Gibertini, P. Schwaller, D. Campi, A. Merkys, A. Marrazzo, T. Sohier, I. E. Castelli, A. Cepellotti, G. Pizzi, and N. Marzari, "Two-dimensional materials from high-throughput computational exfoliation of experimentally known compounds," *Nature Nanotechnology*, vol. 13, no. March, pp. 1–7, 2018.

[46] R. W. Dutton and R. S. Muller, "Electrical properties of tellurium thin films," *Proceedings of the IEEE*, vol. 59, no. 10, pp. 1511–1517, 1971.

[47] C. J. Hawley, B. R. Beatty, G. Chen, and J. E. Spanier, "Shape-controlled vapor-transport growth of tellurium nanowires," *Crystal Growth and Design*, vol. 12, no. 6, pp. 2789–2793, 2012.

[48] Q. Wang, G. D. Li, Y. L. Liu, S. Xu, K. J. Wang, and J. S. Chen, "Fabrication and growth mechanism of selenium and tellurium nanobelts through a vacuum vapor deposition route," *Journal of Physical Chemistry C*, vol. 111, no. 35, pp. 12 926–12 932, 2007.

[49] S. Sen, U. M. Bhatta, V. Kumar, K. P. Muthe, S. Bhattacharya, S. K. Gupta, and J. V. Yakhmi, "Synthesis of tellurium nanostructures by physical vapor deposition and their growth mechanism," *Crystal Growth & Design*, vol. 8, no. 1, pp. 238–242, 2007.

[50] B. Geng, Y. Lin, X. Peng, G. Meng, and L. Zhang, "Large-scale synthesis of single-crystalline Te nanobelts by a low-temperature chemical vapour deposition route," *Nanotechnology*, vol. 14, no. 9, pp. 983–986, 2003.

[51] B. Mayers and Y. Xia, "One-dimensional nanostructures of trigonal tellurium with various morphologies can be synthesized using a solution-phase approach," *Journal of Materials Chemistry*, vol. 12, no. 6, pp. 1875–1881, 2002.

[52] H. O. Churchill, G. J. Salamo, S. Q. Yu, T. Hironaka, X. Hu, J. Stacy, and I. Shih, "Toward Single Atom Chains with Exfoliated Tellurium," *Nanoscale Research Letters*, vol. 12, pp. 1–6, 2017.

[53] Q. Wang, M. Safdar, K. Xu, M. Mirza, Z. Wang, and J. He, "Van der Waals epitaxy and photoresponse of hexagonal tellurium nanoplates on flexible mica sheets," *ACS Nano*, vol. 8, no. 7, pp. 7497–7505, 2014.

[54] X. Huang, J. Guan, Z. Lin, B. Liu, S. Xing, W. Wang, and J. Guo, "Epitaxial Growth and Band Structure of Te Film on Graphene," *Nano Letters*, vol. 17, no. 8, pp. 4619–4623, 2017.

[55] J. Chen, Y. Dai, Y. Ma, X. Dai, W. Ho, and M. Xie, "Ultrathin β-tellurium layers grown on highly oriented pyrolytic graphite by molecular-beam epitaxy," *Nanoscale*, vol. 9, no. 41, pp. 15 945–15 948, 2017.

[56] J. Qiao, Y. Pan, F. Yang, C. Wang, Y. Chai, and W. Ji, "Few-layer Tellurium: one-dimensional-like layered elementary semiconductor with striking physical properties," *Science Bulletin*, vol. 63, no. 3, pp. 159–168, 2018.

[57] Z. Zhu, X. Cai, S. Yi, J. Chen, Y. Dai, C. Niu, Z. Guo, M. Xie, F. Liu, J. H. Cho, Y. Jia, and Z. Zhang, "Multivalency-Driven Formation of Te-Based Monolayer Materials: A Combined First-Principles and Experimental study," *Physical Review Letters*, vol. 119, no. 10, pp. 1–5, 2017.

[58] L. Xian, A. P. Paz, E. Bianco, P. M. Ajayan, and A. Rubio, "Square selenene and tellurene: novel group VI elemental 2D semi-Dirac materials and topological insulators," *2D Materials*, vol. e, p. 041003, 2017.

[59] Z. Zhu, C. Cai, C. Niu, C. Wang, Q. Sun, X. Han, Z. Guo, and Y. Jia, "Tellurene-a monolayer of tellurium from first-principles prediction," *arXiv preprint arXiv:1605.03253*, pp. 1–15, 2016.

[60] J. A. Zasadzinski, R. Viswanathan, L. Madsen, J. Garnaes, and D. K. Schwartz, "Langmuir-Blodgett films," *Science*, vol. 263, no. 5154, pp. 1726–1733, 1994.

[61] M. Mo, J. Zeng, X. Liu, W. Yu, S. Zhang, and Y. Qian, "Controlled hydrothermal synthesis of thin single-crystal tellurium nanobelts and nanotubes," *Advanced Materials*, vol. 14, no. 22, pp. 1658–1662, 2002.

[62] H. S. Qian, S. H. Yu, J. Y. Gong, L. B. Luo, and L. F. Fei, "High-quality luminescent tellurium nanowires of several nanometers in diameter and high aspect ratio synthesized by a poly (vinyl pyrrolidone)- assisted hydrothermal process," *Langmuir*, vol. 22, no. 8, pp. 3830–3835, 2006.

[63] L. A. Agapito, N. Kioussis, W. A. Goddard, and N. P. Ong, "Novel family of chiral-based topological insulators: elemental tellurium under strain," *Physical Review Letters*, vol. 110, no. 17, p. 176401, 2013.

[64] A. Coker, T. Lee, and T. P. Das, "Investigation of the electronic properties of tellurium energy-band structure," *Physical Review B*, vol. 22, no. 6, pp. 2968–2975, 1980.

[65] P. Cherin and P. Unger, "Two-dimensional refinement of the crystal structure of tellurium," *Acta Crystallographia*, vol. 23, pp. 670–671, 1967.

[66] R. M. Martin, G. Lucovsky, and K. Helliwell, "Intermolecular bonding and lattice dynamics of Se and Te," *Physical Review B*, vol. 13, no. 4, pp. 1383–1395, 1976.

[67] Y. Du, G. Qiu, Y. Wang, M. Si, X. Xu, W. Wu, and P. D. Ye, "One-dimensional van der Waals material tellurium: Raman spectroscopy under strain and magneto-transport," *Nano Letters*, vol. 17, p. 39653973, 2017.

[68] A. S. Pine and G. Dresselhaus, "Raman spectra and lattice dynamics of tellurium," *Physical Review B*, vol. 4, no. 2, pp. 356–371, 1971.

[69] B. H. Torrie, "Raman spectrum of tellurium," *Solid State Communications*, vol. 8, no. 22, pp. 1899–1901, 1970.

[70] W. Richter, "Extraordinary phonon Raman scattering and resonance enhancement in tellurium," *Journal of Physics and Chemistry of Solids*, vol. 33, no. 11, pp. 2123–2128, 1972.

[71] X. Wang, A. M. Jones, K. L. Seyler, V. Tran, Y. Jia, H. Zhao, H. Wang, L. Yang, X. Xu, and F. Xia, "Highly anisotropic and robust excitons in monolayer black phosphorus," *Nature Nanotechnology*, vol. 10, no. 6, pp. 517–521, 2015.

[72] C. Lee, H. Yan, L. Brus, T. Heinz, J. Hone, and S. Ryu, "Anomalous lattice vibrations of single-and few-layer MoS_2," *ACS nano*, vol. 4, no. 5, pp. 2695–700, 2010.

[73] Y. Wang, G. Qiu, R. Wang, S. Huang, Q. Wang, Y. Liu, Y. Du, W. A. Goddard, M. J. Kim, X. Xu, P. D. Ye, and W. Wu, "Field-effect transistors made from solution-grown two-dimensional tellurene," *Nature Electronics*, vol. 1, no. 4, pp. 228–236, 2018.

[74] L. Rothkirch, R. Link, W. Sauer, and F. Manglus, "Anisotropy of the Electric Conductivity of Tellurium Single Crystals," *physica status solidi (b)*, vol. 31, no. 1, pp. 147–155, 1969.

[75] Y. Liu, J. Guo, E. Zhu, L. Liao, S.-J. Lee, M. Ding, I. Shakir, V. Gambin, Y. Huang, and X. Duan, "Approaching the SchottkyMott limit in van der Waals metalsemiconductor junctions," *Nature*, vol. 557, no. 7707, pp. 696–700, 2018.

[76] C. D. English, K. K. H. Smithe, R. L. Xu, and E. Pop, "Approaching ballistic transport in monolayer MoS_2 transistors with self-aligned 10 nm top gates," *Technical Digest - International Electron Devices Meeting, IEDM*, pp. 5.6.1–5.6.4, 2017.

[77] J. J. Gu, H. Wu, Y. Liu, A. T. Neal, R. G. Gordon, and P. D. Ye, "Size-dependent-transport study of $In_0.53Ga_0.47As$ gate-all-around nanowire MOSFETs: Impact of quantum confinement and volume inversion," *IEEE Electron Device Letters*, vol. 33, no. 7, pp. 967–969, 2012.

[78] L. Yang, K. Majumdar, H. Liu, Y. Du, H. Wu, M. Hatzistergos, P. Y. Hung, R. Tieckelmann, W. Tsai, C. Hobbs, and P. D. Ye, "Chloride molecular doping technique on 2D materials: WS_2 and MoS_2," *Nano Letters*, vol. 14, no. 11, pp. 6275–6280, 2014.

[79] Y. Du, L. Yang, H. Zhou, and P. D. Ye, "Performance enhancement of black phosphorus field-effect transistors by chemical doping," *IEEE Electron Device Letters*, vol. 37, no. 4, pp. 429–432, 2016.

[80] A. Prakash, Y. Cai, G. Zhang, Y. W. Zhang, and K. W. Ang, "Black Phosphorus N-Type Field-Effect Transistor with Ultrahigh Electron Mobility via Aluminum Adatoms Doping," *Small*, vol. 13, no. 5, pp. 1–7, 2017.

[81] D. A. Wright, "Thermoelectric Properties of Bismuth Telluride and its Alloys," pp. 834–834, 1958.

[82] D. A. Polvani, J. F. Meng, N. V. Chandra Shekar, J. Sharp, and J. V. Badding, "Large Improvement in Thermoelectric Properties in Pressure-Tuned p-Type $Sb_1.5Bi_0.5Te_3$," *Chemistry of Materials*, vol. 13, no. 6, pp. 2068–2071, 2001.

[83] R. Venkatasubramanian, E. Siivola, T. Colpitts, and B. O'Quinn, "Thin-film thermoelectric devices with high room-temperature figures of merit." *Nature*, vol. 413, no. 6856, pp. 597–602, 2001.

[84] M. S. Dresselhaus, G. Chen, M. Y. Tang, R. Yang, H. Lee, D. Wang, Z. Ren, J. P. Fleurial, and P. Gogna, "New directions for low-dimensional thermoelectric materials," *Advanced Materials*, vol. 19, no. 8, pp. 1043–1053, 2007.

[85] Y. Pei, X. Shi, A. Lalonde, H. Wang, L. Chen, and G. J. Snyder, "Convergence of electronic bands for high performance bulk thermoelectrics," *Nature*, vol. 473, no. 7345, pp. 66–69, 2011.

[86] S. Lin, W. Li, Z. Chen, J. Shen, B. Ge, and Y. Pei, "Tellurium as a high-performance elemental thermoelectric." *Nature communications*, vol. 7, p. 10287, 2016.

[87] G. Qiu, Y. Wang, Y. Nie, Y. Zheng, K. Cho, W. Wu, and P. D. Ye, "Quantum transport and band structure evolution under high magnetic field in few-layer tellurene," *Nano Letters*, vol. 18, no. 9, pp. 5760–5767, 2018.

[88] P. Gehring, A. Harzheim, J. Spiece, Y. Sheng, G. Rogers, C. Evangeli, A. Mishra, B. J. Robinson, K. Porfyrakis, J. H. Warner, O. V. Kolosov, G. A. D. Briggs, and J. A. Mol, "Field-effect control of Graphene-Fullerene thermoelectric nanodevices," *Nano Letters*, p. acs.nanolett.7b03736, 2017.

[89] M. Kayyalha, J. Maassen, M. Lundstrom, L. Shi, and Y. P. Chen, "Gate-tunable and thickness-dependent electronic and thermoelectric transport in few-layer MoS_2," *Journal of Applied Physics*, vol. 120, no. 13, 2016.

[90] M.-J. Lee, J.-H. Ahn, J. H. Sung, H. Heo, S. G. Jeon, W. Lee, J. Y. Song, K.-H. Hong, B. Choi, S.-H. Lee, and M.-H. Jo, "Thermoelectric materials by using two-dimensional materials with negative correlation between electrical and thermal conductivity," *Nature Communications*, vol. 7, no. May, p. 12011, 2016.

[91] K. V. Klitzing, G. Dorda, and M. Pepper, "New method for high-accuracy determination of the fine-structure constant based on quantized Hall resistance," *Physical Review Letters*, vol. 45, no. 6, pp. 494–497, 1980.

[92] D. C. Tsui and A. C. Gossard, "Resistance standard using quantization of the Hall resistance of GaAs-AlxGa1-xAs heterostructures," *Applied Physics Letters*, vol. 38, no. 7, pp. 550–552, 1981.

[93] V. P. Gusynin and S. G. Sharapov, "Unconventional integer quantum Hall effect in graphene," *Physical Review Letters*, vol. 95, no. 14, p. 146801, 2005.

[94] D. A. Bandurin, A. V. Tyurnina, G. L. Yu, A. Mishchenko, V. Zólyomi, S. V. Morozov, R. K. Kumar, R. V. Gorbachev, Z. R. Kudrynskyi, S. Pezzini, Z. D. Kovalyuk, U. Zeitler, K. S. Novoselov, A. Patanè, L. Eaves, I. V. Grigorieva, V. I. Fal'Ko, A. K. Geim, and Y. Cao, "High electron mobility, quantum Hall effect and anomalous optical response in atomically thin InSe," *Nature Nanotechnology*, vol. 12, no. 3, pp. 223–227, 2017.

[95] L. Li, F. Yang, G. J. Ye, Z. Zhang, Z. Zhu, W. Lou, X. Zhou, L. Li, K. Watanabe, T. Taniguchi, K. Chang, Y. Wang, X. H. Chen, and Y. Zhang, "Quantum Hall effect in black phosphorus two-dimensional electron system," *Nature Nanotechnology*, vol. 11, no. 7, pp. 593–597, 2016.

[96] J. Yang, S. Tran, J. Wu, S. Che, P. Stepanov, T. Taniguchi, K. Watanabe, H. Baek, D. Smirnov, R. Chen, and C. N. Lau, "Integer and fractional quantum Hall effect in ultra-high quality few-layer black phosphorus transistors," *Nano Letters*, vol. 18, no. 1, pp. 229–234, 2018.

[97] X. Chen, Y. Wu, Z. Wu, Y. Han, S. Xu, L. Wang, W. Ye, T. Han, Y. He, Y. Cai, and N. Wang, "High-quality sandwiched black phosphorus heterostructure and its quantum oscillations," *Nature Communications*, vol. 6, p. 7315, 2015.

[98] B. Fallahazad, H. C. Movva, K. Kim, S. Larentis, T. Taniguchi, K. Watanabe, S. K. Banerjee, and E. Tutuc, "Shubnikov-de Haas oscillations of high-mobility holes in monolayer and bilayer WSe$_2$: Landau level degeneracy, effective mass, and negative compressibility," *Physical Review Letters*, vol. 116, no. 8, pp. 1–5, 2016.

[99] H. C. Movva, B. Fallahazad, K. Kim, S. Larentis, T. Taniguchi, K. Watanabe, S. K. Banerjee, and E. Tutuc, "Density-dependent quantum Hall states and Zeeman splitting in monolayer and bilayer WSe$_2$," *Physical Review Letters*, vol. 118, no. 24, p. 247701, 2017.

[100] X. Cui, E. M. Shih, L. A. Jauregui, S. H. Chae, Y. D. Kim, B. Li, D. Seo, K. Pistunova, J. Yin, J. H. Park, H. J. Choi, Y. H. Lee, K. Watanabe, T. Taniguchi, P. Kim, C. R. Dean, and J. C. Hone, "Low temperature Ohmic Contact to Monolayer MoS$_2$ by van der Waals Bonded Co/h-BN Electrodes," *Nano Letters*, vol. 17, no. 8, pp. 4781–4786, 2017.

[101] Z. Wu, S. Xu, H. Lu, A. Khamoshi, G. B. Liu, T. Han, Y. Wu, J. Lin, G. Long, Y. He, Y. Cai, Y. Yao, F. Zhang, and N. Wang, "Even-odd layer-dependent magnetotransport of high-mobility Q-valley electrons in transition metal disulfides," *Nature Communications*, vol. 7, pp. 1–8, 2016.

[102] X. Cui, G.-H. Lee, Y. D. Kim, G. Arefe, P. Y. Huang, C.-H. Lee, D. a. Chenet, X. Zhang, L. Wang, F. Ye, F. Pizzocchero, B. S. Jessen, K. Watanabe, T. Taniguchi, D. a. Muller, T. Low, P. Kim, and J. Hone, "Multi-terminal transport measurements of MoS$_2$ using a van der Waals heterostructure device platform," *Nature Nanotechnology*, vol. 10, no. 6, pp. 534–540, 2015.

[103] W. Yu, Y. Jiang, J. Yang, Z. L. Dun, H. D. Zhou, Z. Jiang, P. Lu, and W. Pan, "Quantum oscillations at integer and fractional Landau level indices in single-crystalline $ZrTe_5$," *Scientific Reports*, vol. 6, p. 35357, 2016.

[104] J. Wu, H. Yuan, M. Meng, C. Chen, Y. Sun, Z. Chen, W. Dang, C. Tan, Y. Liu, J. Yin, Y. Zhou, S. Huang, H. Q. Xu, Y. Cui, H. Y. Hwang, Z. Liu, Y. Chen, B. Yan, and H. Peng, "High electron mobility and quantum oscillations in non-encapsulated ultrathin semiconducting Bi_2O_2Se," *Nature Nanotechnology*, vol. 12, no. 6, pp. 530–534, 2017.

[105] K. von Klitzing and G.Landwehr, "Surface quantum States in tellurium," *Solid State Communications*, vol. 9, pp. 2201–2205, 1971.

[106] R. Silbermann and G. Landwehr, "Surface quantum oscillations in accumulation and inversion layers on tellurium," *Solid State Communications*, vol. 16, pp. 6–9, 1975.

[107] K. von Klitzing, "Magnetophonon Oscillatinos in Tellurium under Hot Carrier Conditions," *Solid State Communications*, vol. 15, pp. 1721–1725, 1974.

[108] A. S. Epstein, H. Fritzsche, and K. Lark-Horovitz, "Electrical properties of tellurium at the melting point and in the liquid state," *Physical Review*, vol. 107, no. 2, pp. 412–419, 1957.

[109] S. Hikami, A. I. Larkin, and Y. Nagaoka, "Spin-Orbit Interaction and Magnetoresistance in the Two Dimensional Random System," *Progress of Theoretical Physics*, vol. 63, no. 2, pp. 707–710, 1980.

[110] P. A. Lee, A. D. Stone, and H. Fukuyama, "Universal conductance fluctuations in metals: Effects of finite temperature, interactions, and magnetic field," *Physical Review B*, vol. 35, no. 3, pp. 1039–1070, 1987.

[111] P.-Y. Yang, L. Y. Wang, Y.-W. Hsu, and J.-J. Lin, "Universal conductance fluctuations in indium tin oxide nanowires," *Physical Review B*, vol. 085423, pp. 30–32, 2012.

[112] D. Liang, M. R. Sakr, and X. P. Gao, "One-dimensional weak localization of electrons in a single InAs nanowire," *Nano Letters*, vol. 9, no. 4, pp. 1709–1712, 2009.

[113] X. Ren, Y. Wang, Z. Xie, F. Xue, C. Leighton, and C. D. Frisbie, "Gate-tuned insulator-metal transition in electrolyte-gated transistors based on tellurene," *Nano Letters*, vol. 19, pp. 4738–4744, 2019.

[114] G. Qiu, M. Si, Y. Wang, X. Lyu, W. Wu, and P. D. Ye, "High-Performance Few-Layer Tellurium CMOS Devices Enabled by Atomic Layer Deposited Dielectric Doping Technique," *2018 76th Device Research Conference (DRC)*, vol. 06202, no. 2017, pp. 1–2, 2018.

[115] S. Berweger, G. Qiu, Y. Wang, B. Pollard, K. L. Genter, R. Tyrrell-Ead, T. M. Wallis, W. Wu, P. D. Ye, and P. Kabos, "Imaging carrier inhomogeneities in ambipolar tellurene field effect transistors," *Nano Letters*, vol. 19, pp. 1289–1294, 2019.

[116] C. H. Wang, J. A. C. Incorvia, C. J. McClellan, A. C. Yu, M. J. Mleczko, E. Pop, and H. S. Wong, "Unipolar n-type black phosphorus transistors with low work function contacts," *Nano Letters*, vol. 18, no. 5, pp. 2822–2827, 2018.

[117] B. E. Coss, W. Y. Loh, R. M. Wallace, J. Kim, P. Majhi, and R. Jammy, "Near band edge Schottky barrier height modulation using high-κ dielectric dipole tuning mechanism," *Applied Physics Letters*, vol. 95, no. 22, p. 222105, 2009.

[118] Y. W. Suen, J. Jo, M. B. Santos, L. W. Engel, S. W. Hwang, and M. Shayegan, "Missing integral quantum Hall effect in a wide single quantum well," *Physical Review B*, vol. 44, no. 11, pp. 5947–5950, 1991.

[119] Y. W. Suen, M. B. Santos, and M. Shayegan, "Correlated states of an electron system in a wide quantum well," *Physical Review Letters*, vol. 69, no. 11, pp. 1664–1668, 1992.

[120] T. S. Lay, Y. W. Suen, H. C. Manoharan, X. Ying, M. B. Santos, and M. Shayegan, "Anomalous temperature dependence of the correlated ν=1 quantum Hall effect in bilayer electron systems," *Physical Review B*, vol. 50, no. 23, p. 17725, 1994.

[121] Y. W. Suen, L. W. Engel, M. B. Santos, M. Shayegan, and D. C. Tsui, "Observation of ν=1/2 fractional quantum Hall state in a double-layer electron system," *Physical Review Letters*, vol. 68, no. 9, pp. 1379–1382, 1992.

[122] K. Nomura and A. H. MacDonald, "Quantum hall ferromagnetism in graphene," *Physical Review Letters*, vol. 96, no. 25, p. 256602, 2006.

[123] S. Tran, J. Yang, N. Gillgren, T. Espiritu, Y. Shi, K. Watanabe, T. Taniguchi, S. Moon, H. Baek, D. Smirnov, M. Bockrath, R. Chen, and C. N. Lau, "Surface Transport and Quantum Hall Effect in Ambipolar Black Phosphorus Double Quantum Wells," *Science Advances*, vol. 3, no. 6, p. e1603179, 2017.

[124] K. Takashina, A. Fujiwara, S. Horiguchi, Y. Takahashi, and Y. Hirayama, "Valley splitting control in $SiO_2/Si/SiO_2$ quantum wells in the quantum Hall regime," *Physical Review B - Condensed Matter and Materials Physics*, vol. 69, no. 16, p. 161304, 2004.

[125] A. F. Young, C. R. Dean, L. Wang, H. Ren, P. Cadden-Zimansky, K. Watanabe, T. Taniguchi, J. Hone, K. L. Shepard, and P. Kim, "Spin and valley quantum Hall ferromagnetism in graphene," *Nature Physics*, vol. 8, no. 7, pp. 550–556, 2012.

[126] Y. Zhang, Z. Jiang, J. P. Small, M. S. Purewal, Y. W. Tan, M. Fazlollahi, J. D. Chudow, J. A. Jaszczak, H. L. Stormer, and P. Kim, "Landau-level splitting in graphene in high magnetic fields," *Physical Review Letters*, vol. 96, no. 13, p. 136806, 2006.

[127] S. Xu, J. Shen, G. Long, Z. Wu, Z. Q. Bao, C. C. Liu, X. Xiao, T. Han, J. Lin, Y. Wu, H. Lu, J. Hou, L. An, Y. Wang, Y. Cai, K. M. Ho, Y. He, R. Lortz, F. Zhang, and N. Wang, "Odd-Integer quantum Hall states and giant spin susceptibility in p -type few-layer WSe_2," *Physical Review Letters*, vol. 118, no. 6, p. 067702, 2017.

[128] N. Zhang, G. Zhao, L. Li, P. Wang, L. Xie, H. Li, Z. Lin, J. He, Z. Sun, Z. Wang, Z. Zhang, and C. Zeng, "Evidence for Weyl fermions in the elemental semiconductor tellurium," *arXiv preprint arXiv:1906.06071*, 2019.

[129] C. ahin, J. Rou, J. Ma, and D. A. Pesin, "Pancharatnam-Berry phase and kinetic magnetoelectric effect in trigonal tellurium," *PHYSICAL REVIEW B*, vol. 97, p. 205206, 2018.

[130] F. Fei, X. Bo, R. Wang, B. Wu, J. Jiang, D. Fu, M. Gao, H. Zheng, Y. Chen, X. Wang, H. Bu, F. Song, X. Wan, B. Wang, and G. Wang, "Nontrivial Berry phase and type-II Dirac transport in the layered material $PdTe_2$," *Physical Review B*, vol. 96, no. 4, p. 041201, 2017.

[131] J. Hu, J. Y. Liu, D. Graf, S. M. Radmanesh, D. J. Adams, A. Chuang, Y. Wang, I. Chiorescu, J. Wei, L. Spinu, and Z. Q. Mao, "π Berry phase and Zeeman splitting of Weyl semimetal TaP," *Scientific Reports*, vol. 6, no. November 2015, p. 18674, 2016.

[132] Y. Zhao, H. Liu, C. Zhang, H. Wang, J. Wang, Z. Lin, Y. Xing, H. Lu, J. Liu, Y. Wang, S. M. Brombosz, Z. Xiao, S. Jia, X. C. Xie, and J. Wang, "Anisotropic Fermi surface and quantum limit transport in high mobility three-dimensional Dirac semimetal Cd_3As_2," *Physical Review X*, vol. 5, no. 3, p. 031037, 2015.

[133] H. Shinno, R. Yoshizaki, S. Tanaka, T. Doi, and H. Kamimura, "Conduction Band Structure of Tellurium," *Journal of the Physical Society of Japan*, vol. 35, no. 2, pp. 525–533, 1973.

[134] Y. Liu, W. Wu, and W. A. Goddard, "Tellurium: fast electrical and atomic transport along the weak interaction direction," *Journal of the American Chemical Society*, vol. 140, no. 2, pp. 550–553, 2018.

VITA

Gang Qiu was born in Ningbo, China in Nov. 1991. He received his Bachelor of Science degree in Microelectronics from the School of Electrical Engineering and Computer Sciences at Peking University in 2014 with Li Yanghong Scholarship. His undergraduate research focused on resistive random access memory (RRAM) devices retention failure measurement and modelling under the supervision of Prof. Jinfeng Kang. In Aug. 2014, he joined Purdue University as a Ph.D. student and worked with Prof. Peide D. Ye in school of Electrical and Computer Engineering. He is a recipient of Birck Williams Scholarship (2014-2016) and Bilsland Dissertation Fellowship (2019-2020).

His research covers a variety of topics on 2D material systems (black phosphorus, $ZrTe_5$, and tellurene) from material synthesis and characterization, novel device fabrication and measurement, to low-temperature magneto-transport. His recent research interest focuses on electronic device applications and quantum Hall behavior on novel 2D material tellurene films.

PUBLICATIONS

Journals

(† Equal contributions)

[1] Qiu, G; Niu, C.; Wang, Y.; Si, M.; Zhang, Z.; Wu, W.; Ye, P. D. Quantum Hall Effect of Massive Weyl Fermions in n-Type Tellurene Films. *(Under review) arXiv Preprint arXiv1908.11495,* **2019**.

[2] Qiu, G; Huang, S.; Segovia, M.; Venuthurumilli, P. K.; Wang, Y.; Wu, W.; Xu, X.; Ye, P. D. Thermoelectric Performance of 2D Tellurium with Accumulation Contacts. *Nano Lett.* **2019**, 19 (3), 1955-1962.

[3] Qiu, G; Wang, Y.; Nie, Y.; Zheng, Y.; Cho, K.; Wu, W.; Ye, P. D. Quantum Transport and Band Structure Evolution under High Magnetic Field in Few-Layer Tellurene. *Nano Lett.* **2018**, 18 (9), 5760-5767.

[4] Qiu, G; Nian, Q.; Motlag, M.; Jin, S.; Deng, B.; Deng, Y.; Charnas, A. R.; Ye, P. D.; Cheng, G. J. Ultrafast Laser-Shock-Induced Confined Metaphase Transformation for Direct Writing of Black Phosphorus Thin Films. *Adv. Mater.* **2018**, 30 (10), 1-8.

[5] Qiu, G; Du, Y.; Charnas, A.; Zhou, H.; Jin, S.; Luo, Z.; Zemlyanov, D. Y.; Xu, X.; Cheng, G. J.; Ye, P. D. Observation of Optical and Electrical In-Plane Anisotropy in High-Mobility Few-Layer ZrTe$_5$. *Nano Lett.* **2016**, 16 (12), 7364-7369.

[6] Wang, Y.†; Qiu, G†; Wang, R.; Huang, S.; Wang, Q.; Liu, Y.; Du, Y.; Goddard, W. A.; Kim, M. J.; Xu, X.; et al. Field-Effect Transistors Made from Solution-Grown Two-Dimensional Tellurene. *Nat. Electron.* **2018**, 1 (4), 228-236.

[7] Qin, J.†; Qiu, G†; Jian, J.; Zhou, H.; Yang, L.; Charnas, A.; Zemlyanov, D. Y.; Xu, C.-Y.; Xu, X.; Wu, W. Controlled Growth of a Large-Size 2D Selenium Nanosheet and Its Electronic and Optoelectronic Applications. *ACS Nano* **2017**, 11 (10), 10222-10229.

[8] Qin, J.†; Qiu, G†; He, W.; Jian, J.; Si, M.; Duan, Y.; Charnas, A.; Zemlyanov, D. Y.; Wang, H.; Shao, W. Epitaxial Growth of 1D Atomic Chain Based Se Nanoplates on Monolayer ReS$_2$ for HighPerformance Photodetectors. *Adv. Funct. Mater.* **2018**, 28 (48), 1806254.

[9] Niu, C.; Qiu, G; Wang, Y.; Zhang, Z.; Si, M.; Wu, W.; Ye, P. D. Gate-Tunable Strong Spin-Orbit Interaction in Two-Dimensional Tellurium Probed by Weak-Antilocalization. *(Under review) arXiv Preprint arXiv1909.06659,* **2019**.

[10] Qin, J.; Yan, H.; Qiu, G; Si, M.; Miao, P.; Duan, Y.; Shao, W.; Zhen, L.; Xu, C.; Peide, D. Y. Hybrid Dual-Channel Phototransistor Based on 1D t-Se and 2D ReS$_2$ Mixed-Dimensional Heterostructures. *Nano Res.* **2019**, 12 (3), 669-674.

[11] Wang, Y.; Ferreira, R. de S. B.; Wang, R.; Qiu, G; Li, G.; Qin, Y.; Peide, D. Y.; Sabbaghi, A.; Wu, W. Data-Driven and Probabilistic Learning of the Process-Structure-Property Relationship in Solution-Grown Tellurene for Optimized Nanomanufacturing of High-Performance Nanoelectronics. *Nano Energy* **2019**, 57, 480-491.

[12] Berweger, S.; Qiu, G; Wang, Y.; Pollard, B.; Genter, K. L.; Tyrrell-Ead, R.; Wallis, T. M.; Wu, W.; Ye, P. D.; Kabos, P. Imaging Carrier Inhomogeneities in Ambipolar Tellurene Field Effect Transistors. Nano Lett. **2019**, 19, 1289-1294.

[13] Wu, W.; Qiu, G; Wang, Y.; Wang, R.; Ye, P. Tellurene: Its Physical Properties, Scalable Nanomanufacturing, and Device Applications. *Chem. Soc. Rev.* **2018**, 47 (19), 7203-7212.

[14] Si, M.; Gao, S.; Qiu, G.; Qin, J.; Duan, Y.; Jian, J.; Wang, H.; Wu, W.; Ye, P. D. A Ferroelectric Semiconductor Field-Effect Transistor. *(under revision) arXiv Preprint arXiv1812.02933* **2018**.

[15] Si, M.; Liao, P.-Y.; Qiu, G; Duan, Y.; Ye, P. D. Ferroelectric Field-Effect Transistors Based on MoS$_2$ and CuInP$_2$S$_6$ Two-Dimensional van Der Waals Heterostructure. *ACS Nano* **2018**, 12 (7), 6700-6705.

[16] Yang, L.; Charnas, A.; Qiu, G; Lin, Y.-M.; Lu, C.-C.; Tsai, W.; Paduano, Q.; Snure, M.; Ye, P. D. How Important Is the MetalSemiconductor Contact for Schottky Barrier Transistors: A Case Study on Few-Layer Black Phosphorus? *ACS Omega* **2017**, 2 (8), 4173-4179.

[17] Min, M.; Saenz, G. A.; Qiu, G; Charnas, A.; Ye, P.; Kaul, A. B. Chemical Exfoliation of Black Phosphorus for Nanoelectronics Applications. *MRS Adv.* **2017**, 2 (60), 3697-3702.

[18] Du, Y.; Qiu, G; Wang, Y.; Si, M.; Xu, X.; Wu, W.; Ye, P. D. One-Dimensional van Der Waals Material Tellurium: Raman Spectroscopy under Strain and Magneto-Transport. *Nano Lett.* **2017**, 17, 3965-3973.

[19] Si, M.; Su, C.-J.; Jiang, C.; Conrad, N. J.; Zhou, H.; Maize, K. D.; Qiu, G; Wu, C.-T.; Shakouri, A.; Alam, M. A.; et al. Steep-Slope Hysteresis-Free Negative Capacitance MoS$_2$ Transistors. *Nat. Nanotechnol.* **2017**.

[20] Zhou, H.; Maize, K.; Qiu, G; Shakouri, A.; Ye, P. D. β-Ga$_2$O$_3$ on Insulator Field-Effect Transistors with Drain Currents Exceeding 1.5 A/mm and Their Self-Heating Effect. *Appl. Phys. Lett.* **2017**, 111 (9), 92102.

[21] Zhou, H.; Alghmadi, S.; Si, M.; Qiu, G; Peide, D. Y. Al$_2$O$_3$/β-Ga$_2$O$_3$ (-201) Interface Improvement Through Piranha Pretreatment and Postdeposition Annealing. *IEEE Electron Device Lett.* **2018**, 37 (11), 1411-1414.

[22] Zhou, H.; Si, M.; Alghamdi, S.; Qiu, G; Yang, L.; Peide, D. Y. High-Performance Depletion/Enhancement-Mode $-\beta$-Ga_2O_3 on Insulator (GOOI) Field-Effect Transistors With Record Drain Currents of 600/450 mA/mm. *IEEE Electron Device Lett.* **2018**, 38 (1), 103-106.

Conferences

[1] Qiu, G.; Wang, Y.; Wu, W.; Peide, D. Y. High-Performance 2D Tellurium Transistors Towards CMOS Logic Applications. In Meeting Abstracts; *The 236th Electrochemical Conference*, **2019**; p 869.

[2] Qiu, G.; Wang, Y.; Wu, W.; Ye, P. P. High-Efficiency Thermoelectric 2D Tellurium Devices with Accumulation-Type Metal-to-Semiconductor Contacts. In *APS March Meeting*; **2019**.

[3] Liao, P.-Y.; Si, M.; Qiu, G.; Peide, D. Y. 2D Ferroelectric $CuInP_2S_6$: Synthesis, ReRAM, and FeRAM. In *2018 76th Device Research Conference (DRC)*; IEEE, **2018**.

[4] Qiu, G.; Si, M.; Wang, Y.; Lyu, X.; Wu, W.; Peide, D. Y. High-Performance Few-Layer Tellurium CMOS Devices Enabled by Atomic Layer Deposited Dielectric Doping Technique. In *2018 76th Device Research Conference (DRC)*; IEEE, **2018**.

[5] Qiu, G.; Wang, Y.; Wu, W.; Ye, P. P. Magneto-Transport in One-Dimensional van Der Waals Chiral Material Tellurium. In *APS March Meeting*; **2018**.

[6] Qiu, G.; Wang, Y.; Du, Y.; Yang, L.; Wu, W.; Ye, P. Demonstration of High-Performance Transistors with Narrow Bandgap High-Mobility Ultrathin 2D Films. In *APS March Meeting*; **2017**.

[7] Qiu, G.; Nian, Q.; Deng, Y.; Deng, B.; Jin, S.; Charnas, A.; Cheng, G.; Ye, P. Synthesis of Black Phosphorus Films and Particles by Ultra-Fast Laser Ablation. In *APS March Meeting*; **2016**.

[8] Berweger, S.; Qiu, G.; Wang, Y.; Pollard, B.; Genter, K.; Tyrrell-Ead, R.; Wallis, T.; Wu, W.; Ye, P. P.; Kabos, P. Studying Ambipolar Tellurene Field Effect Transistors Using Microwave Near-Field Microscopy. In *APS March Meeting*; **2019**.

[9] Niu, C.; Qiu, G.; Wang, Y.; Wu, W.; Ye, P. P. Quantum Transport in n-Doped 2D Tellurene. In *APS March Meeting*; **2019**.

[10] Jnawali, G.; Linser, S.; Pournia, S.; Abbasian Shojaei, I.; Jackson, H.; Smith, L.; Wang, R.; Qiu, G.; Wu, W.; Ye, P. P. Revealing Optical Transitions and Carrier Dynamics within the Bulk Band Structure of Chiral Tellurium Nanosheets. In *APS March Meeting*; **2019**.

[11] Charnas, A.; Qiu, G.; Si, M.; Wang, Y.; Wu, W.; Ye, P. P. Record-High Drain Current in p-Type 2D Transistors with High-k Dielectric and Accumulation-Type Contacts. In *APS March Meeting*; **2018**.

[12] Liao, P.-Y.; Si, M.; Qiu, G.; Ye, P. P. Room-Temperature Ferroelectricity in Two-Dimensional Material $CuInP_2S_6$: Synthesis and Devices. In *APS March Meeting*; **2018**.

[13] Wang, Y.; Qiu, G.; Ye, P.; Wu, W. Solution Manufacturing of 2D Piezoelectric Semiconductors for Smart Wearable Devices. In *APS March Meeting*; **2017**.

[14] Du, Y.; Qiu, G.; Wang, Y.; Wu, W.; Ye, P.; Collaboration, I. E.; Collaboration, C. E. Magneto-Transport and Strain Experiments in Anisotropic High Mobility van Der Waals Semiconductor. In *APS March Meeting*; **2017**.

[15] Charnas, A.; Qiu, G.; Deng, Y.; Wang, Y.; Du, Y.; Yang, L.; Wu, W.; Ye, P. Photo-Detection on Narrow-Bandgap High-Mobility 2D Semiconductors. In *APS March Meeting*; **2017**.

[16] Yang, L. M.; Qiu, G.; Si, M. W.; Charnas, A. R.; Milligan, C. A.; Zemlyanov, D. Y.; Zhou, H.; Du, Y. C.; Lin, Y. M.; Tsai, W. Few-Layer Black Phosporous PMOSFETs with BN/Al_2O_3 Bilayer Gate Dielectric: Achieving $_On$= 850A/m, g_m= 340μS/mm, and R$_c$= 0.58 k$\Omega \cdot \mu$m. *In 2016 IEEE International Electron Devices Meeting (IEDM); IEEE*, **2018**; p 5.